Search for the rare decay $K^+ \to \pi^+ \nu\overline{\nu}$ with $p_{\pi^+} < 199 MeV/c$

A Dissertation, Presented

by

Ilektra-Athanasia Christidi

to

The Graduate School

in Partial Fulfillment of the

Requirements

for the Degree of

Doctor of Philosophy

in

Physics

Stony Brook University

December 2006

Stony Brook University

The Graduate School

Ilektra-Athanasia Christidi

We, the dissertation committee for the above candidate for the Doctor of Philosophy degree, hereby recommend acceptance of this dissertation.

Michael D. Marx
Professor, Department of Physics, Stony Brook University
Dissertation Director

Robert Shrock
Professor, Department of Physics, Stony Brook University
Chairman of Dissertation

Axel Drees
Professor, Department of Physics, Stony Brook University

David E. Jaffe
Electronic Detector Group, Physics Department, Brookhaven National Laboratory
Outside Member

This dissertation is accepted by the Graduate School.

Dean of the Graduate School

Abstract of the Dissertation

Search for the rare decay $K^+ \rightarrow \pi^+ \nu\overline{\nu}$ with $p_{\pi^+} < 199 MeV/c$

by

Ilektra-Athanasia Christidi

Doctor of Philosophy

in

Physics

Stony Brook University

2006

The rare Kaon decay $K^+ \rightarrow \pi^+ \nu\overline{\nu}$ is a valuable probe for the flavor structure of the Standard Model (SM) and for new physics. In the SM, its Branching Ratio is of the order of 10^{-10} and depends on the magnitude of the V_{td} element of the CKM matrix, which defines the mixing between the top and down quark and includes the imaginary phase of the matrix. This phase is the only source of CP violation in the SM. This rare decay is being searched for by the experiment E949 at BNL's Alternating Gradient Synchrotron in two kinematic regions, "PNN1" with $211 MeV/c < p_{\pi^+} < 229 MeV/c$

and "PNN2" with $p_{\pi^+} < 199 MeV/c$. This thesis describes the analysis of the PNN2 region. A "blind analysis" approach is taken, in which the expected backgrounds are determined a priori and selection criteria ("cuts") to suppress them are developed based on 1/3 of the data, uniformly selected throughout the total sample. During this process, potential signal events (any events in the multidimensional signal region defined by these cuts) are masked out. Then the expected background in the signal region is measured with data, using the final version of the cuts in a bifurcated analysis, and verified by examining the number of events close to (but still outside of) the signal region. For some background processes that are difficult to distinguish in real data, Monte Carlo simulation is used. Finally the acceptance loss of the offline cuts and the online trigger is measured using special background samples of data and signal simulation, and the single event sensitivity is calculated.

Contents

List of Figures

Acknowledgements

I want to acknowledge moral support from Donald Duck and the Cookie Monster I also want to thank god that is finally over.

Chapter 1

Introduction

“42”

Chapter 2

Theory

2.1 Introduction

The Standard Model (SM) of particle physics has accounted for almost all particles and their interactions that have been observed. Matter is built of 3 generations of leptons and their respective neutrinos, and 3 generations of quarks. The interactions between them are explained by two gauge theories: Quantum Chromodynamics (QCD), with 8 gauge bosons called gluons, which accounts for the strong interaction between quarks, and the Glashow-Weinberg-Salam (GWS) theory, which accounts for the electromagnetic (carried by the photon between electrically charged leptons and quarks) and the weak interactions (which are carried by the $W^{\pm}$ and Z^{o} bosons and affect all particles) and their unification. In the context of the SM, the masses of all particles, except for the photon and gluon which are massless, arise from spontaneous symmetry breaking that occurs due to the existence of a scalar particle called the Higgs boson.

It has been evident from as early as 1956 that the weak interaction differs from the other ones in the non-preservation of parity P, as it is a vector-axial $(V-A)$ interaction. However, the combined charge conjugation - parity (CP) symmetry was thought to be conserved until the astonishing result of the BNL E-0181 experiment in 1964 [1], that discovered direct CP violation in the neutral Kaon system. Since then, an elegant explanation has been incorporated in the SM, where CP violation arises naturally from the existence of 3 families of quarks that "mix" with each other through the weak interactions: the Kobayashi-Maskawa (KM) theory [2] introduces a 3×3 unitary matrix for this mixing, called the Cabibbo-Kobayashi-Maskawa (CKM) matrix. Particle flavors are still conserved in the strong and electromagnetic interactions.

As $K^+ \to \pi^+\nu\overline{\nu}$ is a Flavor Changing Neutral Current (FCNC) weak process, the flavor structure of the SM and its predictions for the Branching Ratio BR of this decay will be presented in this chapter. The particular aspects and parameters of the SM that can be measured with this decay will be pinpointed and the potential physics beyond the SM that could be accessed will be reviewed.

2.2 CP violation in the Standard Model

There are charged and neutral current processes in the weak interaction, mediated by the W^+ or W^- and the Z^o bosons respectively. In the charged-current processes, one quark can transform into another quark of the same family with a different electric charge/flavor (e.g., $u \to d$), and one lepton can transform into the respective neutrino (e.g., $e^- \to \nu_e$) and vice versa. However, as the fact that heavier quarks decay into lighter ones shows, the charged-current weak interaction can even transform quarks to different family ones (e.g., $c \to d$), with the strength of the mixing depending on the parameters of the CKM matrix V:

$$\begin{pmatrix} d' \\ s' \\ b' \end{pmatrix} = V \begin{pmatrix} d \\ s \\ b \end{pmatrix} = \begin{pmatrix} V_{ud} & V_{us} & V_{ub} \\ V_{cd} & V_{cs} & V_{cb} \\ V_{td} & V_{ts} & V_{tb} \end{pmatrix} \begin{pmatrix} d \\ s \\ b \end{pmatrix} \tag{2.1}$$

which connects the weak eigenstates d', s', b' to their mass eigenstates d, s, b. Thus the quark that couples to the weak interaction charged bosons is a linear combination of the free (mass) eigenstates, and it can transform to another flavor through the interaction. In this picture, since V is unitary and 3×3, there is one irreducible imaginary phase in it. CP invariance of the Lagrangian for weak interactions is violated when the CKM matrix is a complex one, therefore CP violation is naturally explained. A similar strucure is speculated to exist also in the leptonic sector, since the neutrinos have been found to posess mass, described by the 3×3 Maki-Nakagawa-Sakata (MNS) matrix.

In the neutral-current weak processes, however, when a single Z^o is exchanged, a quark cannot transform into another quark with the same charge and a different flavor (e.g., $s \to d$). These FCNC processes are forbidden at the tree level, and suppressed at the one-loop level due to the Glashow-Iliopoulos-Maiani (GIM) mechanism [3]: the weak eigenstates, d' and s', not the mass eigenstates, d and s, participate in the weak interaction. Their relation is written as

$$\begin{pmatrix} d' \\ s' \end{pmatrix} = \begin{pmatrix} \cos\theta_C & \sin\theta_C \\ -\sin\theta_C & \cos\theta_C \end{pmatrix} \begin{pmatrix} d \\ s \end{pmatrix}, \tag{2.2}$$

where θ_C is called the Cabibbo angle [4]. The neutral current J^0, is expressed by the following description (omitting the γ-matrices):

$$\begin{aligned} J^0 &= \bar{u}u + \bar{c}c + \bar{d}'d' + \bar{s}'s' \\ &= \bar{u}u + \bar{c}c + (\bar{d}d + \bar{s}s)\cos^2\theta_C + (\bar{d}d + \bar{s}s)\sin^2\theta_C \quad &&: \text{(flavor conserving term)} \\ &\quad +(\bar{d}s + \bar{s}d - \bar{d}s - \bar{s}d)\sin\theta_C\cos\theta_C &&: \text{(flavor changing term)} \\ &= \bar{u}u + \bar{c}c + \bar{d}d + \bar{s}s. \end{aligned} \tag{2.3}$$

The term that accounts for the FCNC processes vanishes, and therefore the absence of the FCNC processes at the tree level is explained by this description. The GIM cancellation can also work at 1-loop diagrams, where the initial-to-final quark transitions are effectively the FCNC processes, if the quarks in the intermediate state (e.g., the u and c quarks in the $K^0 - \bar{K}^0$ mixing) have the same mass. Since the quark masses depend on the quark flavors, this cancellation is not perfect, and thus the FCNC processes are allowed as "rare decays" at higher orders.

The unitary CKM matrix has four independent parameters, which in leading order of the Wolfenstein parameterization [5] are A, λ, ρ and η. In terms of these parameters, the CKM matrix can be written as

$$\begin{pmatrix} V_{ud} & V_{us} & V_{ub} \\ V_{cd} & V_{cs} & V_{cb} \\ V_{td} & V_{ts} & V_{tb} \end{pmatrix} \simeq \begin{pmatrix} 1-\lambda^2/2 & \lambda & A\lambda^3(\rho - i\eta) \\ -\lambda & 1-\lambda^2/2 & A\lambda^2 \\ A\lambda^3(1-\rho-i\eta) & -A\lambda^2 & 1 \end{pmatrix} \tag{2.4}$$

where $\lambda = \sin\theta_c = 0.22$ is the sine of the Cabibbo angle, the mixing angle for the case of 2 quark generations initially studied by Cabibbo. One sole parameter η describes CP violation in the SM, since a non-zero value of this parameter breaks the CP invariance for weak interactions.

The values of the CKM matrix elements are not defined by any first principles, and can only be experimentally measured and constrained. The present values of the magnitudes are:

$$\begin{pmatrix} |V_{ud}| & |V_{us}| & |V_{ub}| \\ |V_{cd}| & |V_{cs}| & |V_{cb}| \\ |V_{td}| & |V_{ts}| & |V_{tb}| \end{pmatrix} \simeq \begin{pmatrix} [0.9736, 0.9741] & [0.2262, 0.2282] & [0.0039, 0.0041] \\ [0.2261, 0.2281] & [0.9727, 0.9732] & [0.0414, 0.0423] \\ [0.0075, 0.0085] & [0.0409, 0.0417] & [0.9991, 0.9991] \end{pmatrix} \tag{2.5}$$

at the 90% confidence level interval [6]. These values can either be determined directly from tree-level decays (e.g., the simplest, neutron beta decay, or $B \to \pi l\nu$) , or (particularly those involving couplings to the top quark) indirectly from flavor-changing second-order weak processes that involve the up-type quarks in an internal loop (e.g., $K^+ \to \pi^+\nu\overline{\nu}$). It is assumed that the dominant contribution to the processes comes from the t quark loop. The agreement or disagreement between the measured and predicted (based on

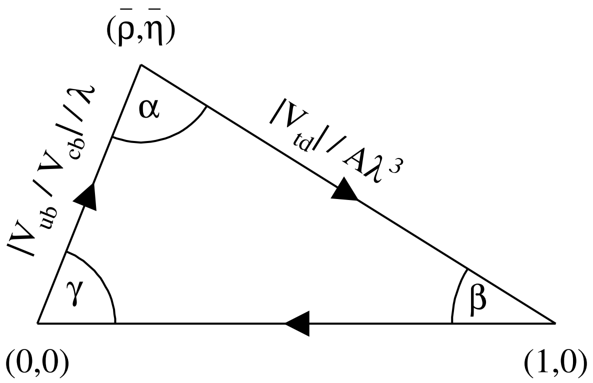

Figure 2.1: Unitarity triangle in the $\rho-\eta$ plane. Two sides of the triangle can be expressed by the CKM matrix elements $|V_{td}|/A\lambda^3$ and $|V_{ub}/V_{cb}|/\lambda$, respectively, where A and λ are parameters in the Wolfenstein parameterization.

independent measurements) quantities can put constraints on new physics.

All of the information concerning the CKM matrix elements can be summarized in terms of "unitarity triangles". The unitarity of this matrix can be expressed with 9 conditions, 6 of which (the ones for the off-diagonal elements) can be represented graphically in the form of triangles, all of which must have the same area. Applying the unitarity property $V^\dagger V = 1$ to the CKM matrix in (2.4) implies

$$V_{ub}^* V_{ud} + V_{cb}^* V_{cd} + V_{tb}^* V_{td} \simeq V_{ub}^* - \lambda V_{cb}^* + V_{td} = 0, \tag{2.6}$$

where the approximations $V_{ud} \simeq V_{tb}^* \simeq 1$ and $V_{cd} \simeq -\lambda$ have been made. This equation can be represented graphically, as shown in Fig. 2.1, where both sides of the equation have been divided by λV_{cb}^*. The apex of the triangle in the $\rho-\eta$ plane is given by two Wolfenstein parameters, $\bar{\rho}$ and $\bar{\eta}$, where $\bar{\rho} = \rho(1-\lambda^2/2)$ and $\bar{\eta} = \eta(1-\lambda^2/2)$.

The values of these parameters currently come from several measurements of B meson decays, as well as a measurement of the indirect CP violation parameter from $K^0 - \bar{K}^0$ mixing, ϵ_K, as shown in Fig. 2.2. All these measurements agree to a very good level and the $\rho - \eta$ parameters are well constrained. However, it is desirable to over-constrain the position of the apex in as many independent ways as possible, because any disagreement among the independent measurements would indicate the presence of new physics that contains new sources of CP violation. Such sources are expected to exist, because the parameters for CP violation in the SM are not sufficient to explain the observed matter-antimatter asymmetry of the Universe. An especially powerful probe for such new physics is the comparison of the results from B meson and kaon decays with small theoretical ambiguities. In other words, since the CKM phase should be the only source of CP violation within the SM, precise measurements of all the CKM matrix elements are crucial.

The determination of ρ and η independently from B and K decays, as shown in Fig. 2.3, can be examined in two ways:

- A comparison of the angle β from the ratio $BR(K_L^o \rightarrow \pi^o \nu\bar{\nu})/BR(K^+ \rightarrow \pi^+ \nu\overline{\nu})$ and from CP violation asymmetry ($\mathcal{A}_{CP}$) in the decay $B_d^0 \rightarrow J/\psi K_s^0$.
- A comparison of the magnitude $|V_{td}|$ from $K^+ \rightarrow \pi^+ \nu\overline{\nu}$ and from the mixing frequencies of B_s and B_d mesons, expressed in terms of the ratio of the mass differences, $\Delta M_{B_s}/\Delta M_{B_d}$.

The motivation to search for $K^+ \rightarrow \pi^+ \nu\overline{\nu}$ also stems from a desire to measure the small, imprecisely-determined CKM matrix element $|V_{td}|$, as well as to search for non-SM physics.

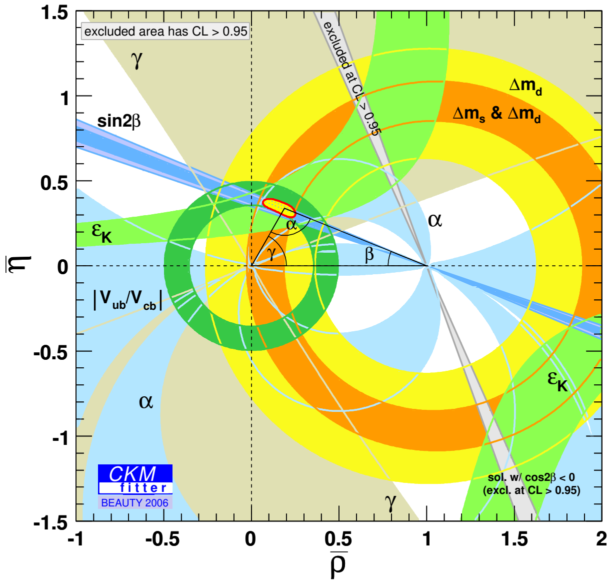

Figure 2.2: The global CKM fit results for the unitarity triangle, using the latest B and K measurements ([7]). The following constrain areas can be seen: the green annular area comes from the rates of tree-level semileptonic B decays, the orange and yellow ones from B meson oscillation parameters, the blue wedge around angle β, as well as the light blue and brown constrains in the other angles, from CP asymmetries in the rates of hadronic B decays, and the light green hyperbola from indirect CP violation in $K^0 - \bar{K}^0$ mixing.

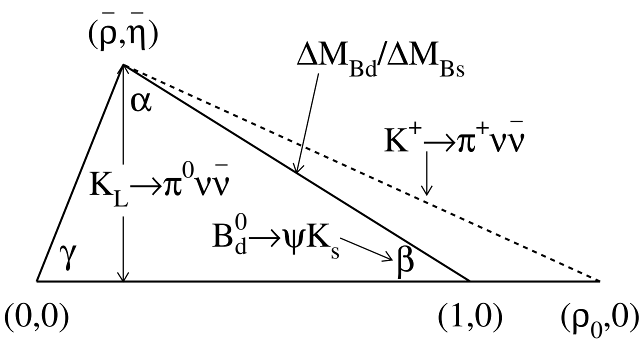

Figure 2.3: Unitarity triangle determined by B and K decays.

2.3 $K^+ \to \pi^+\nu\overline{\nu}$in the Standard Model

The decay $K^+ \to \pi^+\nu\overline{\nu}$ is a FCNC process that is prohibited in the first order (see Fig. 2.4).

However, this decay is allowed in the second order, and is described by a box diagram and two Z-penguin diagrams, as shown in Fig. 2.5.

The weak amplitude for this process is represented as

$$\mathcal{M} \sim \sum_{i=u,c,t} V_{is}^* V_{id} \frac{\gamma^\mu q_\mu + m_i}{q^2 - m_i^2}, \tag{2.7}$$

where the V_{ij}'s are the CKM matrix elements, the γ^μ's are the Dirac matrices, q_μ is the momentum transfer, and the m_i's are the quark masses. $\mathcal{M}$ vanishes if all of the quark masses m_i, are equal, because of the unitarity of the CKM matrix. However, the breaking of flavor symmetry, which results in the different quark masses, allows this decay to proceed at a very small rate. Since the top quark violates the quark mass equality at a maximum, its contribution to the $K^+ \to \pi^+\nu\overline{\nu}$ branching ratio is the largest. This decay is sensitive to the weak coupling of top to down quarks, given by the CKM matrix element V_{td}.

The branching ratio for $K^+ \to \pi^+\nu\overline{\nu}$ is calculated by following the convention in [8] and [9]. The effective Hamiltonian can be written in the SM as

$$\mathcal{H}_{eff}^{SM} = \frac{G_F}{\sqrt{2}} \frac{\alpha}{2\pi \sin^2 \Theta_W} \sum_{l=e,\mu,\tau} (V_{cs}^* V_{cd} X^l(x_c) + V_{ts}^* V_{td} X(x_t))(\bar{s}d)_{V-A}(\bar{\nu}_l \nu_l)_{V-A}, \tag{2.8}$$

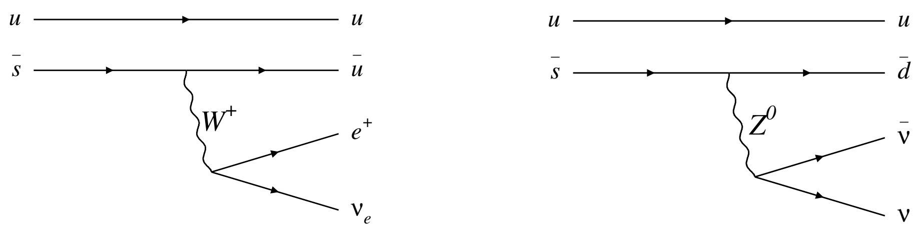

Figure 2.4: Feynman diagram for the weak decay $K^+ \to \pi^o e^+ \nu_e$, which is allowed in the SM (left). Feynman diagram for the $K^+ \to \pi^+ \nu \overline{\nu}$ decay in a tree level, which is not allowed (right).

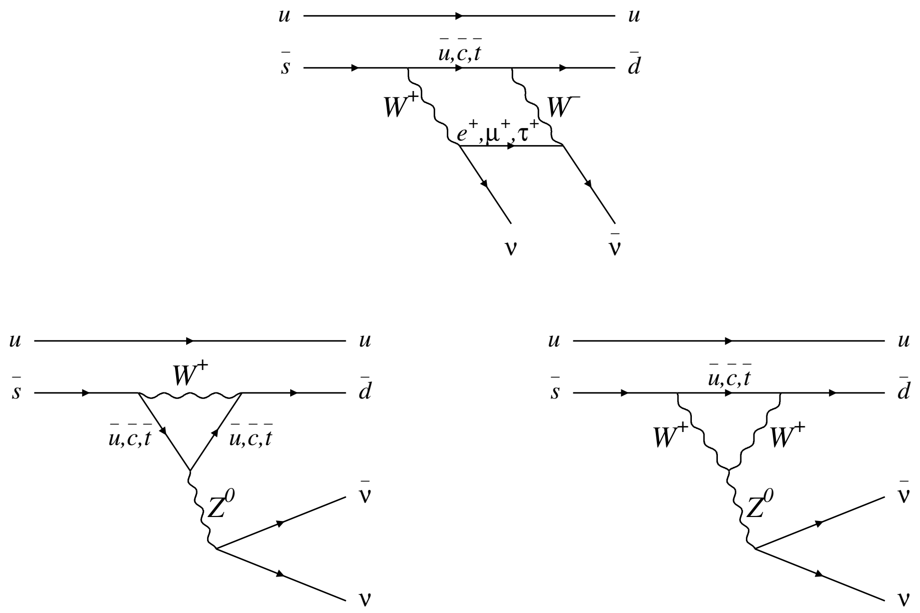

Figure 2.5: Second-order weak processes that contribute to the $K^+ \to \pi^+ \nu \overline{\nu}$ branching ratio: the "box" diagram (upper) and two "Z-penguin" diagrams (bottom).

where $X(x_j)$ are functions of $x_j \equiv m_j^2/M_W^2$ summarizing the top and charm quark contributions in the loop, including QCD corrections at the next-to-leading-order (NLO) level. The up quark term has been removed using the unitarity of the CKM matrix. The dependence on the charged lepton mass in the loop is negligible for the top quark contribution, but not for the charm quark for the case of tau lepton. Therefore the perturbative charm contribution is described in terms of the parameter

$$P_c(X) \equiv \frac{1}{\lambda^4}(\frac{2}{3}X^e + \frac{1}{3}X^\tau) = 0.369 \pm 0.036_{theory} \pm 0.033_{m_c} \pm 0.009_{a_s} \qquad (2.9)$$

where $\lambda = \sin\theta_c = 0.2248$ has been used. The errors on the right-hand side of (2.9) correspond to the uncertainty in the charm mass, m_c and the coupling constant, $\alpha_s(M_Z^2)$.

The theoretical uncertainty in the dominant top contribution is very small, and is essentially determined by the experimental error on the top quark mass, m_t. With the top quark mass in the minimal subtraction ($\overline{MS}$) scheme $m_t = (163.0 \pm 2.8) GeV$ ([9]),

$$X(x_t) = 1.464 \pm 0.041 \qquad (2.10)$$

is obtained. The largest theoretical uncertainty in estimating BR($K^+ \to \pi^+\nu\overline{\nu}$) originates from the charm contribution.

With these definitions the branching ratio for $K^+ \to \pi^+\nu\overline{\nu}$ can be written as

$$BR(K^+ \to \pi^+ \nu\overline{\nu}) = \kappa_+ \left[\left(\frac{\mathrm{Im}\lambda_t}{\lambda^5} X(x_t) \right)^2 + \left(\frac{\mathrm{Re}\lambda_c}{\lambda} P_c(X) + \frac{\mathrm{Re}\lambda_t}{\lambda^5} X(x_t) \right)^2 \right] \tag{2.11}$$

where

$$\kappa_+ \equiv r_+ \frac{3\alpha^2 BR(K^+ \to \pi^0 e^+ \nu)}{2\pi^2 \sin^4 \theta_W} \lambda^8 = (5.04 \pm 0.17) \times 10^{-11} \left[\frac{\lambda}{0.2248} \right]^8 \tag{2.12}$$

and the λ_j's ($\equiv V_{js}^* V_{jd}$) are from the CKM matrix elements. The r_+ ($=$ 0.901) represents isospin breaking corrections in relating $K^+ \to \pi^+ \nu\overline{\nu}$ to the well-measured leading decay $K^+ \to \pi^0 e^+ \nu$ [10]. In obtaining the numerical value in (2.12), we used [11]

$$\sin^2 \theta_W = 0.231, \qquad \alpha = \frac{1}{127.9}, \qquad BR(K^+ \to \pi^0 e^+ \nu) = (4.93 \pm 0.07) \times 10^{-2}. \tag{2.13}$$

Employing the improved Wolfenstein decomposition of the CKM matrix [12], expression (2.11) describes in the $\bar{\rho} - \bar{\eta}$ plane an ellipse with a small eccentricity, namely

$$(\sigma\bar{\eta})^2 + (\bar{\rho} - \bar{\rho}_0)^2 = \frac{\sigma \mathcal{B}(K^+ \to \pi^+ \nu\bar{\nu})}{\bar{\kappa}_+ |V_{cb}|^4 X^2(x_t)}, \tag{2.14}$$

where

$$\bar{\rho}_0 \equiv 1 + \frac{\lambda^4 P_c(X)}{|V_{cb}|^2 X(x_t)}, \sigma \equiv \left(1 - \frac{\lambda^2}{2}\right)^{-2}, \overline{\kappa}_+ \equiv \frac{\kappa_+}{\lambda^8} = (7.64 \pm 0.09) \times 10^{-6}. \tag{2.15}$$

Using (2.11) and the next-to-next-to-leading-order (NNLO) calculations in [9], the branching ratio of $\pi\nu\overline{\nu}$ is predicted to be

$$\mathcal{B}(K^+ \to \pi^+ \nu\bar{\nu}) = (8.0 \pm 1.1) \times 10^{-11} \tag{2.16}$$

within the SM. It should be noted that, for an uncertainty of 15% in (2.16), the theoretical uncertainty is ~7% at present, mainly due to the charm quark contribution.

The measurement of BR($K^+ \to \pi^+\nu\overline{\nu}$) is regarded to be one of the cleanest ways to extract $|V_{td}|$ for the following reasons:

- Long-distance contributions to the branching ratio are negligible (at most 10^{-13}) [13].
- The uncertainty from the hadronic matrix element has been removed by using $BR(K^+ \to \pi^0 e^+ \nu)$.
- The remaining theoretical uncertainties (7%) are relatively small and reliable as compared with the errors in other K and B decays.

2.4 Physics beyond the Standard Model

Since $K^+ \to \pi^+\nu\overline{\nu}$ is a second order process, a precise measurement of the branching ratio can investigate whether there are non-SM effects involved in

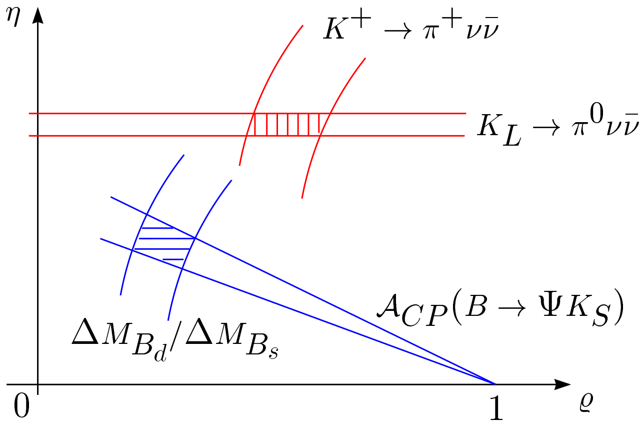

Figure 2.6: Schematic determination of the unitarity triangle apex (ρ,η) from the B system (blue) and from the $K \to \pi\nu\bar{\nu}$ decays (red). Both determinations can be performed with small theoretical uncertainties, therefore any discrepancy between them, as illustrated in this hypothetical example [14], would indicate new physics.

this decay mode or not. A possible discrepancy between the measured branching ratio and the SM prediction would indicate the existence of new physics beyond the SM. What can be performed is to determine ρ and η independently from the K and B decays, as shown in Fig. 2.6.

The information that is currently being used to constrain the unitarity triangle is obtained only from the charged current processes (i.e. tree-level amplitudes) and the $\Delta F = 2$ ($F = S, B$) loop-induced processes. For example, determinations of ρ and η can be obtained from the $B_d^0 - \bar{B}_d^0$ mixing and the CP violating asymmetry in $B_d^0 \to J/\psi K_s^0$, both of which are mediated by $\Delta B = 2$ loop-induced processes. On the contrary, $K^+ \to \pi^+\nu\overline{\nu}$ and $K_L^0 \to \pi^0\nu\bar{\nu}$ are mediated via the $\Delta S = 1$ FCNC transition. New physics may therefore be seen in a discrepancy between K and B decays [14].

Several SM extensions to new physics would affect the $\pi\nu\overline{\nu}$ branching ratio. In the Minimal Flavor Violation (MFV) model, the $\pi\nu\overline{\nu}$ branching ratio is allowed to be as large as 1.9×10^{-10} [15]. In this model, the origin of CP violation and quark mixing comes from the CKM matrix as in the SM, and from process-independent universal master functions, which are real and which in the SM reduce to the Inami-Lim functions.

In the "Enhanced Z^0 Penguin" model [16], where a new imaginary phase is introduced, the $\pi\nu\overline{\nu}$ branching ratio is expected to be almost the same as the SM prediction. However, the $K_L^0 \to \pi^0\nu\bar{\nu}$ branching ratio is predicted to be $(3.1 \pm 0.1) \times 10^{-10}$, which is 10-times larger than the SM prediction, and is close to the Grossman-Nir limit, $BR(K_L^0 \to \pi^0\nu\bar{\nu})/BR(K^+ \to \pi^+\nu\overline{\nu}) < 4.4$ [17]. Another interesting prediction derived from this model is that the value of $\sin 2\beta$ obtained from $K \to \pi\nu\bar{\nu}$ is not equal to that obtained from $B_d^0 \to J/\psi K_s^0$.

Chapter 3

The experiment

3.1 Introduction

3.2 Experimental Overview

The experimental signature of the $K^+ \to \pi^+\nu\overline{\nu}$ decay is a single π^+ track and no other particle from a K^+ decay, because the two neutrinos in the final state cannot be detected in the apparatus. $K^+ \to \pi^+\nu\overline{\nu}$ is a three-body decay with a maximum momentum of 227 MeV/c, and it has been traditionally searched for by the experiments E787 and E949 in two kinematic regions: "PNN1" and "PNN2" (the region studied in this analysis). The momentum definition of these regions, together with the momentum spectra of the outgoing charged particle (pion or muon) of the main background mechanisms relevant to PNN2, are shown in Fig. 3.1. Their Branching Ratios are listed in Table 3.1. As it can be seen, the upper bound of PNN2 is very close to the momentum (and energy and range) of the major 2-body decay $K_{\pi 2}$.

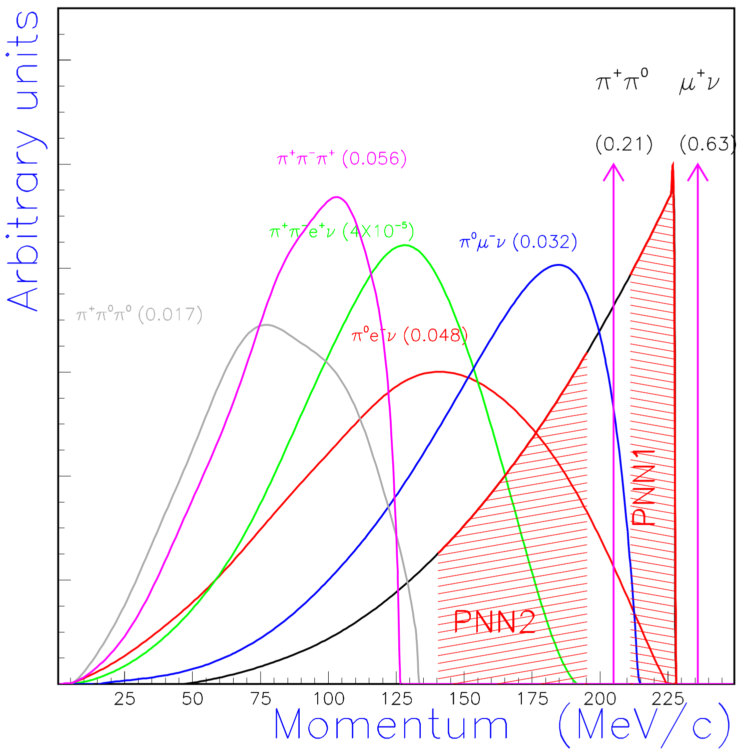

Figure 3.1: Momentum spectra of the charged product of the top 7 K^+ decay modes. The SM $K^+ \to \pi^+\nu\overline{\nu}$ spectrum is also shown (not in scale).

Since, in the SM, the branching ratio of $K^+ \to \pi^+\nu\overline{\nu}$ is expected to be at $\sim 10^{-10}$, all other kaon decay modes and beam pions that scatter into the detector acceptance could be sources of background. Therefore, precice kinematic measurements, positive particle identification of the incoming K and the outgoing π, and efficient vetoing of all other decay products (mainly photons) is required to suppress these backgrounds to an acceptable level. The E949 detector has been designed with these requirements in mind, specifically:

- The beam intensity should be as high as possible, since the decay rate

Background	Branching Ratio ($\times 10^{-3}$)
$K^+ \to \pi^+\pi^o$ ($K_{\pi 2}$)	212.0
$K^+ \to \pi^+\pi^o\gamma$ ($K_{\pi 2\gamma}$)	0.275
$K^+ \to \pi^o\mu^+\nu$ ($K_{\mu 3}$)	31.8
$K^+ \to \mu^+\nu\gamma$ ($K_{\mu 2\gamma}$)	5.5
$K^+ \to \pi^+\pi^- e^+\nu$ (K_{e4})	0.039
Beam backgrounds	-
CEX: $K^+ n \to K^o p$	prob = 0.0015
$K^o_L \to \pi^+\mu^-\overline{\nu}$	135.0
$K^o_L \to \pi^+ e^-\overline{\nu}$	194.0

Table 3.1: Background processes to the decay $K^+ \to \pi^+\nu\overline{\nu}$ in the kinematic region below the $K_{\pi 2}$ peak, with their Branching Ratios. CEX stands for Charge Exchange.

is extremely rare.

- Pion contamination in the kaon beam should be reduced to be as low as possible to minimize events with the scattered pion beam (Pion Scattering events).

- Detectors along the beam path are installed, in order to assure the PID of the incoming particle and to veto on other particles arriving around the decay time.

- A series of detectors give precise kinematic measurements, in order to suppress the $K^+ \to \pi^+\pi^o$ background: the active Target (TG) and two momentum degraders are designed to stop the incoming Kaon and measure its arrival time. The TG is surrounded by a drift chamber (UTC) immersed in a 1T magnetic field, in order to measure the outgoing particle momentum. Then the charged decay product comes to a rest in a stack of scintillators (RS), where its total energy and range are measured.

- The charged particle should be identified as π^+, which is achieved by observing the $\pi^+ \to \mu^+ \to e^+$ decay sequence in the stopping counter of the RS. This helps to suppress muon backgrounds.

- Any particles other than π^+ from K^+ decay should be detected and rejected. Photon veto detectors cover the detector at 4π, and the TG can detect extra short-range charged decay products.

The BNL-E949 experiment [18] is a successor to the experiment BNL-E787, whose data taking was completed in 1998. The beam and apparatus are similar to those of E787, but several upgrades have been made:

Beam

- The proton intensity increased by a factor of two compared to E787, which resulted in a twice higher kaon intensity than that in E787.

Detector

- A new lead/scintillator sandwich sampling calorimeter (Barrel Veto Liner, BVL) was installed in the barrel region, which added 2.3 radiation lengths to the photon vetos. Also installed were photon detectors that cover small solid angles near the beam line: the Active Degrader (AD) and Upstream Photon Veto (USPV) in the upstream, and the Downstream Photon Veto (DSPV) in the downstream.

- One third of the plastic scintillators in the π^+ range counters were replaced, which enabled us to achieve greater outputs of light.

- A gain monitor system, operated by blue LED flashers, was installed in the RS. The gain fluctuations of a phototube could be tracked down spill by spill, or even within a spill. This resulted in more precise energy calibration.

- The electronics for the drift chamber and straw chambers embedded in the RS were modified to meet the high rates.

- Signals from several beam counters were read out by waveform digitizers. Signal pileup due to the high beam intensity was solved by pulse-shape analysis.

Trigger and DAQ

- The level 0 trigger board was upgraded [19].

- Digital mean-timer modules were used for online photon rejection [19]. This helped to avoid any accidental loss in the trigger.

In the following sections, details concerning the E949 experiment are described.

3.3 The beam

The K^+ beam is produced by a high-intensity proton beam from the Alternating Gradient Synchrotron (AGS) at BNL. A schematic view of the AGS accelerator complex is shown in Fig. 3.2.

Protons are accelerated to a momentum of 21.5 GeV/c. 65 trillion protons (Tp) are extracted in a 2.2-second long "spill" once every 5.4 seconds from the

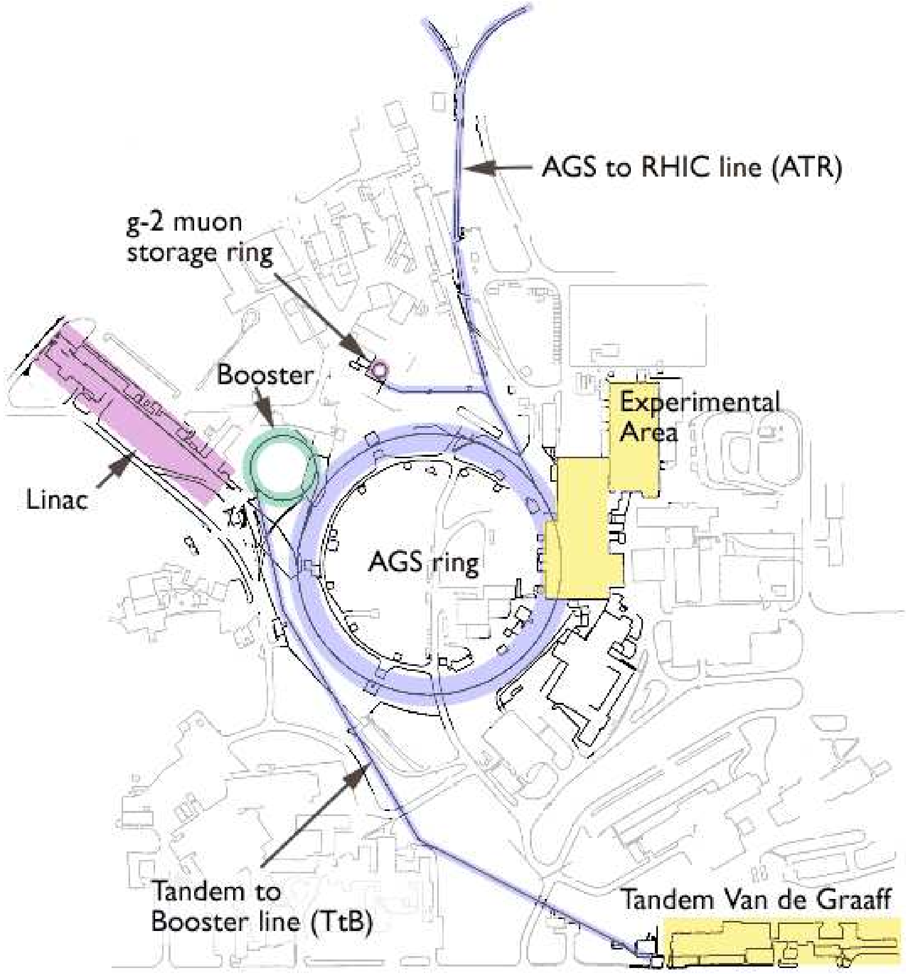

Figure 3.2: Schematic view of the AGS complex, which consists of a 200 MeV LINAC, a booster and a synchrotron. The secondary beam lines are located in the experimental area.

AGS. The slow extracted beam (SEB) is transported to the kaon production target for E949. The platinum production target extends 6 cm to the beam direction, and is located on a water-cooled copper base. Under typical AGS running conditions, 45 Tp hit the production target every 2.2 second spill at 21.5 GeV/c.

The Low Energy Separated Beam line III [20] (LESBIII, shown in Fig. 3.3) collects and focuses kaons produced at the production target. The beam emitted toward 0 degrees contains about 500 pions and 500 protons for every kaon, and is momentum-selected by a dipole magnet (D1 in Fig. 3.3). Two electrostatic separators (Separators 1 and 2 in Fig. 3.3) sweep pions and protons out of the beam. The resulting beam is further selected by a second dipole magnet (D2 in Fig. 3.3). LESBIII contains a number of focusing quadrupole (Q1-10), sextupole (S1-3), and octupole (O1) magnets and collimating slits, and has a total length of 19.6 m from the production target to the E949 target. Kaons with 710 MeV/c momentum were transported down this beamline.

The angular acceptance of LESBIII is 12 msr and the momentum acceptance is 4.5% FWHM. LESBIII provides the world's highest-intensity kaon beam of 710 MeV/c with a flux of about 5×10^5 K^+'s per Tp on the production target. The $K^+ : \pi^+$ ratio in the beam is about 3:1 [1]. Proton contamination is negligible due to a large deflection of protons by the separators. Under the typical AGS running condition of 45 Tp on the production target per spill, 1.3×10^7 K^+'s emerge from LESBIII.

[1] The K/π ratio in E787 was 4:1. This worse K/π ratio was due to a problem with the second separator.

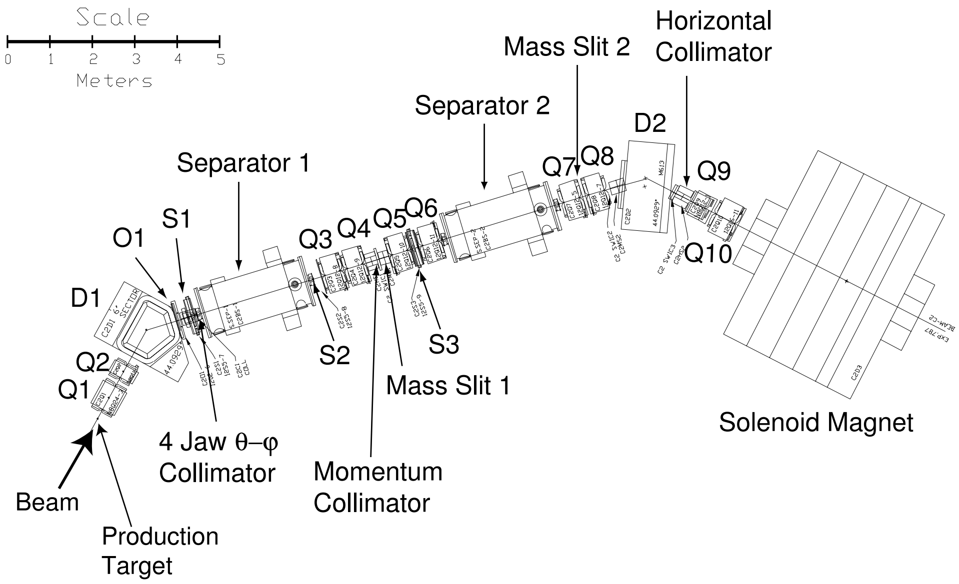

Figure 3.3: Low-energy separated beam line III at BNL.

3.4 The detector

A side view of the E949 detector is shown in Fig. 3.4. The E949 detector consists of beam instrumentation, a target of scintillating fibers, a central drift chamber, a stack of plastic scintillators (Range Stack), and hermetic photon detectors.

The whole detector is surrounded by a solenoid magnet with a 1 Tesla magnetic field along the beam line for momentum measurements. The coordinates of the detector are defined such that the origin is at the center of the target; the z-axis is along the beam direction and the x-axis and y-axis are set in the horizontal and vertical directions, respectively.

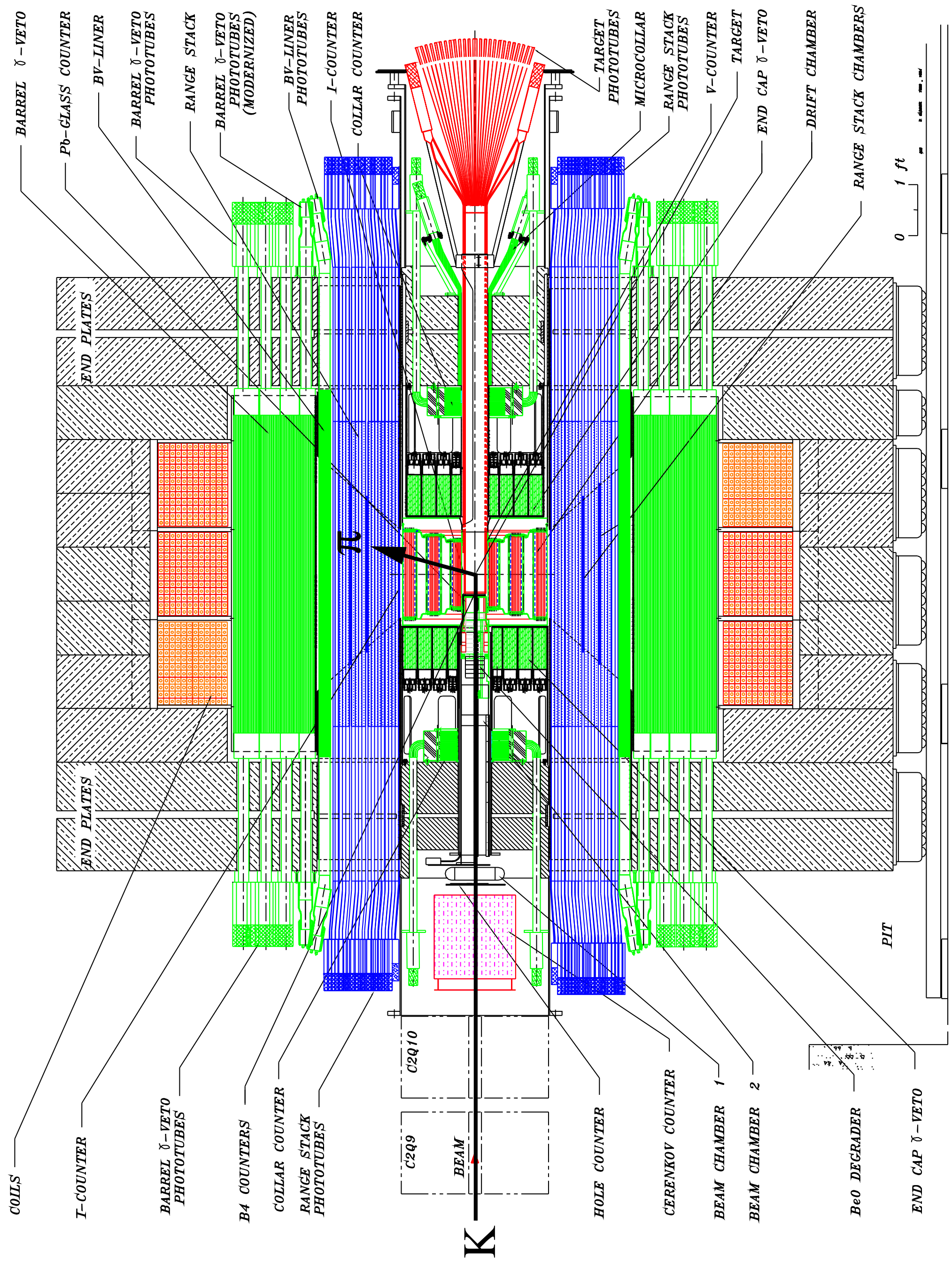

Figure 3.4: Side view of the E949 detector.

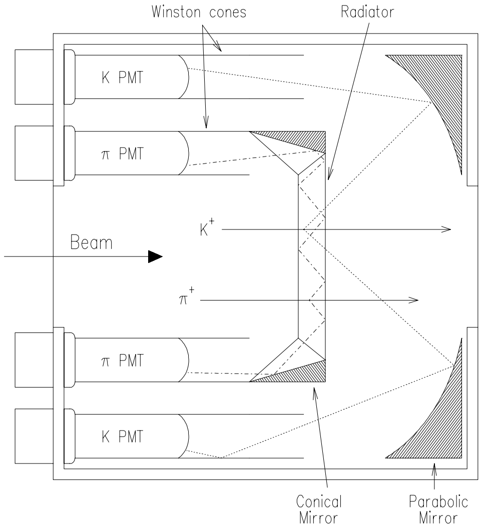

Figure 3.5: Side view of the Čerenkov counter.

3.4.1 Beam detectors

Since the beam intensity is very high and the beam contains pions with a ratio of $K^+ : \pi^+ = 3:1$, a single kaon entering the target should be identified by the beam instrumentation. It has three roles: kaon identification, slowing down the kaon, and the detection of extra beam particles if they exist at the kaon beam time or the kaon decay time. The beam instrumentation from upstream to downstream consists of a Čerenkov counter, the Upstream Photon Veto detector, beam wire chambers, degraders and a beam hodoscope.

The kaon beam from LESBIII first enters the Čerenkov counter located just downstream of the last quadrupole magnet (Q10) and 2 m upstream of the target. A side view of the Čerenkov counter is shown in Fig. 3.5.

The reflection index (n) of the radiator is 1.49, which gives a threshold of Čerenkov radiation $\beta_{\check{C}} = 1/n = 0.671$ and a reflection threshold $\beta_{ref} = \sqrt{\frac{1}{n^2-1}} = 0.905$. Kaons and pions with a momentum of 710 MeV/c have

$\beta_{K^+} = 0.821$ and $\beta_{\pi^+} = 0.981$, respectively. Therefore, the Čerenkov light from kaons is not reflected at the inner surface of the radiator, but from pions is. The light from a kaon exits the radiator and is reflected by a parabolic mirror to the outer ring of 14 photomultiplier (PMT) tubes (Kaon Čerenkov Counter), while that from a pion is internally reflected within the radiator and detected in the inner ring of 14 PMTs (Pion Čerenkov Counter).

The PMT signals are fed to time-to-digital converters (TDCs) via discriminators, as well as to 500 MHz transient digitizers based on gallium-arsenide (GaAs) charge-coupled devices (CCDs) [21]. The pulse-height information in every 2 ns interval is recorded in the CCDs to reproduce the time development of the pulses.

A charged particle passing through the Čerenkov counter fires a number of PMTs in the Kaon or Pion Čerenkov Counters; PMT hits coincident with each other are called a "cluster". A kaon is identified by requiring that the Kaon Čerenkov Counter has a hit cluster and the Pion Čerenkov Counter has no hit cluster.

Two incoming particles close in time can fire the same PMTs, and a pileup signal may not be found by the TDCs. In this case, the pulse shapes recorded in the CCDs can be used to discriminate such pileup signals.

Right downstream of the Čerenkov counter there is the Upstream Photon Veto (USPV) detector. This is made of 12 layers of 28.4 cm^2 plastic scintillator sheets, 2 mm thick, alternating with 1 mm (the 6 most downstream ones) or 2 mm (the 5 most upstream ones) thick lead sheets (see fig ...The downstream-most layer of lead was replaced by 2.2 mm thick copper, which formed part of the box holding the layers together. The upstream side of the box is made by

3.175 mm thick aluminum. The detector has a 175 mm wide by 40 mm high slot in the center to allow the beam to pass through, and is divided horizontally in 2 modules, each read out by one PMT. Each scintillator layer was read out by 21 WLS fibers going to one of these 2 PMTs. Then the signals from each PMT were fed to a TDC, an ADC and a CCD.

Although the USPV was originally designed as a photon veto detector for the photons that might escape in the beam direction, it was found that its rate was overwhelmed by beam particles and its segmentation into only 2 modules did not give enough space resolution to distinguish between them and upstream-going photons. Therefore its time, energy and CCD pulse information was used to veto beam particles coincident with the kaon decay time.

Behind the USPV, two Beam Wire Projection Chambers (BWPCs) are located, and allow to monitor the beam profile and to identify multiple incoming particles. Cross-sectional views of the BWPCs are shown in Fig. 3.6.

The first chamber (BWPC1) consists of 3 planes of anode wires, labeled U, V and X. The direction of the wires in the X-plane is vertical, and in the U- and V-planes are at $\pm 45^o$ to the vertical plane respectively. The wires are made of gold-plated tungsten with 0.012 mm diameter. The BWPC1 has 72, 60 and 60 readout channels for the X-, U- and V-planes, respectively, with a 2.54 mm wire spacing. The spacial resolution is 1.54 mm, and the active area is 178 mm (horizontal) by 50.8 mm (vertical). The cathode foils are 0.025 mm thick aluminized mylar coated with carbon. The anode-cathode distance is 3.175 mm, and the total thickness of the BWPC1 is approximately 56 mm. The BWPC1 is filled with a mixture of CF4 (80%) and Isobutane (20%).

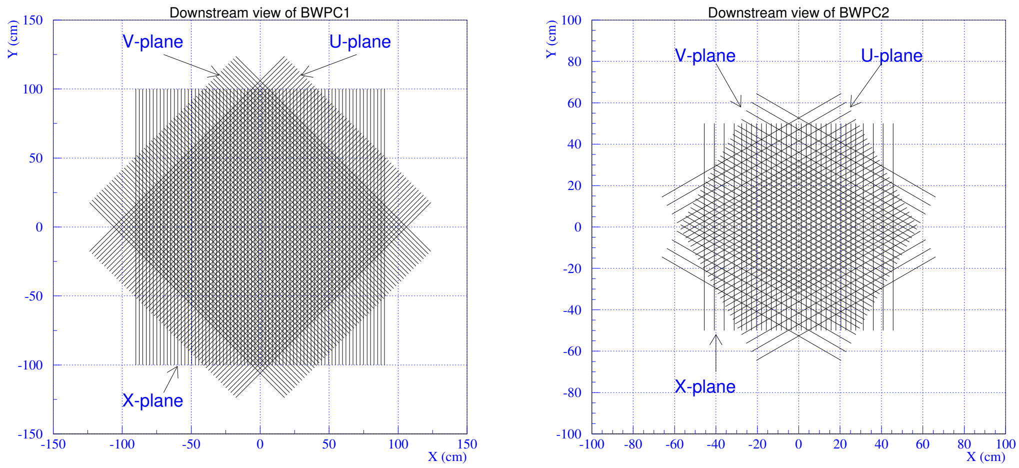

Figure 3.6: Cross-sectional view of the two beam wire chambers (BWPCs): BWPC1 (left) and BWPC2 (right).

The second chamber (BWPC2) is located at 90 cm downstream of the BWPC1 and consists of three planes (U, V and X). Each plane has 24 readout channels with a 2.40 mm wire spacing in the central region (57.6 mm) and 8 channels with a 4.80 mm wire spacing in the peripheral region (19.2 mm on each end). The cathode foils are 0.008 mm single-side aluminized mylar coated with carbon. The anode-cathode distance is 1.5875 mm. The BWPC2 is filled with the same gas as BWPC1.

Downstream of the BWPCs, cylindrical degraders are located for slowing down the kaons so that they come to rest in the target. The degraders have inactive and active parts. The upstream inactive degrader is made of 111.1 mm long beryllium oxide (BeO) and 4.76 mm Lucite. The total thickness is appropriate for stopping kaons with a momentum of 710 MeV/c. BeO, with high density and low atomic number, minimizes multiple scattering.

The downstream active degrader (AD) consists of 40 layers of 2 mm thick

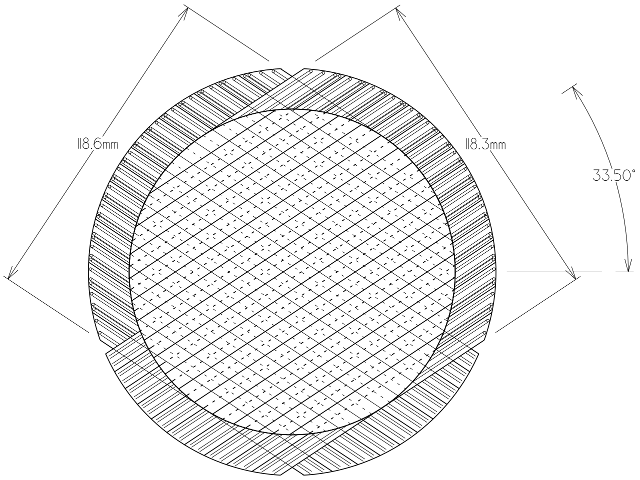

Figure 3.7: End view of the B4 Hodoscope.

scintillator disks (139 mm in diameter) alternating with 2-mm thick copper disks (136 mm in diameter). The AD is split into 12 azimuthal segments, and the scintillation light in each segment is sent to a single PMT through 14 wave length shifting (WLS) fibers running in grooves cut into the perimeter of the disks. The PMT outputs are fed to TDCs and CCDs. The signals from 4 PMTs are multiplexed and fed to a single analog-to-digital converter (ADC). Using this information, the AD has the ability to identify the beam particles and to detect activity coincident with kaon decays.

After passing through the degraders, just in front of the target, a beam hodoscope (B4 Hodoscope) detects the incoming particle and identifies it as a kaon or pion by measuring the energy deposit. An end view of the B4 Hodoscope is shown in Fig. 3.7.

The B4 Hodoscope consists of two planes (U- and V-plane, 119 mm in diameter) to provide position information. Each plane has 12 scintillator fingers. The cross section of the finger has a "Z-shape", as shown in Fig. 3.8,

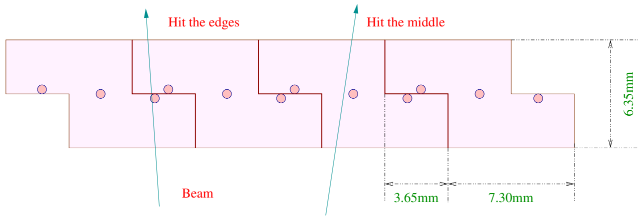

Figure 3.8: Schematic cross section of the B4 Hodoscope.

with a 6.35-mm thick middle part and 3.175-mm thick edge parts. This shape allows the B4 Hodoscope to have no inactive region and improves its spatial resolution.

In each finger, 3 WLS fibers are embedded and fed to a single PMT that is read out by TDCs, ADCs and CCDs. A double-pulse fitting is performed to the signals recorded in the CCDs in order to detect pileups. The time development of the output signals is fitted with single- or double-pulse assumption, which allows to reject events if the fitted pulse is more likely to be a double pulse and the time of the second pulse is coincident with the K^+ decay time.

The B4 is surrounded by a ring of scintillator, the Ring Veto (RV), which covers the crack between the B4 and the I-Counter (described later). It is 3.27 mm thick, with an outer diameter of 145.5 mm, and as long as the B4 hodoscope. The RV is segmented vertically to 2 modules, each one read out seperately and with its signals sent to a TDC, an ADC and a CCD.

3.4.2 Target (TG)

After passing through all the beam elements and being slowed down by the degraders, 3.9×10^6 kaons per spill enter the scintillating fiber target located in the center of the spectrometer. Kaons lose more energy, come to rest, and

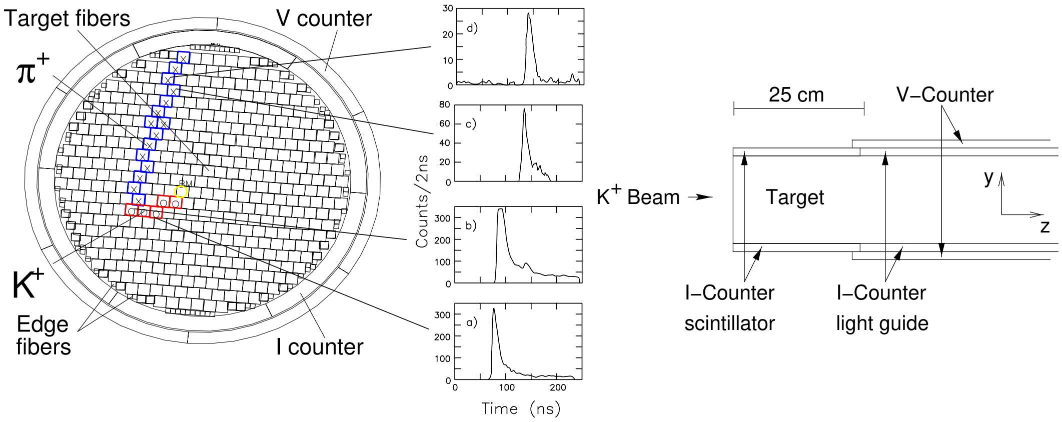

Figure 3.9: End (left) and side (right) views of the target. The CCD pulse-shape information is used to find kaon and pion clusters, as shown in the left figure. The lower two plots ((a) and (b)), are CCD pulses for a kaon, and the upper two plots ((c) and (d)), are those for a pion. Two layers of 6 plastic scintillators, the I-Counter (IC) and V-Counter (VC), surround the target.

decay in the target.

The TG consists of 413 5-mm square and 3.1-m long plastic scintillating fibers that are bundled to form a 12-cm diameter cylinder. A number of smaller fibers (called "edge fibers") fill the gaps near the outer edge of the TG. End and side views of the target are shown in Fig. 3.9.

Each of the 5.0-mm fibers is connected to a PMT, whereas the edge fibers are multiplexed into groups of 12 and each group is connected to a single PMT. The PMTs are read out by ADCs, TDCs and CCDs. Kaons, whose velocities are small, typically lose a large amount of energy (few tens MeV) in each fiber, while pions from kaon decays lose about 1 MeV per fiber, since they travel as minimum ionizing particles (MIPs). Pattern recognition is performed to find fibers that belong to a kaon's path or a pion's path. The CCD pulse information is used to find clusters for kaons (kaon fibers) and pions (pion fibers). A double-pulse fitting is also performed to find the fiber where a

$K^+ \to \pi^+$ decay vertex is located and to estimate the energy loss and range of the pion hidden in the kaon fiber.

The fiducial region of the target is defined by two layers of 6 plastic-scintillating counters that surround the target (see Fig. 3.9). The inner scintillators, called I-Counter (IC), tag charged decay products for a trigger before they enter the drift chamber. The IC is 6.4 mm thick at an inner radius of 6.0 cm, and extends 24 cm downstream from the upstream face of the target. Each scintillator is instrumented with a PMT, and is read out by an ADC, a TDC and a 500 MHz transient digitizer based on flash ADC (TD) [22].

The outer scintillators, called the V-Counter (VC), overlap the downstream edge of the IC by 6 mm, and serve to detect particles that decay downstream of the fiducial region of the target. The VC is 5 mm thick and 1.96 m long, and is staggered with respect to the IC. Each scintillator is instrumented with a PMT, which is read out by an ADC and a TDC.

3.4.3 Drift Chamber (UTC)

The drift chamber, called "Ultra Thin Chamber" (UTC), is located just outside of the IC. The whole E949 spectrometer is in a 1 Tesla magnetic field. Positively charged particles are bent clockwise in the view from downstream. The primary functions of the UTC are measuring the momentum of charged particles and providing a matching between the tracks in the target and in the Range Stack.

The UTC has a length of 51 cm and inner and outer radii of 7.85 cm and 43.31 cm respectively. It is composed of 12 layers of drift cells, grouped into 3

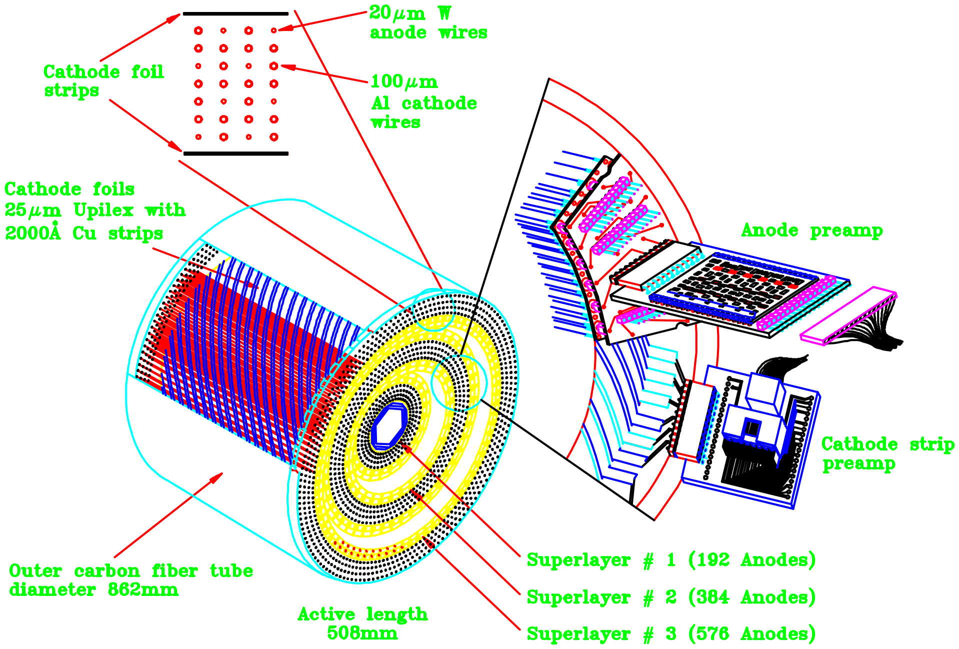

Figure 3.10: Schematic view of the Ultra Thin Chamber.

superlayers. The inner superlayer has 4 layers of 48 cells, the middle superlayer has 4 layers of 96 cells, and the outer superlayer has 4 layers of 144 cells (shown in Fig. 3.10).

Each cell is composed of 9 wires strung axially. A single anode wire, made of gold-coated tungsten with a 20 μm diameter, is surrounded by 8 cathode wires made of gold-coated aluminum with a 100 μm diameter, which are arranged in a square. Adjacent cells share the cathode wires at the boundaries. The cells in each layer are staggered by one-half cell with respect to the neighboring layers, in order to resolve a left-right ambiguity. The superlayers are filled with a mixture of argon (49.6%), ethane (49.6%) and ethanol (0.8%) gases. The cathode wires are grounded, and the anode wires are maintained at 2 kV (gain = 8×10^4, drift velocity = 5 cm/μs). Each anode wire is instrumented with an ADC and a TDC. The drift time to the anode wires provides (x, y)

positions for charged tracks.

The inner and outer radii of each superlayer have helical arrays of cathode strips, whose pitch angle is 45^o. The strips, with a width of 7 mm, are made of 1200 Å thick copper coated with 300 Å thick nickel, and are mounted on a 25 μm thick Kapton foil. The separation between the strips is 1 mm. The cathode foils have 48, 72, 108, 144, 180, and 216 strips from the inner to the outer layers, respectively. The Z position of a charged track is measured from the energy-weighted mean of the cluster of hit strips. The resolution for a z-position measurement is about 1 mm. Each cathode strip is instrumented with an ADC and a TDC.

There are 2 inactive regions filled with nitrogen gas between the 3 superlayers. The differential pressure in the 5 gas volumes supports the cathode foils (excluding the innermost and outermost foils, which are held in place by support tubes). The total mass in the active region of the UTC, excluding the inner and outer support tubes and innermost and outermost foils, amounts to 2×10^{-3} radiation lengths.

The momentum resolution ($\Delta P/P$) for the two body decays $K_{\pi2}$ and $K_{\mu2}$ are 1.1% and 1.3%, respectively. More information on the UTC is given in [23].

3.4.4 Range Stack (RS)

The primary functions of the Range Stack (RS) are energy and range measurements of charged particles and their identification. The RS is located just outside the UTC at an inner radius of 45.08 cm and an outer radius of 84.67 cm. It consists of 19 layers of plastic scintillators, azimuthally segmented into

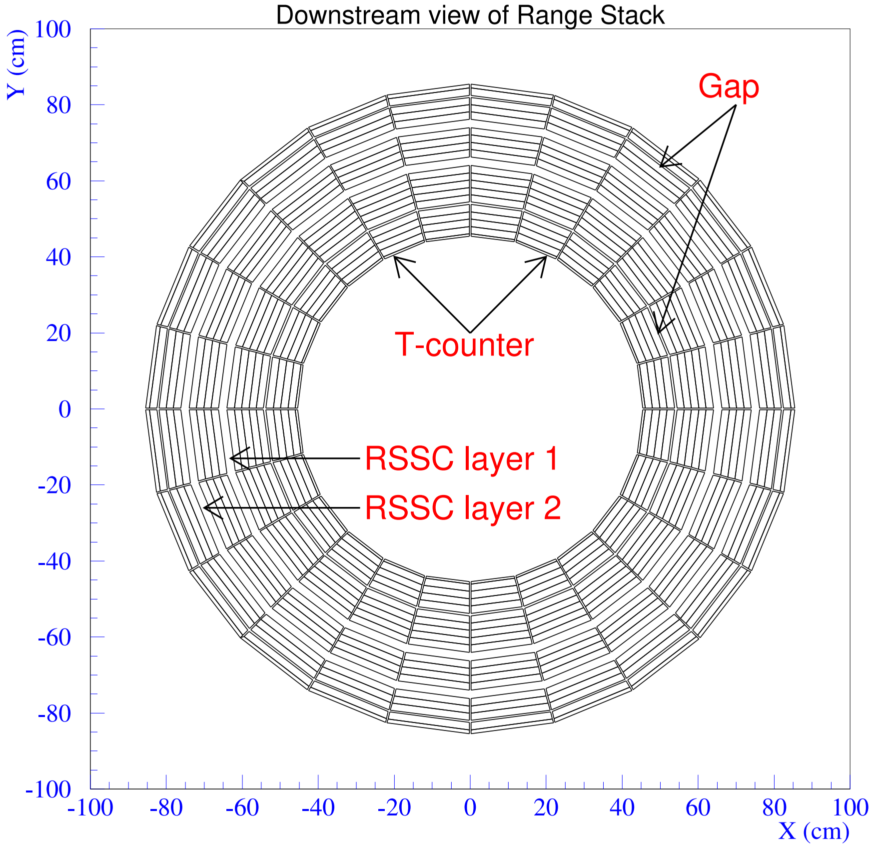

Figure 3.11: End view of the Range Stack. The two layers of the Range Stack Straw Chambers are located after layers 10 and 14.

24 sectors (see Fig. 3.11). Conventionally, the 24 sectors are grouped into 6 "hextants" of 4 sectors each (sectors 1-4, 5-8, 9-12, 13-16, 17-20, 21-24).

The scintillators of layers 2-18 have a thickness of 1.905 cm and a length of 182 cm. The scintillators of layer 19 have a thickness of 1 cm. This layer is mainly used to veto charged particles with long range by requiring that they do not reach the layer-19 scintillators. The scintillation light in the layer 2-19 counters is led by light guides to PMTs at both the upstream and downstream ends.

The innermost counters, called T-Counters, have a thickness of 6.35 mm and a length of 52 cm. 17 WLS fibers are embedded in each scintillator for read out, and are grouped and fed to a single PMT at each end. The T-Counter signals are used to produce a trigger signal and to define the fiducial region as 2π sr solid angle, which is almost the same as the solid-angle acceptance of the UTC.

Each PMT of the RS scintillators is read out by an ADC and a TDC. Signals from 4 PMTs at the same end, same hextant and same layer are multiplexed and read out by a single TD. The signals are demultiplexed in the offline event reconstruction by using TDC information in order to determine which counter the signal came from. The ADCs record charges in a 100 ns window, and the TDCs record the time of hits in the range of 10 μs. The TDs record pulse heights of PMT signals in 2 ns intervals (500 MHz sampling) for up to 2 μs to provide information on the time development of the pulses. This 500 MHz sampling provides detailed information about the pulse shapes, which enables the separation of two pulses as close as 5 ns in time, by performing an offline pulse fitting. The gate width of the TDs is narrower than that of the TDCs in order to reduce the data size.

The time of a hit in the RS counters is obtained from the average of the upstream and downstream TDC times, and the z position of the hit is obtained from their time difference. In the case that TDC hit information is missing, the hit time information is complemented with the corresponding TD information if available.

The π^+'s from the $\pi\nu\overline{\nu}$ decay in the PNN2 region, whose momentum is up to 199 MeV/c, come to rest in the RS. Pions with 199 MeV/c can propagate into plastic scintillator by roughly 28 cm. The total radial thickness of the RS and target is 45 cm, therefore almost all of the π^+'s (which are also bent in the 1 Tesla magnetic field) lose their entire kinetic energy and come to rest by the 10^{th} layer of the Range Stack. On the other hand, the momentum of μ^+'s from kaon decays at rest are at most 236 MeV/c. Muons with 236 MeV/c (such as μ^+'s from $K_{\mu 2}$ decays) can propagate into plastic scintillator by 54.3 cm. Hence, $K_{\mu 2}$ decays are completely suppressed by requiring that charged tracks come to rest by the 12^{th} layer of the RS.

However, the μ^+'s from $K_{\mu 2\gamma}$ and $K_{\mu 3}$ decays could come to rest earlier in the RS. Besides, a π^+ can decay in flight and the secondary μ^+ may come to rest in the RS. For this reason, further identification of π^+ in the RS is performed by observing the $\pi^+ \to \mu^+ \to e^+$ decay sequence in the TDs and TDCs of the counter where the π^+ comes to rest (the "stopping counter"). Typical TD pulses in and around the stopping counter for a pion track are shown in Fig. 3.12.

The μ^+ from the $\pi^+ \to \mu^+$ decay at rest has a kinetic energy of 4 MeV (equivalent range in plastic scintillator is 1 mm) and rarely goes out of the stopping counter. On the contrary, the e^+ from the $\mu^+ \to e^+$ decay at rest has a kinetic energy of up to 52 MeV, and the e^+ track loses kinetic energy not only in the stopping counter, but also in the neighboring counters. The $\pi^+ \to \mu^+$ decay at rest, whose lifetime is 26 ns, is detected by using TD information of the stopping counter by performing a double-pulse fitting, while the sequential $\mu^+ \to e^+$ decay, whose lifetime is 2.2 μs, is detected by using TDC information of the stopping counter as well as the neighboring counters by requiring that

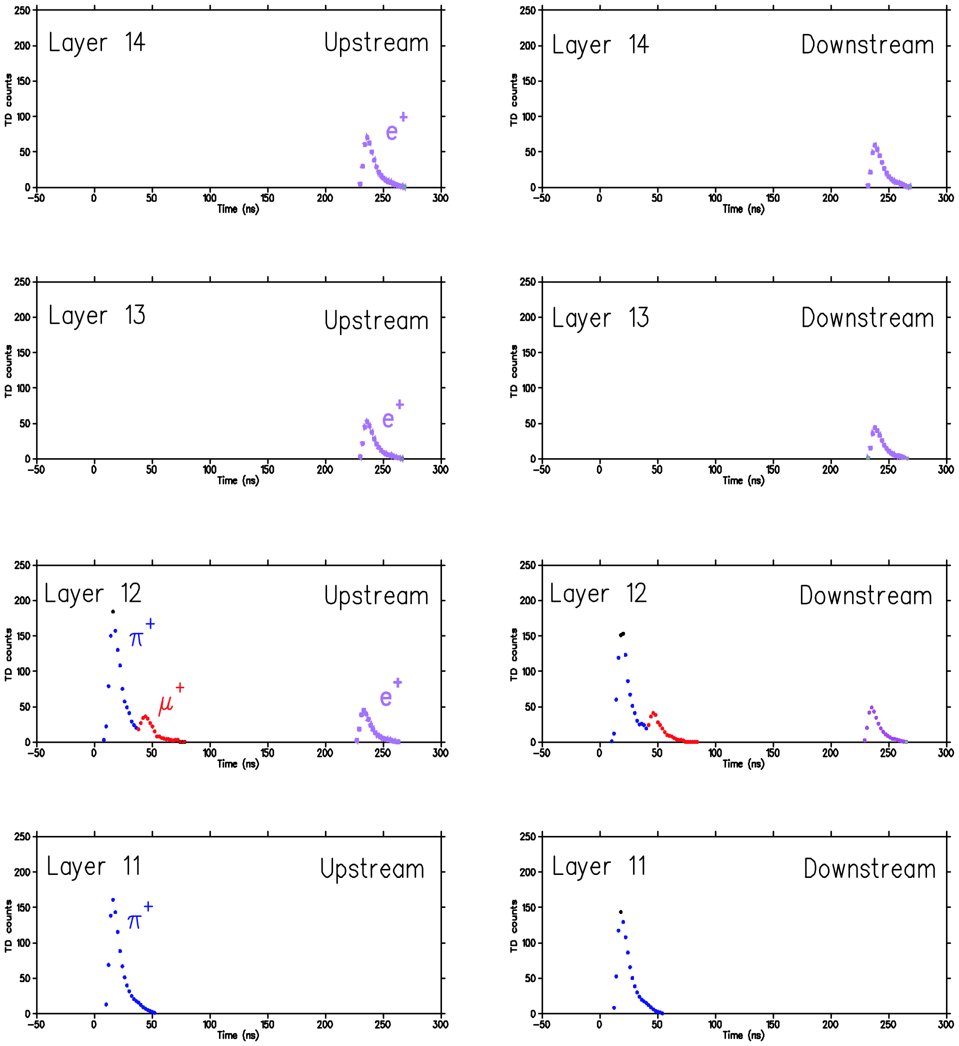

Figure 3.12: Pulses in and around the stopping counter recorded by the TDs of the upstream and downstream ends. The $\pi^+ \to \mu^+ \to e^+$ decay sequence is recorded in the stopping counter (Layer 12 in this case). The μ^+ from the $\pi^+ \to \mu^+$ decay is contained in the stopping counter. The positron from the $\mu^+ \to e^+$ decay should also be found in the counters around the stopping counter (Layers 13 and 14 in this case).

the times of the hits from the e^+ track are consistent with each other.

Range Stack Straw Chambers (RSSCs) are located after layers 10 and 14 of the RS. The inner RSSC consists of two layers of 24 straws per sector, and the outer RSSC consists of two layers of 28 straws per sector. The RSSCs are used to determine the trajectory (and therefore refine the range) of a charged particle in the RS. Information on the RSSCs is given in [24].

Energy, range and momentum measurements of charged tracks are crucial to distinguish the π^+'s in the signal region from backgrounds due to $K_{\pi 2}$ decays, which have monochromatic momenta of 205 MeV/c. Energy, range and momentum resolutions of 2.8%, 2.9% and 1.1% respectively are achieved for fully contained $K_{\pi 2}$ decays by the UTC-RS system.

3.4.5 Photon Veto

The detection of any activity coincident with the charged track is crucial for suppressing the backgrounds for $K^+ \to \pi^+ \nu \overline{\nu}$. Photons from $K_{\pi 2}$ and other radiative decays are detected by hermetic photon detectors, which are shown in Fig. 3.13.

The photon detectors, surrounding the K^+ decay vertex in a 4π solid angle, are located in the barrel, upstream and downstream end caps, and near the beam line. Photon veto is performed by the Barrel Veto (BV), the Barrel Veto Liner (BVL), the upstream and downstream End Caps (ECs), the upstream and downstream Collar detectors (CO), the downstream Microcollar detector (CM), the Downstream Photon Veto detector (DSPV), as well as the AD, target and RS.

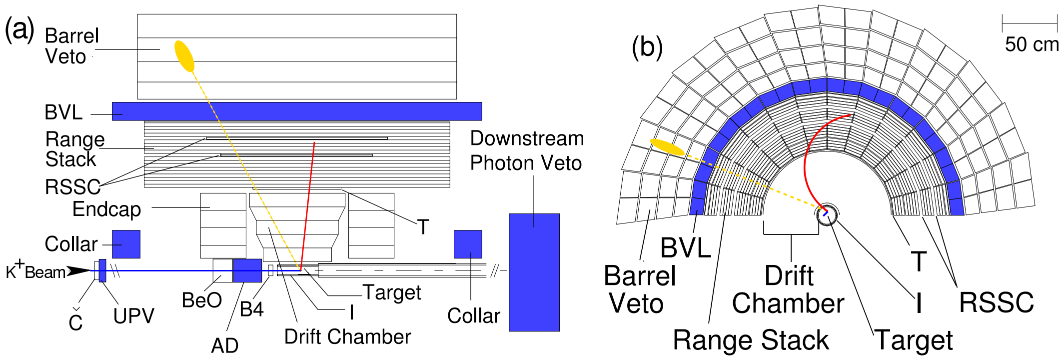

Figure 3.13: Schematic side (left) and end (right) views of the upper half of the E949 detector. Newly installed or upgraded photon detectors for E949 are in blue.

The BV, 1.9-m long, is located in the outermost barrel region with an inner radius of 94.5 cm and an outer radius of 145.3 cm. It surrounds two thirds of the 4π sr solid angle. The BV consists of 48 azimuthal sectors and four radial segments. The radial modules consist of 16, 18, 20 and 21 layers of 1-mm thick lead and 5-mm thick plastic scintillator from inner to outer module respectively. The azimuthal boundaries of each sector are tilted so that photons from the decay vertex could not travel along the inactive inter-sector gaps without losing their energy in the active regions.

The BV has 14.3 radiation lengths in total. Each end of each module is read out by a PMT and the signals are recorded by an ADC and a TDC. The time resolution of individual BV counters is found to be 1.0 ns. The resolution is limited by the sampling time of the TDCs. The fraction of the photon energy left in scintillators is about 30%.

The BVL, which is newly installed for E949, is located just outside the

Range Stack and inside the Barrel Veto. It has an inner radius of 85.2 cm and an outer radius of 93.5 cm, and consists of 48 azimuthal sectors and 12 radial layers of 1 mm thick lead and 5 mm thick plastic scintillator.

The BVL has 2.3 radiation lengths in total. Its length (2.2 m) is larger than that of the BV, so that the BVL adds active material to the region where the radiation length is relatively small. Each end of each module is read out by a PMT and the signals are recorded by an ADC and a TDC. Groups of adjacent sectors in each end are read by TDs. The time resolution of the individual BVL counters is found to be 0.5 ns. The resolution of the BVL modules is also limited by the TDC sampling time. The fraction of the photon energy seen by scintillator is about 30%.

The EC photon detector [25] is located in the 1 Tesla magnetic field and covers roughly one-third of the 4π sr photon coverage. The EC is exposed in a high counting-rate environment near the beam line, where beam particles cause many hits that are not coincident with kaon decays. These hits may mask photons from $K_{\pi 2}$ decays in the case that an accidental hit arises earlier than the photon hit, or cause vetoing on accidentals and loss of acceptance. Therefore offline double-pulse finding in the signals recorded by the CCDs, and tuning the photon veto time windows around these second pulses seperately, is crucial.

The upstream EC detector consists of 75 undoped Cesium Iodide (CsI) crystals, segmented in four rings (13, 14, 21 and 27 crystals from the inner to outer ring respectively), and the downstream EC detector consists of 68 crystals in four rings (11, 13, 19 and 25 from the inner to outer ring respectively). A total of 143 crystals with a pentagonal cross-section are used (Fig. 3.14).

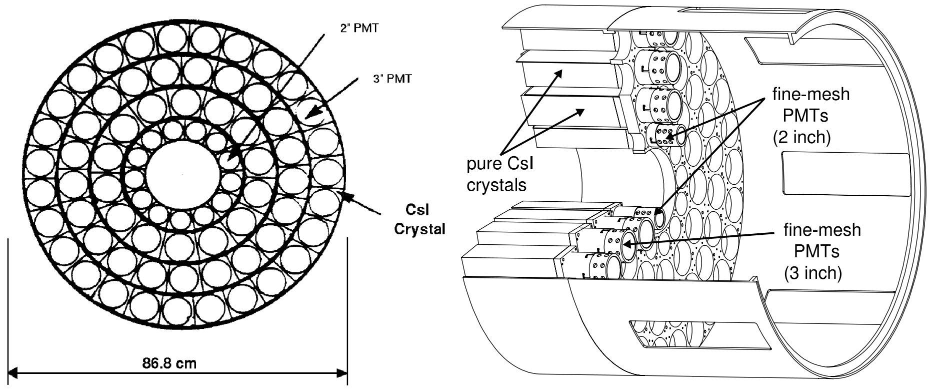

Figure 3.14: End view (left) and back view (right) of the End Cap.

Each crystal has a length of 25 cm (13.5 radiation lengths) and the whole EC detector is designed to minimize photon escape through its radial cracks. Fine-mesh PMTs [26], which maintain high gains in strong magnetic fields, are attached directly to the crystals to achieve efficient light collection (Fig. 3.14).

Only the fast component of the CsI light output with a decay time of a few tens of a nanosecond at a wavelength of 305 mm is selected by ultraviolet transmitting optical filters. The PMT signals are read out by ADCs, TDCs, and CCDs.

The upstream and downstream CO detectors are located outside the ECs and around the beamline, so that they cover the region with small angles around the beam line. They are similar in construction and cross-sectional size, but the upstream CO is about half the thickness of the downstream one. Their xy crossection is a $\sim$50 cm by $\sim$50 cm dodecagon with a 203.2 mm (164.3 mm for the downstream CO) hole in the middle, and they are segmented in 12 azimuthal sectors. The downstream CO consists of 25 layers of 5 mm thick scintillator alternating with 2 mm thick lead, with a total thickness of about

173.5 mm and radiation length of about 9. The light from each sector is read out by bundles of WLS fibers glued in grooves in the scintillator, then fed to a PMT outside the magnetic field through a lucite lightguide. The upstream CO is read out directly with the lightguide, and has no fibers. The signal is recorded by TDCs and ADCs.

The CM is a mysterious device that has left no traces of documentation through its life with the E949 experiment.

Finally the DSPV (see Fig. 3.15), in the far downstream end of the detector after the TG PMTs, is a 700 mm by 700 mm square right on the beam path. It consists of 26 sheets of 10 mm thick scintillator alternating with 1.5 mm thick lead, with a total thickness of about 300 mm and 7.3 radiation lengths. It is not optically segmented into modules, and is read out directly by 4 PMTs simultaneously, two on each side. The signal is sent to TDCs and ADCs.

3.5 Trigger

The trigger selects signal-like events out of all kaon decays to be recorded, based on TDC, ADC, CCD and TD information from the detector elements. Digitized information of the selected events, which correspond to 70-80 Kbyte of data per event, is transfered from the electronics hut to the main computer for data taking.

The trigger is composed of a fast level-0 trigger and level-1.1 and -1.2 triggers. The level-0 trigger makes decisions entirely with logic pulses from detectors. It has a rejection of 10^3 and introduces 38 ns of dead time for every coincident hit in the first two layers of the Range Stack (T•2). The level-1.1

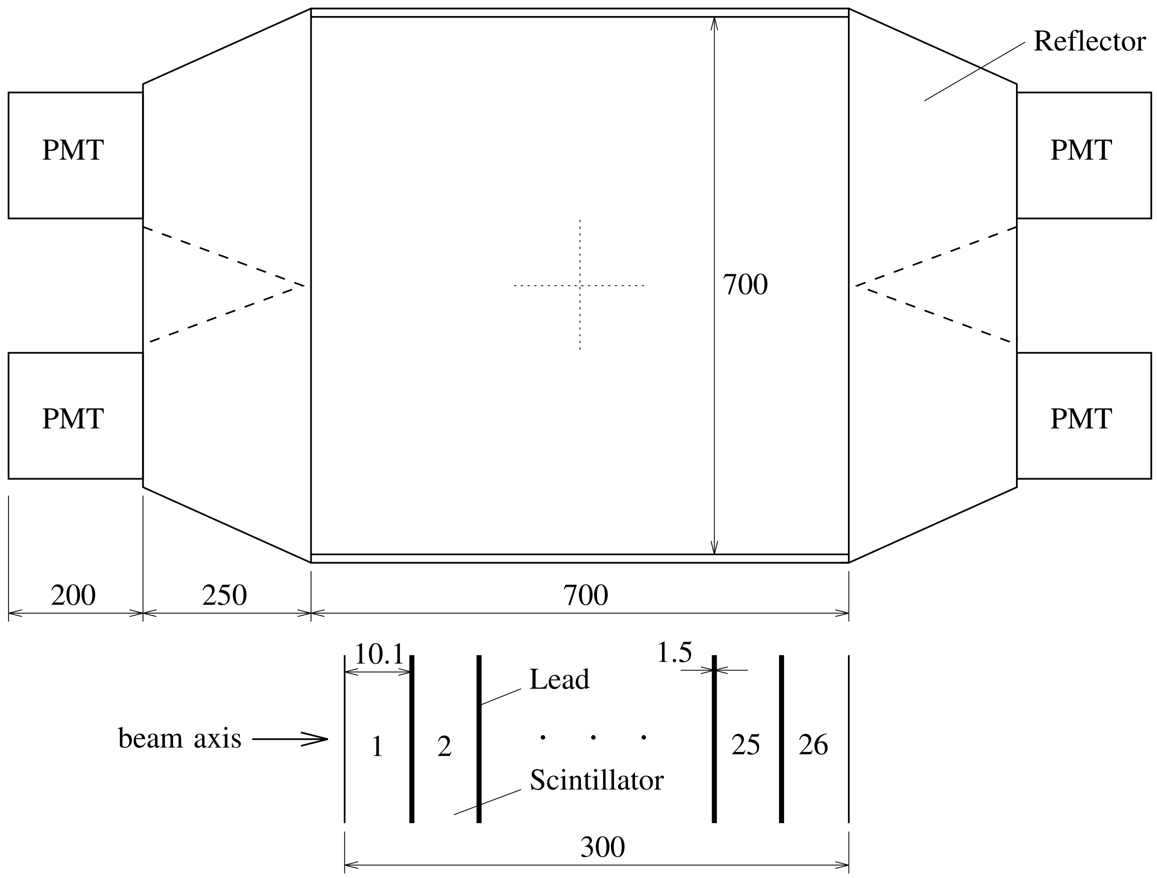

Figure 3.15: Schematic of the Downstream Photon Veto. Dimensions are in mm.

and -1.2 triggers involve partial processing of ADC and TD data, and operate on the lower rate events that pass the level-0 trigger. The level-1.1 trigger has a rejection of 12 after level-0, and introduces 10 to 20 μs of dead time per level-0 trigger. The level-1.2 trigger has a rejection of 2 after level-1.1 and introduces a dead time of up to 100 μs per level-1.1 trigger. The entire trigger for $\pi\nu\overline{\nu}$ therefore has a rejection of 24000, and reduces the 2.6×10^6 kaon decays to about 100 events per spill.

The trigger for $K^+ \to \pi^+\nu\overline{\nu}$ (referred to as $\pi\nu\bar{\nu}(2)$ trigger) consists of the following requirements:

$$\begin{aligned} \pi\nu\bar{\nu}(2) \quad \equiv \quad & \mathrm{KB} \cdot \mathrm{DC} \cdot \mathrm{IC} \cdot \mathrm{T} \bullet 2 \cdot 3_{ct} \cdot 4_{ct} \cdot 5_{ct} \cdot 6_{ct} \cdot \overline{(13_{ct} + \cdots + 18_{ct})} \cdot \overline{19} \cdot \\ & \overline{\mathrm{BV} + \mathrm{BVL} + \mathrm{EC}} \cdot \mathrm{L0\_rr2(1)} \cdot \mathrm{HEX} \cdot \mathrm{L1.n} \cdot (\mathrm{ps16} + \overline{C_\pi}) \end{aligned} \tag{3.1}$$

where

- K^+ Stop Requirements:
  - KB : KB requires a coincident hit in the Kaon Čerenkov Counter, the B4 Hodoscope, and the target. This requirement ensures that a kaon enters the target.
  - DC : Online delayed coincidence, in which the IC time is required to be at least 2 ns later than the time in the Kaon Čerenkov Counter. This delayed coincidence requirement ensures that a kaon decays at rest.
- Fiducial Requirements on Charged Tracks:

- IC : At least one hit in the I-Counter is required to be coincident with the T•2 time. This condition requires that a charged track from a kaon decay enters the fiducial region of the detector.
- T•2 : A coincidence hit is required in the first two layers (T-Counter and layer 2) of the Range Stack in the same sector. This condition requires that a charged track from a kaon decay enters the Range Stack.

- Range Requirements on Charged Tracks:
  - $3_{ct} \cdot 4_{ct} \cdot 5_{ct} \cdot 6_{ct}$: A charged track must reach the Range Stack layer 6 and have hits in all previous layers. The T•2 sector and two sectors clockwise from it are defined as the charged track (ct) sectors. This condition removes short-range tracks from 3- and 4-body decays.
  - $\overline{(13_{ct} + \cdots + 18_{ct})} \cdot \overline{19}$: A charged track is not allowed to reach Range Stack layers 13-19. This condition removes μ^+ and other long tracks, allowing to collect more events in the region of interest (PNN2).
  - L0_rr2(1) : Refined range requirement on a charged track. μ^+'s from $K_{\mu 2}$ decays are suppressed by the $\overline{(19_{ct})}$ requirement. However, some of the μ^+'s can still survive the requirement if their polar angle (compared to beam direction) is small and they stop near the edge of the RS scintillators. Events are rejected if the range calculated in the online trigger is too long. The online range in the target is obtained from the number of hit fibers, and the online range in the Range Stack is obtained from the polar angle and the stopping layer

of the charged track. The polar angle is measured by the z positions at RS layers 11, 12 and 13, which are obtained from the end-to-end time difference of both-end hits. The online stopping counter is found by the "stopping counter finder" (SCF), which defines the outermost and most clockwise *ct* counter as the stopping counter.

- Online Photon Veto:
  - $\overline{\mathrm{BV}+\mathrm{BVL}+\mathrm{EC}}$: Online photon veto in the BV, BVL and EC. Any photon hit which is coincident with T•2 and whose energy is above a threshold is not allowed. Each PMT signal from each end of the BV and BVL counters is discriminated by the threshold corresponding to 5 MeV, and the mean time of the discriminated signals from both ends is given by digital mean-timers [19]. Events are rejected if the output signals of the mean timers are coincident with T•2. Each PMT signal from each End Cap crystal is discriminated by the threshold corresponding to 20 MeV. Events are rejected if the output signals are coincident with T•2.
  - HEX : Only one RS hextant is allowed to have hits coincident with T•2, or two hextants if they are adjacent. This rejects events with multiple tracks and events with photon activity in the RS.
- Level-1.1 and 1.2:
  - L1.1 : Level-1.1 trigger requires a signature of $\pi^+ \to \mu^+$ decay in the online stopping counter. The height (PH) and the area (PA) of the pulse(s) recorded by the TDs in the stopping counter are compared.

The decision is made by a control board with Application Specific Integrated Circuits (ASICs) in each TD board. The ratio PH/PA would be smaller for double pulses than for a single pulse. Events are rejected if the PH/PA ratio is large.

  - L1.2 : Level-1.2 trigger consists of three parts: (1) Events are rejected if coincident hits are detected in a RS counter near the stopping counter. It rejects events with muons that pass Level-1.1 due to accidental hits from the outside providing the double-pulse $\pi^+ \to \mu^+$ decay signature in the stopping counter. (2) Events are rejected if one of two adjacent hextant hits is not due to a charged track. This requirement removes those events that pass the HEX requirement because of accidental hits. (3) Events are rejected if the SCF assignments are bogus (e.g., stopping layer is more than 19, etc).

- Pion Čerenkov veto

  - (ps16+$\overline{C_\pi}$) : An online pion Čerenkov veto was imposed after run 49151, when the rate of beam pions was found to be too high. This requirement was prescaled by 16 (i.e. it was not applied in one every 16 events), in order to be able to measure its rejection. The data taken before the addition amount to about 39.4% of the total.

In addition to the $\pi\nu\overline{\nu}$ trigger, various "monitor" triggers also collected events for use in data quality assessments, calibration of detector subsystems, and acceptance and background calculations.

- $K_{\pi 2}(1)$= $\mathrm{KB} \cdot \mathrm{T} \bullet 2 \cdot (6_{ct} + 7_{ct}) \cdot \overline{(19_{ct})}$

- $K_{\pi 2}(2)$= $\mathrm{KB} \cdot \mathrm{DC} \cdot \mathrm{T} \bullet 2 \cdot \mathrm{IC} \cdot (6_{ct} + 7_{ct}) \cdot \overline{(19_{ct})} \cdot \mathrm{HEX} \cdot \mathrm{L1.n}$

- $K_{\mu 2}(1)$= $\mathrm{KB} \cdot \mathrm{T} \bullet 2 \cdot (6_{ct} + 7_{ct}) \cdot (17_{ct} + 18_{ct} + 19_{ct})$

- $\pi_{scatter} = \pi B \cdot \overline{\mathrm{DC}} \cdot \mathrm{T} \bullet 2 \cdot \mathrm{IC} \cdot (6_{ct} + 7_{ct}) \cdot \overline{\mathrm{BV} + \mathrm{BVL} + \mathrm{EC}} \cdot \mathrm{HEX}$,

where πB requires that a pion enters the target. Because each monitor trigger is highly prescaled, the number of all the monitor triggers in each spill were at most 10.

3.6 Monte Carlo Simulation

The detector and the physics processes in it are modeled by a Monte Carlo (MC) simulation program. The MC includes all of the detector elements, except for the beam instrumentation upstream of the target, therefore the simulation of kaon decays in the E949 detector starts from a "beam file" with the (x,y,z) positions of kaon decays in the target obtained from an analysis of $K^+ \to \mu^+\nu$ decays. The MC generates all data, except for the TD and CCD pulse-shape information.

Multiple Coulomb scattering of charged particles with various nuclei in the detector are calculated according to the theory of Moliere [27], with corrections for the spin of the scattered particle and the form factor of the nucleus [28]. Hadronic interactions of positively charged pions in the plastic scintillators are calculated using a combination of data and phenomenological models [29]. Photon and electron interactions are calculated using the EGS4 electromagnetic-shower simulation package [30].

The accuracy and the performance of the MC has been verified by comparing the different kinematic variables from data and MC for $K^+ \to \pi^+\pi^o$ and $K^+ \to \mu^+\nu$ decays.

3.7 Summary of 2002 Data Taking

The E949 experiment had the first physics run for 12 weeks from March to June in 2002. The data collected in the run period corresponded to 1.77×10^{12} kaon decays in the target. Fig. 3.16 shows the number of accumulated kaon decays as a function of the data-taking days for the various running years of E787 and E949.

The E949 run was performed under a high beam intensity environment. The proton intensity of the AGS increased to twice as high as in E787. The total exposure of kaons available for E949 was 30% that of E787, which recorded 5.94×10^{12} kaon decays in the target.

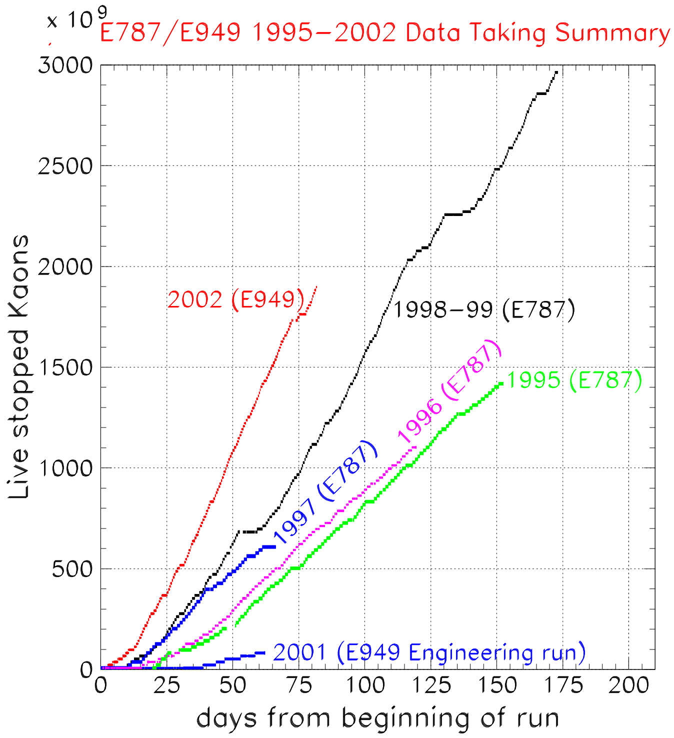

Figure 3.16: Number of kaon decays in the target as a function of the data-taking days for E787 and E949.

Chapter 4

Analysis overview

4.1 Introduction

Reliable detection of a process as rare as $K^+ \to \pi^+\nu\overline{\nu}$ requires knowledge and suppresion of the background processes of the order of $10^{-12}-10^{-13}$, depending on the achieved acceptance. For this purpose, a set of stringent selection criteria ("cuts", see A) is used in a blind analysis, in order to estimate the expected background levels from data. Monte Carlo simulation is also used for the backgrounds that cannot be reliably identified in the data samples. In this chapter, the analysis technique and the methods used to verify its reliability will be described.

4.2 Background overview

The range in plastic scintillator versus momentum distribution of the outgoing charged particle (pion or muon) is shown in fig... for the events which passed the PNN(1) or PNN(2) trigger. The two concentrated peaks are due to the dominant two-body decays $K^+ \to \pi^+\pi^o$ ($K_{\pi 2}$ peak) and $K^+ \to \mu^+\nu$ ($K_{\mu 2}$ peak). The range tails contain peak events with inelastic pion/muon scattering in the RS. Therefore the momentum measurement is correct, but the range is mismeasured and these events do not belong to the peak. The diagonal "bands" are either multi-body decays with pions/muons ($K_{\pi 2\gamma}$, $K_{\mu 3}$, $K_{\mu 2\gamma}$, K_{e4}), decays in flight, or, in the case of pions, $K_{\pi 2}$'s where the pion scattered inelastically in the target. In this case, both the range and the momentum are measured incorrectly. Beam pions that scatter into the detector acceptance also belong to this band.

As can be seen in this plot, the $K_{\mu 2}$ peak and tail do not contribute at all to the PNN2 background, and the three-body muon decays in the band give a small contribution. For these modes to be confused with signal, both the muon has to be misidentified as a pion, and the extra photons have to escape the veto.

The multi-body pion decays and scattered beam particles are the processes whose kinematics coincide with those of $K^+ \to \pi^+\nu\overline{\nu}$ in the PNN2 region. $K_{\pi 2\gamma}$ has 3 photons to veto on, and K_{e4} has the signature of extra activity in the target, either in the Kaon fibers (detected as second pulses) or outside of them.

Scattered beam backgrounds are divided in 2 categories: *single-beam background* (see Fig. 4.1) is due to a beam pion entering the target and scattering into the detector or a beam Kaon decaying in flight causing its products to be in the PNN2 kinematic region due to a Lorenz boost. Although the case of a Kaon decay-in-flight is suppressed by all the other K decay cuts as well, a beam

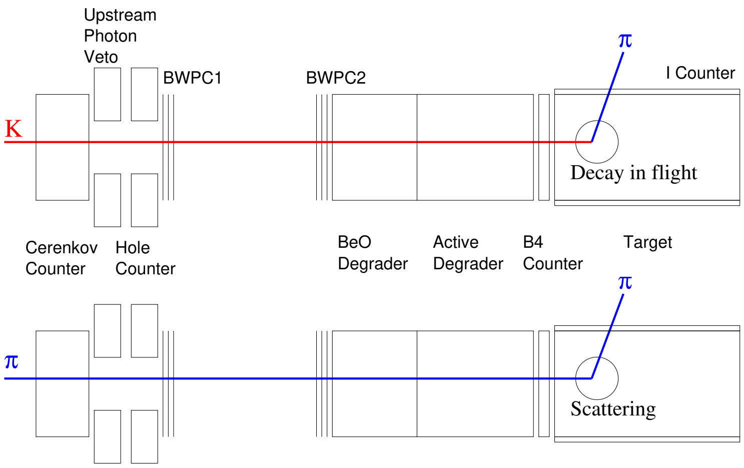

Figure 4.1: Schematic diagrams of the Single Beam background: a Single Kaon Beam background (top) and a Single Pion Beam background (bottom).

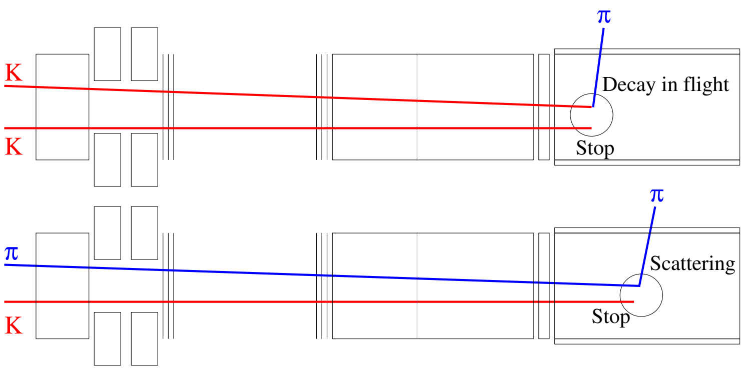

Figure 4.2: Schematic diagrams of the Double Beam background: a $K-K$ Double Beam background (top) and a $K-\pi$ Double Beam background (bottom).

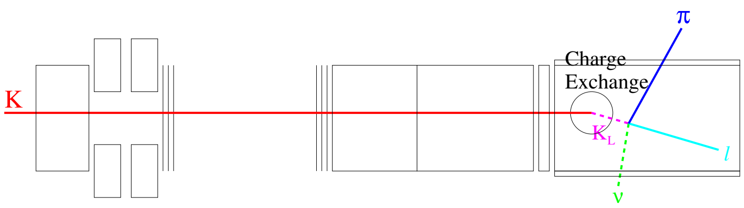

Figure 4.3: Schematic diagram of the charge exchange interaction background.

pion scattering into the detector has no extra particles to veto on, just like the signal. Howerver, both processes occur instantaneously after the entrance of the beam particle into the target, unlike normal decays where the Kaon has to stop first and decay a while later, therefore they do not satisfy the delayed coincidence requirement. The *double-beam background* (see Fig. 4.2) is caused by two beam particles entering the detector at times sufficiently different to fool the delayed coincidence. The products of the first Kaon can be missed under certain circumstances, and a second pion can scatter into the detector like in the single-beam-pion case ("K-pi" background) or a second Kaon can enter the target and decay in flight, like in the single-beam-kaon case ("K-K" background). Double-beam backgrounds are suppressed by requiring no activity in the beam detectors in time with the decay.

Beam kaons can also interact in matter as they are being brought to rest and produce a neutral kaon via the charge exchange process (see Fig. 4.3). K^o's are not slowed down in the target, so potential background arising from prompt K^o_s's decay is removed by the delayed coincidence requirement. However, K^o_Ls are long-lived and can decay semi-leptonically. If the K^o_L travels slowly in the target, the decay lepton is not detected and the π^+ can emulate the signal.

The main background in the PNN2 region, however, is the $K_{\pi 2}$ with target scatter process, and the main concern in this analysis will be to minimize it. This is a particularly dangerous background due to the large BR of $K_{\pi 2}$ and the way the geometry of the scatter correlates the kinematics of the π^+ and the direction of the photons produced by the π^o. Fig. 4.4 gives an idea of this mechanism: the outgoing π^+ starts at the direction of the incoming K, and its track is hidden under the Kaon fibers. Due to the two-body kinematics, at

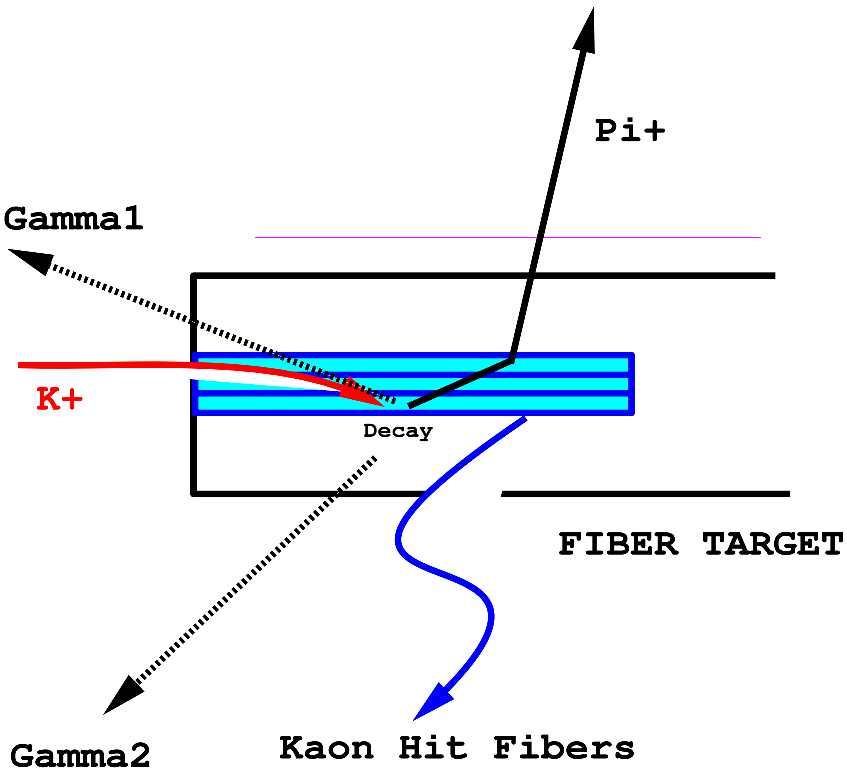

Figure 4.4: A schematic of a $K_{\pi2}$ scattering event in the target in which the pion travels along the fibers, and thereby the neutral pion escapes through the weak photon detection region of the detector.

least one of the two photons has a higher probability to go towards the beam direction, where the photon detection power of the detector is smaller than that at the barrel region. Then the π^+ scatters inelastically in a kaon fiber and enters the detector with deteriorated kinematic quantities as compared to the $K_{\pi2}$ peak. Such events are wrongly included in the PNN2 box, and their photon veto rejection is not the same as the ones on the peak.

4.3 Analysis technique

4.3.1 Background estimation from data: bifurcated analysis

The large suppression of backgrounds needed for a reliable measurement makes estimation of the background in the signal region difficult, because any measurement involving low statistics is subject to large statistical fluctuations. Furthermore, the development of cuts using smaller and smaller numbers of events can result in bias, because it is always possible to design cuts to remove a single event or a small number of events, but which may not represent the characteristics of a larger data sample.

To avoid this bias in designing cuts, a "blind" analysis is performed. The background sources and the cuts to suppress each one of them are identified a priori and the signal region is pre-defined (a multi-dimensional parameter space, populated by the events that pass all the cuts, often referred to as the "box") where the signal to background ratio is expected to be the highest. Cuts to suppress background are developed using events which lie outside the box and events in the box are not counted or examined until the cuts and the background estimates are final.

To enhance the statistical power of the analysis, background measurements are made via "bifurcated" analysis. Each background is addressed by at least two uncorrelated cuts or group of cuts, which can be independently "inverted" to create high statistics tagged background samples from data. That is, background data samples can be created by selecting events which fail a specific cut.

A pictorial representation of a bifurcated analysis is shown in Fig. 4.5. If cut1 and cut2 are designed to target a specic type of background and are assumed to be uncorrelated, then the number of background events in signal region A relative to that in region B in the parameter space of cut1 and cut2 must be equal to the background events in region C relative to region D. Applying cut2 to the inverted cut1 sample, one can get the number of events in region B, which will be referred to as *normalization*. Then measuring the *rejection* of cut1 on a sample which fail cut2 via $R = (C + D)/C$, the background level in signal region A can be calculated as:

$$N_{bg} = BC/D = B/(R - 1) \tag{4.1}$$

Thus, in a bifurcated analysis, the measurement of background in the signal region is restricted to the measurement of the number of events outside the signal region.

Whenever possible, the background sample is extracted from the real data as opposed to modeling the background with Monte Carlo simulations. This is because the reliability of the simulation of various physical processes involved is limited due to uncertainties in nuclear and photo-nuclear total and differential cross-sections. These can lead to large uncertainties when extrapolating to sensitivities of the order of 10^{-10}. Nevertheless, in some cases this method is the only one available because certain cuts suppress many different backgrounds with similar signatures. Therefore, by inverting one of them, it is not possible to clearly tag a certain background and measure the rejection of other cuts on it, and the background will be over- of under-estimated. Moreover, since the level of these backgrounds is very small, the samples needed to measure the normalization or rejection run out of statistics after applying some purification setup cuts. This is the case for the K_{e4}, $K_{\pi 2\gamma}$ and CEX backgrounds, which cannot be easily separated from the much more abundant $K_{\pi 2}$ scatter and double-beam events.

To detect and avoid any bias in the cuts, background measurements are performed twice on independent data samples. The data set is partitioned into one-third and two-third samples uniformly throughout the run, and cuts are designed and the background level is measured using the one-third sample. When the background estimate from the one-third sample is found to be within the acceptable limit, the cuts are frozen and the background level is re-measured using the two-third sample. If the cuts are unbiased, the one-third and the two-third samples should give the same result within statistical uncertainty when scaled appropriately to represent the entire data set. The background, estimated using the two-third sample, is then corrected for the whole data sample and is accepted as the final background measurement for the analysis.

4.3.2 Validity checks: outside-the-box and single-cut-failure studies

The validity of the bifurcation method relies on the assumptions that (a) the bifurcated cuts are uncorrelated and (b) that all the background types are known and the cuts to suppress them are pre-identied. The assumption that the bifurcated cuts are uncorrelated can be tested by loosening the cuts, re-calculating the background levels at these looser cut positions, and comparing it to the observed number of events in these “outside the box” regions. Fig. 4.6 shows a schematic explanation of this method. A new signal region A’ larger than A is defined, and the expected background in it is calculated with the same method described above. Then the background in the unmasked part of this region will be

$$bg' = bg(A') - bg(A) = B'C'/D' - BC/D \tag{4.2}$$

Since the region is close but still outside the box, it can be examined and the events in it counted. If the number of events observed is different than that predicted, a correlation between cuts may be present, which invalidates the bifurcated background estimate for the box.

The events that fail only one or two cuts are also individually examined. These are the closest to the signal box and if more than expected are found (based on the rejection of every cut), or a certain pattern is observed, it may mean that there is a source of background that has not been accounted for in the bifurcation analysis that is suppressed only by the one cut that these events failed. In this case new “safety” cuts have to be developed to attack this background, their rejection and acceptance has to be measured and the background levels re-measured including these new cuts.

4.3.3 Acceptance measurement

4.3.4 Calculating the Branching Ratio

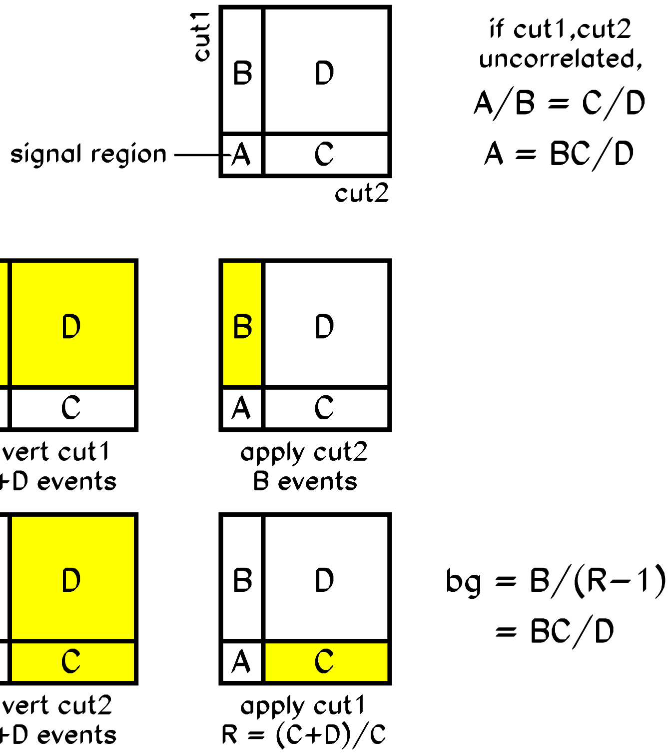

Figure 4.5: A background estimate resulting from a bifurcated analysis. The letters signify both the samples and the number of events in them.
Top: If a certain background is suppressed by cut1 and cut2, then the data sample can be represented in the parameter space of these two cuts as 4 sub-samples A, B, C and D. If these cuts are uncorrelated, then the number of background events in region A relative to that in B is equal to that in C relative to D.
Middle: Count events that fail cut1 and pass cut2 to get the normalization B.
Bottom: Select events that fail cut2, and measure the rejection of cut1 via $R = (C + D)/C$. Region A is never examined in this procedure. The background estimated to be present in region A is given by $BC/D = B/(R - 1)$.

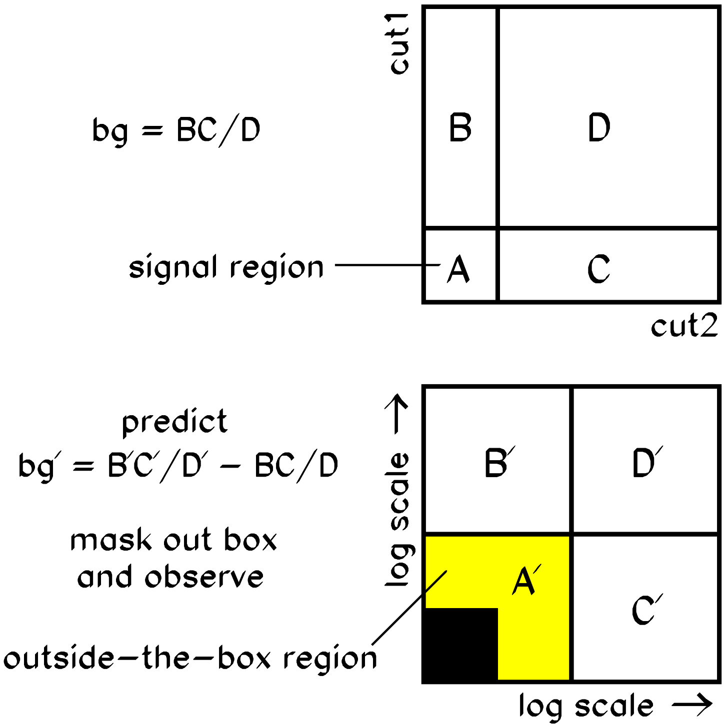

Figure 4.6: Schematic representation of the outside-the-box study.

Chapter 5

Background estimation

5.1 Introduction

5.2 $K^+ \to \pi^+\pi^o$ target scatters

The $K_{\pi 2}$decay, where the π^+ scatters in the Target, is the dominant background for the PNN2 analysis. As it has been shown with Monte Carlo simulations ([32]), the photon distribution from the π^o decay is more uniform in polar angle for events where the π^+ has scattered in the target, than for unscattered ones. Therefore, the Photon Veto rejection for TG scatter events is expected to be different than that for $K_{\pi 2}$events in the peak. The kinematic cut cannot be used anymore in the bifurcation study, since the PV rejection has to be measured inside the PNN2 kinematic box.

The other set of cuts used to supress this background are the TGCUTS. These eliminate events with evidence of a scattered pion in the target, either the scatter occured outside the Kaon fibers (scatters visible in xy, or "xy-scatters") or inside them (events where the π^+ started in the beam direction and then scattered into the detector acceptance, or "z-scatters"). The two categories are not mutually exclusive. By inverting some of these cuts and applying others, samples with varying mixtures of xy- and z-scatters can be created for the rejection branch. 13 such "classes" were used, described in Table 5.1, and the PV rejection was measured on them in the PNN2 kinematic box. The rejection in the $K_{\pi 2}$peak is also given for comparison. The PV rejections measured for different classes are consistent with each other within statistical uncertainties, therefore for the final PV rejection, class 12 was used, because it had adequate statistics and it is expected to be the richest in z-scatters. In the normalization branch (see Table 5.2), all the TGCUTS were applied, and the PV was inverted.

CLASS	TGCUTS	PV rejection
1	All cuts, KP2BOX	1016.4± 233.1
2	$\overline{CCDPUL}$, $\overline{EPIONK}$	1653.6± 389.6
3	$\overline{CCDPUL}$, $\overline{EPIONK}$, all others	1304.0±1303.5
4	CCDPUL, EPIONK, TGZFOOL, EIC, OPSVETO, $\overline{OTHERS}$	1313.0± 757.8
5	$\overline{CCDPUL}$, $\overline{EPIONK}$, $\overline{CHI567}$, $\overline{VERRNG}$	1773.5± 396.4
6	$\overline{CCDPUL}$, $\overline{EPIONK}$, $\overline{CHI567}$, $\overline{VERRNG}$, all others	1744.0±1743.5
7	$\overline{CHI567}$, $\overline{VERRNG}$	2360.0± 572.3
8	$\overline{CHI567}$, $\overline{VERRNG}$, all others	70.0± 69.5
9	$\overline{CCDPUL}$, $\overline{EPIONK}$, $\overline{CHI567}$, $\overline{VERRNG}$, KIC, PIGAP, TARGF, TPICS	1723.2± 417.8
10	$\overline{B4EKZ}$	1760.1± 622.1
11	$\overline{B4EKZ}$, all others	10.0± 9.5
12	$\overline{CCDPUL}$, $\overline{EPIONK}$, $\overline{B4EKZ}$	1754.2± 413.4
13	$\overline{CCDPUL}$, $\overline{EPIONK}$, $\overline{B4EKZ}$, all others	1534.0±1533.5

Table 5.1: Classes of events used to measure the PV rejection in the PNN2 kinematic box, and the rejection found. The PV rejection in the KP2 kinematic peak, after all TGCUTS were applied, is also given. The same setup cuts as in the normalization branch (Table 5.2) are applied.

CUT	Events
	30991832
BAD_RUN,KERROR	30406468
SKIM5,RECON	10483802
PSCUT06	3227433
DELCO3	3208449
KINCUT06	476189
$\overline{PVCUT}$, PNN2BOX	49255
B4EKZ(IC)	35182
TGZFOOL	34676
EPITG	19698
EPIMAXK	19698
TARGF	16999
DTGTTP	16994
RTDIF	16841
DRP	16613
TGKTIM	16330
EIC	15870
TIC	15870
TGEDGE	15517
TGDEDX	12321
TGENR	11782
PIGAP	11569
TGB4	10473
KIC	10469
PHIVTX	8332
OPSVETO	7382
TGLIKE	6980
TIMKF	5644
NPITG	5644
ALLKFIT	5244
TPICS	5238
EPIONK	5019
CHI567	3316
VERRNG	2836
CHI5MAX	1801
ANGLI	1793
CCDBADFIT	1443
CCDPUL	181

Table 5.2: The normalization branch for the $K_{\pi 2}$target scatter background.

Using the numbers from tables 5.2 and 5.1, the $K_{\pi2}$target scatter background is

$$N_{K_{\pi2}-TGscat} = 3 \times \frac{N}{R_{PVclass12} - 1} = 3 \times \frac{181}{(1754.2 \pm 413.4) - 1} = 0.310 \pm 0.219 \quad (5.1)$$

5.3 $K^+ \to \pi^+\pi^o$ RS scatters

Pions from the $K_{\pi2}$decay can also undergo inelastic scattering in the Range Stack and fall into the PNN2 kinematic box by losing energy in the scattering process. However, for these events to be a background for this analysis, the pion momentum also has to be mis-measured and the photons from the π^o decay have to be missed. Therefore, this background is expected to be smaller compared to the $K_{\pi2}$target scattered background. The $K_{\pi2}$RS scatter background can be measured using the $K_{\pi2}$background sample.

It should be noted that these background events are already included in the normalization branch in Table 5.2, but they are not included in the Photon Veto rejection study in Table 5.1 because the target cuts were reversed to measure this Photon Veto rejection. The $K_{\pi2}$events which scattered in the RS should be assigned the same Photon Veto rejection as the KP2BOX events, since the pion did not scatter in the target.

The most effective cuts against this background are the Range Stack track quality cuts RSDEDX and PRRF (collectively referred to as RSCT), the BOX cut on *ptot* and the Photon Veto cut. Table 5.3 summarizes this background

CUT	Rejection PBOX from KP2BOX		Normalization $\overline{RSDEDX}$ or $\overline{CHIRF}$	
	KP2BOX	PNN2 RE BOX	KP2BOX	PNN2BOX
SETUP	39707	490	9847	1954
LAYER14	39640	490	9819	1954
FIDUCIAL	36366	432	8664	1877
UTCQUAL	32907	363	7438	1455
RNGMOM	32480	363	7267	72
RSDEDX	29050	81	NA	NA
PRRF	25213	59	NA	NA
PVCUT	21	0	4	0

Table 5.3: Background study for $K_{\pi 2}$RS scatters.

study. The SETUP cuts are the same with the $K_{\pi 2}$target scatter normalization branch. The second and the third columns of the table contain events in the $K_{\pi 2}$momentum peak. Events with the correct momentum as the $K_{\pi 2}$peak events, but lowered in range and energy are assumed to have scattered in the Range Stack.

The efficiency ϵ_{RSCT} and the rejection R_{RRSCT} of these cuts can be measured as

$$\begin{aligned} \epsilon_{RSCT} &= 25213/32480 &= 0.776 \pm 0.002 \\ R_{RSCT} &= 363/59 &= 6.153 \pm 0.733 \end{aligned} \tag{5.2}$$

The fourth and fifth column of Table 5.3 are for normalization. The RSCT cut is reversed and all other cuts are applied. The various contributions to the total 72 events left in the PNN2BOX before the application of the PV have to be considered in order to calculate the background of interest. The largest component of this sample comes from scattering in the target that contaminated the RSCT reversed sample because of the inefficiency of the RSCT cuts. On the other hand, the total 181 events in the $K_{\pi2}$target scatter normalization branch (Table 5.2) have a target scattered (N_{tg}) and a RS scattered (N_{rs}) component. Therefore

$$\begin{aligned} N_{tg} + N_{rs} &= 181 \\ (1 - \epsilon_{RSCT}) \times N_{tg} + (R_{RSCT} - 1) \times N_{rs} &= 72 \end{aligned} \tag{5.3}$$

Solving this system of equations, the real $K_{\pi2}$RS scatter normalization is obtained, $N_{rs} = 6.382 \pm 0.952$. The final background from the RS scattered events can be measured by applying the $K_{\pi2}$peak Photon Veto rejection to N_{rs} from the second column of Table 5.3, $R_{PV-K_{\pi2}peak} = 25213/21 = 1200.6 \pm 458.2$:

$$N_{K_{\pi2}-RSscat} = 3 \times \frac{N_{rs}}{R_{PV-K_{\pi2}peak} - 1} = 3 \times \frac{6.382 \pm 0.952}{(1200.6 \pm 458.2) - 1} = 0.016 \pm 0.006 \tag{5.4}$$

5.4 Beam background

5.4.1 Single beam

The two cuts that suppress this background are DELCO3 and B4DEDX. In the rejection branch, after some basic setup cuts, B4DEDX is inverted, requiring B4 energy consistent with a pion ($b4abm\_atc < 1.0MeV$), and the DELCO3 cut rejection is measured on this sample. The branch is divided into 3 sub-branches before DELCO3 is applied, of varying purity. Ideally, the rejection

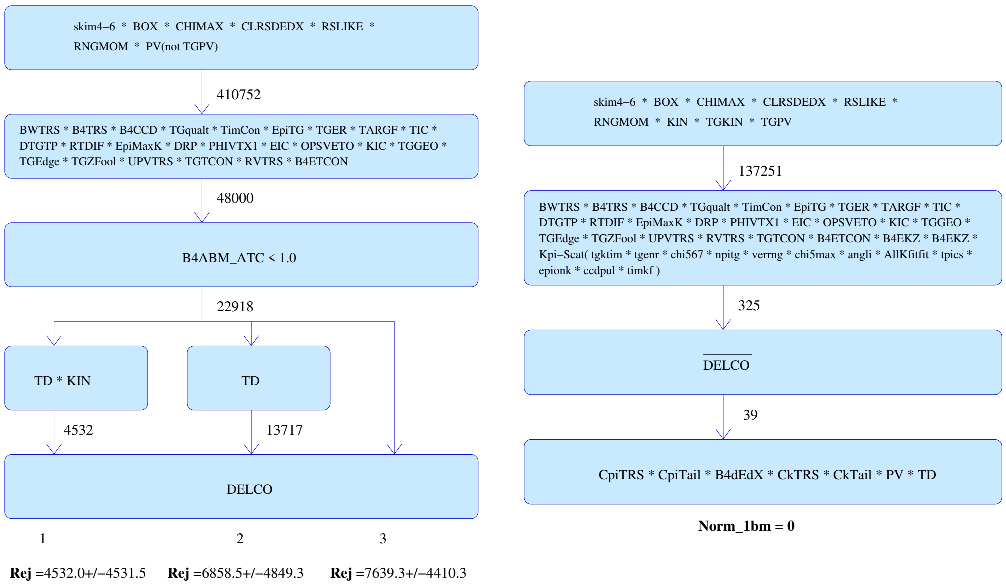

(a) Rejection (b) Normalization

Figure 5.1: Single beam bifurcations: (a) rejection branch, with the values of the DELCO3 rejection obtained for the 3 sub-branches, and (b) normalization branch. Numbers under the boxes are the number of events remaining after the cuts were applied.

from the TD*KIN sub-branch should be used, if statistics permit. It is assumed that the DELCO3 rejection is the same for beam pions and kaons. In the normalization branch, DELCO3 is inverted and all other relevant cuts are applied. The schematic of the two branches, together with the number of events that survive after every (set of) cut(s), is shown in Fig. 5.1. Using these numbers, the single-beam background in the 3/3 sample is

$$N_{1bm} = 3 \times \frac{A_{PV_{pnn2}}}{A_{PV_{beam}}} \times \frac{Norm_{1bm}}{R_{DELCO}-1}$$

$$N_{1bm} = 3 \times \frac{0.58}{0.85} \times \frac{1.0\pm1.0}{(4532.0\pm4531.5)-1} = (0.452 \pm 0.452)\cdot 10^{-3} \qquad (5.5)$$

where $\frac{A_{PV_{pnn2}}}{A_{PV_{beam}}} = \frac{0.58}{0.85}$ is the ratio of the acceptance of the nominal PNN2 photon veto cut and the looser PV cut used to produce the beam study numbers (see 6.2). For a conservative estimate of the background, the smallest value of R_{DELCO} from the 3 rejection sub-branches is used.

5.4.2 Double beam

In order to calculate this background, it is assumed that the Čerenkovcounter and the Beam Wire Chambers are uncorrelated with the B4 and the Target, since the Degraders, where the beam particles undergo multiple scattering, are located between them. Therefore, for the rejection branch, 2-beam events are tagged by requiring a hit in the B4 at RS time, and the rejection of the BWCs and the K- or π-Čerenkov(Ck and Cpi respectively) is measured on this sample. In the normalization branch, either the BWCs, or Ck or Cpi are required to have a hit at RS time and all other cuts are applied. A schematic of the 2-beam bifurcation study is shown in Fig. 5.2.

In addition to the B4-tag, KPIGAP is also applied in the rejection branch, which requires the Kaon and pion cluster in the Target to be disconnected in xy. This is done to remove K-decay contamination from the 2-beam sample: either a photon from $K_{\pi2}$or a charged particle from a 3-body decay, both relevant in the PNN2 kinematic region, can give a signal in the B4 at RS time, faking a second beam particle. Such events are not expected to have any BWC or Čerenkovrejection, and should be removed. On the other hand, the rejection of the beam counters does not depend significantly on the proximity of the 2 beam particles, therefore such a subset of events with spacially disconnected

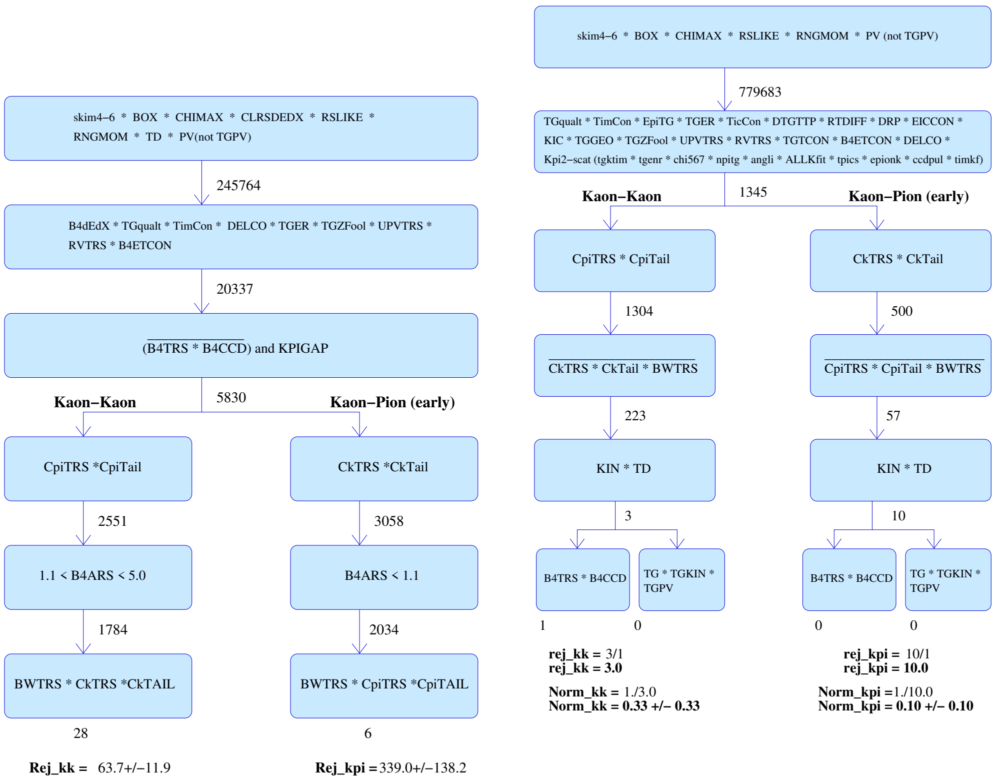

(a) Rejection (b) Normalization

Figure 5.2: Double beam Bifurcations: (a) rejection branch, and (b) normalization branch, for both K-K and K-π. Numbers under the boxes are the number of events remaining after the cuts were applied. The K-π numbers are for the early runs (before the change in trigger) and the K-K numbers are from all runs.

beam particles, can be used to measure the rejection.

Both the rejection and normalization branches bifurcate into K-K and K-π sub-branches, requiring a Cpi or Ck veto respectively, before either inverting Ck or Cpi, or measuring its rejection. The normalization branch bifurcates further at the bottom, in order to handle the small statistics, therefore the K-K (K-π) normalization numbers are given by

$$Norm_{KK(K\pi)} = \frac{n_{KK(K\pi)}}{r_{KK(K\pi)}} \tag{5.6}$$

where $n_{KK(K\pi)}$ is the number of events remaining in the B4TRS*B4CCD sub-branch, and $r_{KK(K\pi)}$ the rejection of TG*TGKIN*TGPV.

K-K background

Using the method described above, and the results from Fig. 5.2, the K-K 2-beam background is

$$N_{KK} = 3 \times \frac{A_{PV_{pnn2}}}{A_{PV_{beam}}} \times \frac{Norm_{KK}}{R_{KK} - 1} \tag{5.7}$$

and, using Eq. (5.6),

$$N_{KK} = 3 \times \frac{0.58}{0.85} \times \frac{\frac{1.0 \pm 1.0}{3.0 \pm 2.4}}{(63.7 \pm 11.9) - 1} = 0.0109 \pm 0.0109 \tag{5.8}$$

K-π background

A complication arises when the K-π is to be calculated, due to the addition of the Cpi veto to the online trigger in the middle of the run. The offline Cpi rejection is very low for the late part of the run, and the normalization branch runs out of statistics, producing an unnaturally hight background with large uncertainty. Therefore it is impossible to just add the K-π background for the early and late part of the run. Instead, the background calculated for the set of runs before the trigger change was scaled by the difference in KB_{live} of the two parts of the run $f_{KB_{live}} = \frac{0.606}{0.394} = 1.54$:

$$N_{K\pi} = 3 \times \frac{A_{PV_{pnn2}}}{A_{PV_{beam}}} \times (1 + f_{KB_{live}}) \times \frac{Norm_{K\pi}}{R_{K\pi} - 1}$$

$$N_{K\pi} = 3 \times \frac{0.58}{0.85} \times (1 + 1.54) \times \frac{\frac{1.0 \pm 1.0}{10.0 \pm 9.5}}{(339.0 \pm 138.2) - 1} = (1.54 \pm 1.54) \cdot 10^{-3} \quad (5.9)$$

5.4.3 Total beam background

Summarizing the previous results, the total beam background expected in the signal region for the 3/3 sample is

$$N_{beam} = N_{1bm} + N_{KK} + N_{K\pi} = (12.9 \pm 12.9) \cdot 10^{-3} \quad (5.10)$$

5.5 Muon backgrounds

5.6 $K^+ \to \pi^+\pi^-e^+\nu$

The K_{e4}decay with a BR of $(4.08 \pm 0.09) \times 10^{-5}$ and with the π^+ maximum momentum at 203 MeV/c could be a serious background in the PNN2 region because this decay contains no photon in the final state to veto on and the π^- and the e^+ could be invisible. Fig. 5.3 shows the total kinetic energy (T_2) of the π^- and the e^+ versus the momentum of the π^+ (P_{tot}) for Monte Carlo

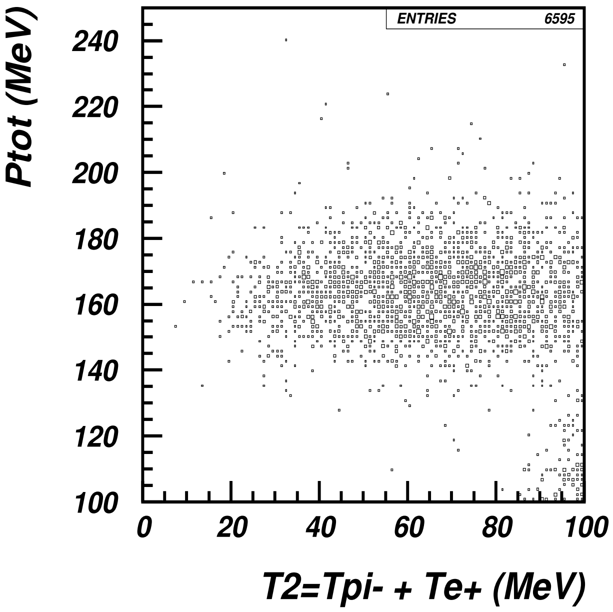

Figure 5.3: Total kinetic energy (T_2) of the π^- and the e^+ versus the momentum of the π^+ (P_{tot}) for Monte Carlo events that pass the $\pi\nu\overline{\nu}(2)$ trigger.

events that passed the $\pi\nu\overline{\nu}(2)$ trigger. When T_2 is very low, for instance below 50 MeV, the π^- and the e^+ can not fly out of target and they might escape detection if they deposit all their energy in some insensitive material or if their hits on target fibers overlap with kaon fibers. For these low T_2 events the distribution of P_{tot} concentrates around 160 MeV, which is in the range of the pnn2 signal box.

5.6.1 Background estimate using data

The two cuts that are most effective against this background are TGPV·OPSVETO and CCDPUL. TGPV·OPSVETO removes events with extra hits in target fibers except for kaon and pion fibers (classified as "photon" and "opposite side pion" fibers respectively), and $CCDPUL$ removes events with extra hits hidden under the Kaon fibers.

Two K_{e4}background branches are selected in data skim5 by $\overline{TGPV \cdot OPSVETO}$ or $\overline{CCDPUL}$. The events remaining after every cut in these branches are listed in Table 5.4. Some cuts have been loosened in this study, in order to avoid revealing part of the signal box, therefore a background estimate using the results of this table will be a conservative one. For instance, the Photon Veto cuts are at E949 pnn1 level (95% acceptance), the time interval and energy threshold of TGPV and OPSVETO have been loosened from their nominal values to 1.3 ns and 5 MeV and 3 ns and 2 MeV respectively, and the CCD-PUL energy threshold is set to 2 MeV.

The events that remain at the end of each branch were scanned by eye to understand the nature of them, and a significant contamination of $K_{\pi2}$scatters, $K^+ \to \pi^+\mu^+\mu^-$ and other decays was found, among the K_{e4}ones. Therefore, the data themselves cannot be used to calculate this background, because a clean sample of K_{e4}cannot be isolated. The TGPV·OPSVETO and CCDPUL rejection will be calculated with Monte Carlo, and the data will be used for normalization, in order to get a conservative background prediction.

5.6.2 Background study with UMC

In order to understand the rejection of TGPV·OPSVETO and CCDPUL, Monte Carlo is used to simulate the energy deposit of charged tracks in the target. The main source of uncertainty in simulation comes from the absorption of π^- in the target. The π^- absorption is modeled with an experimental measurement of stopped π^- in the Range Stack ([33]). Fig. 5.4 shows the

Cut	$\overline{TGPV \cdot OPSVETO}$	$\overline{CCDPUL}$
TRIGGER	30995248 (1.000)	30995248 (0.704)
BOX	1201592 (0.038)	1201592 (0.038)
PCUTS	423959 (0.352)	423959 (0.352)
TDCUTS	179203 (0.422)	179203 (0.422)
KCUTS	112435 (0.627)	112432 (0.627)
PRESEL	8593 (0.076)	8594 (0.076)
RCUT	7346 (0.854)	5923 (0.689)
PVICVC	3303 (0.449)	2901 (0.489)
EPITG	2725 (0.825)	2329 (0.802)
EPIMAX	2500 (0.917)	2156 (0.925)
TGER	2490 (0.996)	2149 (0.996)
TARGF	2071 (0.831)	1912 (0.889)
DTGTTP	2069 (0.999)	1912 (1.000)
RTDIF	2040 (0.985)	1880 (0.983)
DRP	1889 (0.925)	1752 (0.931)
EIC	1742 (0.922)	1628 (0.929)
TIC	1742 (1.000)	1628 (1.000)
TGDEDX	969 (0.556)	953 (0.585)
TGENR	792 (0.817)	794 (0.833)
PIGAP	770 (0.972)	769 (0.968)
TGLIKE	680 (0.883)	695 (0.903)
TGB4	615 (0.904)	638 (0.917)
PHIVTX1	392 (0.637)	456 (0.714)
PHIVTX2	378 (0.964)	445 (0.975)
CHI567	262 (0.693)	312 (0.701)
NPITG	262 (1.000)	312 (1.000)
VERRNG	223 (0.851)	276 (0.884)
CHI5MAX	220 (0.986)	272 (0.985)
ANGLI	220 (1.000)	272 (1.000)
KIC	220 (1.000)	272 (1.000)
EPIONK	217 (0.986)	269 (0.988)
TGKTIM	197 (0.907)	246 (0.914)
TGEDGE	192 (0.974)	241 (0.979)
TIMKF	116 (0.604)	149 (0.618)
B4EKZ	108 (0.931)	135 (0.906)
ALLKFIT	95 (0.879)	122 (0.903)
FINALCUT	15 (0.158)	42 (0.344)

Table 5.4: The normalization branches of data, using $\overline{TGPV \cdot OPSVETO}$ and $\overline{CCDPUL}$. PRESEL contains DELCO6, B4TIM, TGZFOOL and all Photon Veto cuts except that for IC and VC. RCUT means $\overline{TGPV \cdot OPSVETO}$ in the $\overline{TGPV \cdot OPSVETO}$ branch and $\overline{CCDPUL}$ in the $\overline{CCDPUL}$ branch. FINALCUT means $CCDPUL$ in the $\overline{TGPV \cdot OPSVETO}$ branch and $TGPV \cdot OPSVETO$ in the $\overline{CCDPUL}$ branch.

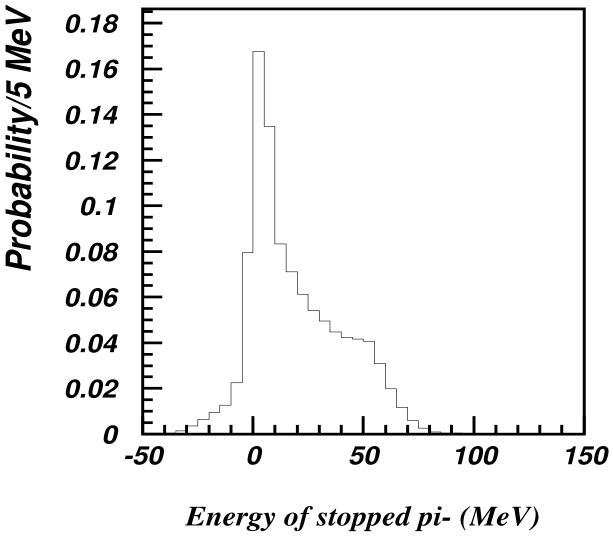

Figure 5.4: Observable energy of π^- stopped in the target.

energy distribution of stopped π^- from that experiment. In simulation, the absorption energy is sampled according to this distribution. If the energy is sampled to be negative, then the last fiber on the π^- trajectory is assigned 0 energy. This model, however, assumes that all the observable energy is deposited locally and promptly. All the absorption energy is deposited in a single fiber, where the π^- stopped. Possible energy deposit in neighboring fibers from the relatively energetic photons that are produced in π^--Carbon absorption as well as deposits from neutrons outside the target are not simulated.

About 2×10^8 events were simulated using this model, with an additional cut at $T2 < 50MeV$, in order to enhance the phase space region most responsible for the background. To study the correlation between TGPV·OPSVETO and CCDPUL, two variables were used: the energy deposit in target fibers except for kaon and pion fibers T_{xtg}, corresponding to TGPV·OPSVETO, and the total energy deposit of pions and electrons in kaon fibers E_{hide}, corresponding to CCDPUL. Because there are no CCD simulated in UMC, E_{hide} is a reconstructed variable from UMC truth.

Table 5.5 shows the number of events left after the application of all possible cuts to MC data, and Fig. 5.5 the relation between E_{hide} and T_{xtg} for the surviving events. In Table 5.6 the rejection of TGPV·OPSVETO is calculated as a function of the cut on E_{hide}, which simulates the effect of the $CCDPUL$ cut. Since the matching of the energy between MC and Data is uncertain, the cut on E_{hide} is varied between 1.5 and 10 MeV, and the cut on T_{xtg} between 0.6 and 1.8 MeV. The rejections of TGPV·OPSVETO are in the same order of magnitude.

5.7 $K^+ \rightarrow \pi^+\pi^o\gamma$

The background due to radiative $K_{\pi2}$is expected to be small, due to the small branching ratio of this decay compared to $K_{\pi2}$and the existence of the third photon available to veto on. From the two processes through which this decay proceeds, direct emission with $BR(DE) = (4.7 \pm 0.9) \times 10^{-6}$ and inner Bremsstrahlung with $BR(IB, 55MeV < T_{\pi^+} < 90MeV) = (2.75 \pm 0.15) \times 10^{-4}$, the latter is only of interest, due to its higher Branching Ratio.

Since it is difficult to separate this background sample from the $K_{\pi2}$-scatter background sample, both Monte Carlo and data were used to measure it. The method consisted of determining the expected number of $K_{\pi2\gamma}$events in the $\pi\nu\overline{\nu}(2)$ kinematic region as a function of the number of $K_{\pi2}$peak events observed outside the search region. In order to normalize the number of $K_{\pi2\gamma}$events to the number of $K_{\pi2}$peak events, it is necessary to know the

Cut	Events (Acceptance)
Kstops	199998880. (1.00000)
TRIGGER	10691979. (0.05346)
BOX	9928203. (0.92857)
PCUTS	0. (0.00000)
TDCUTS	0. (0.00000)
KCUTS	7697728. (0.77534)
PRESEL	3894473. (0.50592)
RCUT	0. (0.00000)
PVICVC	2316910. (0.59492)
EPITG	2220561. (0.95841)
EPIMAX	2164988. (0.97497)
TGER	2161579. (0.99843)
TARGF	2147258. (0.99337)
DTGTTP	2146393. (0.99960)
RTDIF	2111778. (0.98387)
DRP	1841553. (0.87204)
EIC	1680279. (0.91242)
TIC	0. (0.00000)
TGDEDX	1133592. (0.67465)
TGENR	961622. (0.84830)
PIGAP	934673. (0.97198)
TGLIKE	885761. (0.94767)
TGB4	0. (0.00000)
PHIVTX1	401995. (0.45384)
PHIVTX2	381786. (0.94973)
CHI567	99680. (0.26109)
NPITG	99680. (1.00000)
VERRNG	63997. (0.64202)
CHI5MAX	63773. (0.99650)
ANGLI	63436. (0.99472)
KIC	63436. (1.00000)
EPIONK	63425. (0.99983)
TGKTIM	0. (0.00000)
TGEDGE	0. (0.00000)
TIMKF	0. (0.00000)
B4EKZ	0. (0.00000)
ALLKFIT	63425. (1.00000)

Table 5.5: The number of events remaining after all possible pass2 cuts for MC. PRESEL cut means DELCO6, TGZFOOL, and all Photon Veto cuts except that for IC and VC.

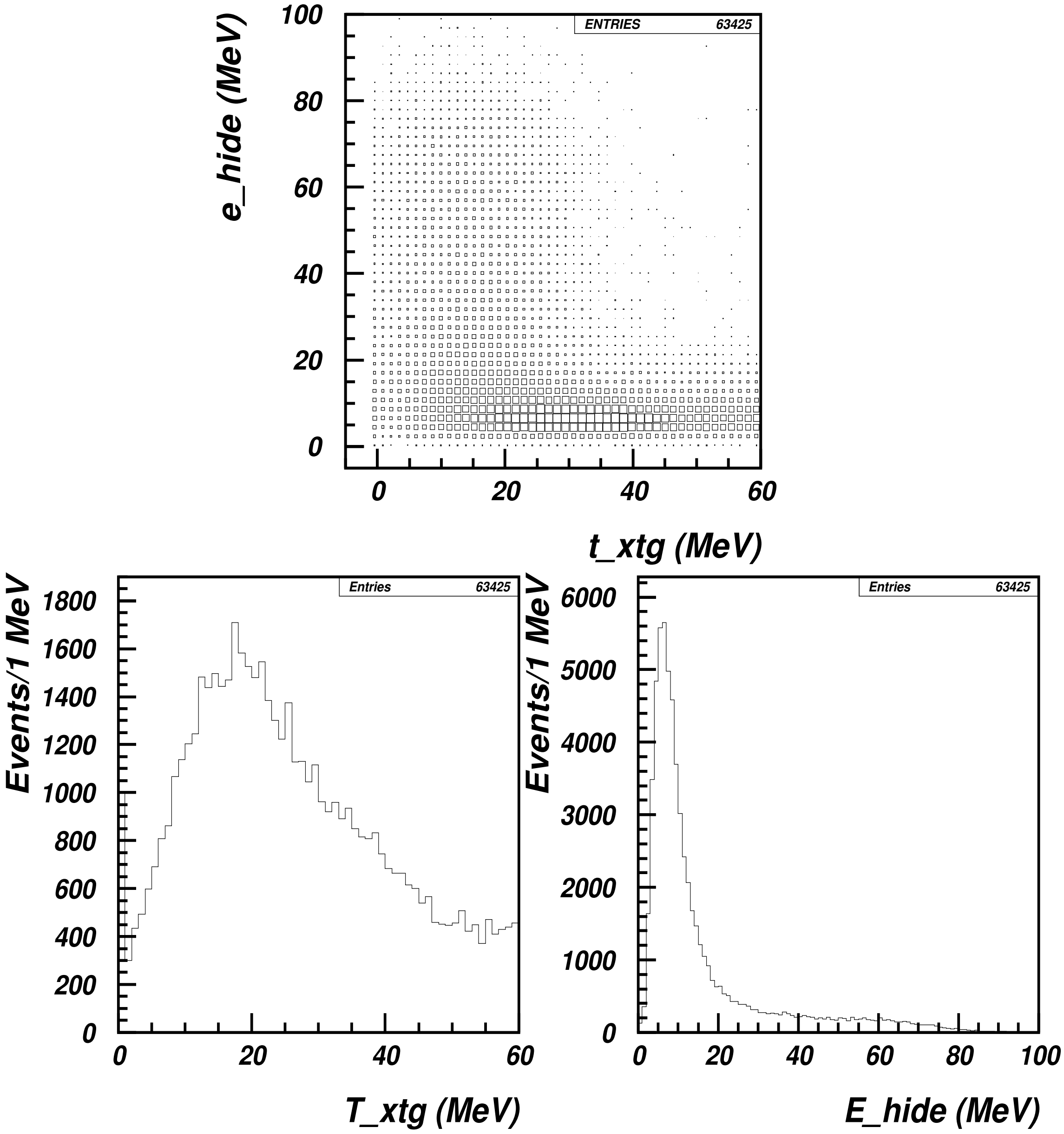

Figure 5.5: E_{hide} versus T_{xtg} (top) and projections on T_{xtg} (bottom left) and E_{hide} (bottom right).

	$T_{xtg} < 0.6$	$T_{xtg} < 1.2$	$T_{xtg} < 1.8$
$E_{hide} < 1.5$	245/12 (20)	245/18 (14)	245/18 (14)
$E_{hide} < 2.5$	1104/27 (40)	1104/34 (31)	1104/36 (31)
$E_{hide} < 4.0$	5609/61 (91)	5609/70 (80)	5609/78 (80)
$E_{hide} < 10.0$	34943/264 (132)	34943/313 (112)	34943/354 (99)

Table 5.6: Rejection of cuts on T_{xtg} with different cuts on E_{hide}.

Requirement	$K_{\pi 2}$	$K_{\pi 2\gamma}$
K^+ decays ($N^{UMC}_{K_{\pi 2(\gamma)}}$)	199992	499968
$\pi\nu\overline{\nu}(2)$ trigger	20455	49355
offline cuts ($N_{K_{\pi 2(\gamma)}}$)	4950	6907

Table 5.7: Trigger simulation and offline analysis results on $K_{\pi 2}$and $K_{\pi 2\gamma}$simulated samples.

branching ratio and the rejection of both the online and offline cuts for each decay. This information was calculated using MC.

About 2×10^5 $K_{\pi 2}$and 5×10^5 $K_{\pi 2\gamma}$events were generated with MC. Fig. 5.6 shows the π^+ kinetic energy spectrum of the $K_{\pi 2\gamma}$events produced. The BR in the region of interest ($0MeV < T_{\pi^+} < 106MeV$) can be calculated from this distribution as:

$$BR(K_{\pi 2\gamma}) = \frac{\int_0^{106} dN}{\int_{55}^{90} dN} \times (2.75 \pm 0.15) \times 10^{-4} = (1.11 \pm 0.06) \times 10^{-3} \quad (5.11)$$

Then the online $\pi\nu\overline{\nu}(2)$ trigger and the offline cuts were applied to the simulated samples (Table 5.7). From the number of events remaining and the branching ratio of each decay, the ratio of $K_{\pi 2}$events in the kinematic peak over the $K_{\pi 2\gamma}$events in the PNN2 region can be determined as :

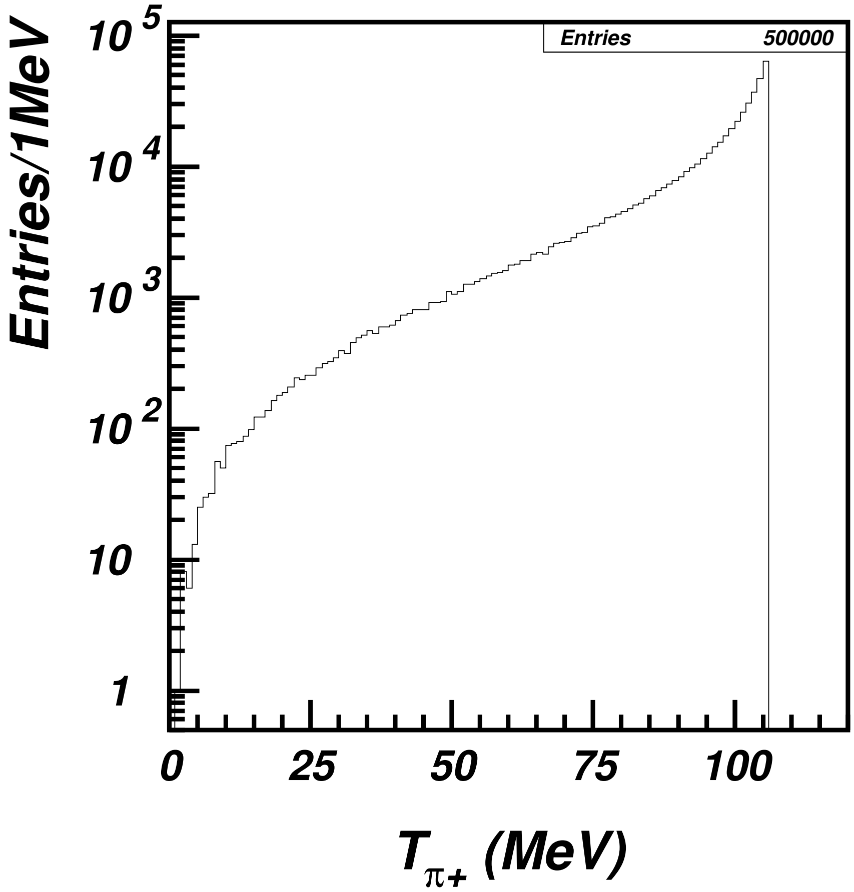

Figure 5.6: Pion energy spectrum from $K_{\pi 2\gamma}$generated by MC, using only the inner Bremsstrahlung process.

$$\begin{aligned}\kappa &= \frac{N_{K_{\pi 2}}}{N_{K_{\pi 2\gamma}}} \times \frac{BR(K_{\pi 2})}{BR(K_{\pi 2\gamma})} \times \frac{N^{UMC}_{K_{\pi 2\gamma}}}{N^{UMC}_{K_{\pi 2}}} \\ &= \frac{4950}{6907} \times \frac{0.2117}{(1.11\pm 0.06)\times 10^{-3}} \times \frac{499968}{199992} \\ &= 341 \pm 17 \end{aligned} \tag{5.12}$$

The rejection due to the photons from the π^o for both $K_{\pi 2}$and $K_{\pi 2\gamma}$decay can be expected to be roughly equal. However, due the presence of the extra photon, the total Photon Veto rejection for the $K_{\pi 2\gamma}$decay is expected to be higher than for $K_{\pi 2}$. The single photon detection inefficiency of the detector has been measured as a function of the energy and angle of the additional photon in [34]. Using these measurements and the energy and angular distribution of the additional photon for the 6907 events which passed all the analysis cuts (Fig. 5.7), the rejection due to the additional photon was measured to be

$$R_\gamma = \frac{1}{\epsilon_\gamma} = 5.40 \tag{5.13}$$

where ϵ_γ is the total single photon detection inefficiency from the convolution of the distribution in Fig. 5.7 and the map in [34].

Using the ratio of $K_{\pi 2}$events in the kinematic peak over the $K_{\pi 2\gamma}$events in the PNN2BOX from the MC study, and the additional Photon Veto rejection due to the presence of the extra photon in the $K_{\pi 2\gamma}$decay, the radiative K2 background can be measured as

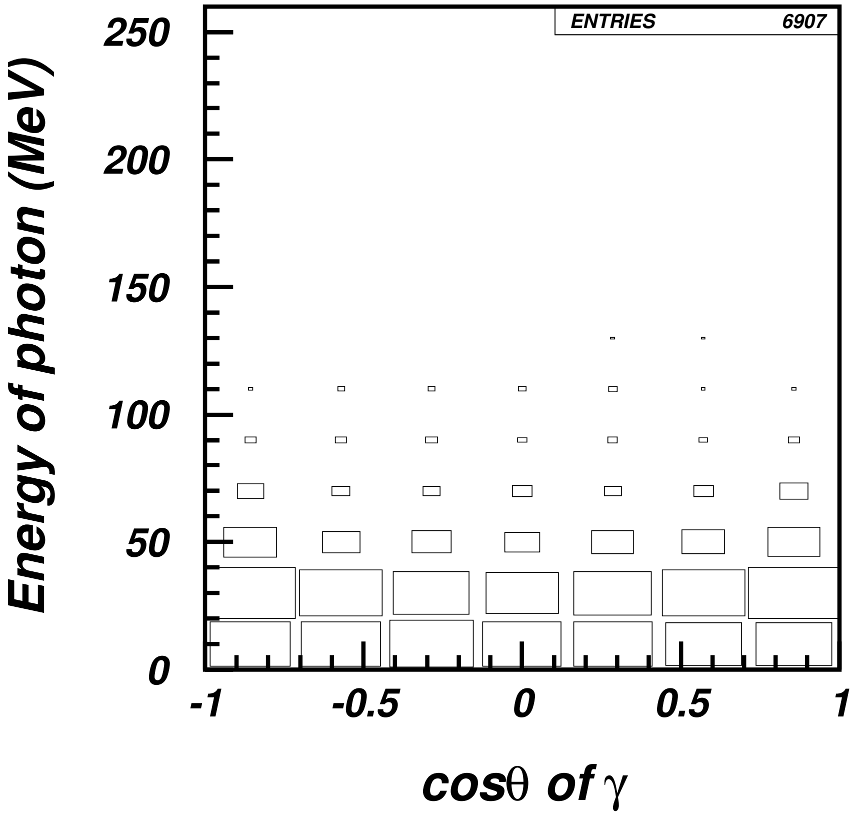

Figure 5.7: Energy vs polar angle of the non-π^o photon from the $K_{\pi 2\gamma}$MC events that passed all the cuts.

Background	Events in the 3/3 sample
$K_{\pi 2}$TG scatter	0.310 ± 0.219
$K_{\pi 2}$RS scatter	0.016 ± 0.006
Beam	0.013 ± 0.013
Muon	
K_{e4}	
$K_{\pi 2\gamma}$	0.031 ± 0.002
CEX	
TOTAL	

Table 5.8: Total background estimation.

$$N_{K_{\pi 2\gamma}} = 3 \times \frac{N^{data}_{K_{\pi 2}}}{\kappa R_\gamma} = 3 \times \frac{19}{(341 \pm 17) \cdot 5.4} = 0.031 \pm 0.002 \tag{5.14}$$

where $N^{data}_{K_{\pi 2}}$ is the number of events in the $K_{\pi 2}$kinematic peak which survived all the analysis cuts, used to generate class 1 of Table 5.1.

5.8 Charge Exchange (CEX) background

5.9 Background summary

The total background expected in the signal region based on the 1/3 sample analysis is summarized in Table 5.8

This result is an improvement of about a factor of 2(?) compared to the E787 PNN2 result [31].

5.10 Outside-the-box study

In order to verify that the bifurcation cuts are uncorrelated, the outside-the-box (OTB) study was performed on the major ($K_{\pi 2}$TG scatter) background. The Photon Veto was loosened to its loosest parameters (at 85% acceptance) and the CCDPUL cut to a threshold of 2 MeV pion energy, and the background study was repeated. The number of background events expected in the OTB region for every rejection class (see 5.2) is listed in Table 5.9. About 3.5 events were expected, and 1 was observed, which is in agreement with this expectation.

	background
CLASS 2	3.45014±0.9
CLASS 5	3.41792±0.9
CLASS 7	3.14669±0.6
CLASS 9	3.35115±0.9
CLASS 12	3.51692±0.9
measured	1

Table 5.9: The expected $K_{\pi 2}$TG scatter background in the outside-the-box region defined by the loosest PV and a loose CCDPUL cut, for rejection classes with significant statistics. One event was observed in that region.

5.11 1 and 2 cut failures

Chapter 6

Acceptance measurement

6.1 Introduction

6.2 $K_{\mu 2}$ based acceptance

6.3 π_{scat} based acceptance

6.4 $K_{\pi 2}$ based acceptance

6.5 UMC based acceptance

6.6 $T \cdot 2$ efficiency

6.7 Kaon stopping fraction f_s

6.8 Measurement of the $K_{\pi 2}$ Branching Ratio

6.9 Acceptance summary and Single Event Sensitivity (SES)

Chapter 7

Conclusion

Chapter 8

Appendix

A Analysis cuts

A.1 PASS1 level

These basic cuts are applied as a pre-selection to all the analysis samples, therefore they are not mentioned in the background studies.

- Trigger Bit (TRBIT)

  The event passes the online trigger bit of $\pi\nu\overline{\nu}$.

- Data Taking Quality (BAD_RUN)

  Events in runs during which problems on the beam, detector, or electronics occured are removed.

- Charged Track Reconstruction (RD_TRK)

  The track is reconstructed in the Range Stack.

- Track Time Reconstruction (TRKTIM)

  The average time of the track hits in the Range Stack is obtained.

- Consistency between Online and Offline Stopping Counters (STLAY)

  The stopping counter that is found by the online Stopping Counter Finder (SCF) should be the same as that found by the offline track finding routine.

- Stopping Counter Performance (BAD_STC)

  Some TD channels had problems recording input signals in specific periods of data taking. These "bad TD channels" were listed during the detector calibration. The charged track should not stop in the counters where the corresponding TDs were unable to record signals properly.

- Track Fitting in UTC (UTC)

  The track is successfully reconstructed in the UTC.

- Matching Between UTC and RS Tracks (UTC/RANGE)

  The track reconstructed in the UTC should point to the T•2 sector in the RS.

- Target Reconstruction (TARGET)

  The target reconstruction is successfully done.

- Momentum in UTC (PDC)

  The momentum measured by the UTC should be less than 280 MeV/c. This requirement removes failures of UTC pattern recognition.

- $\pi^+ \to \mu^+$Double-Pulse Fitting (FITPI)

$\pi^+ \rightarrow \mu^+$double pulses were found by fitting TD pulses in the stopping counter.

- Photon Veto around the Stopping Counter (RSHEX)

  No extra hit is allowed in the counter after the stopping counter and the hextants that do not have track hits.

- Sector Crossing Cut (RSHEX2)

  No sector crossing is allowed in the stopping layer.

- π^+ Stop Fiducial Requirement (LAY14)

  The charged track should not come to rest in the support materials for the RSSC second layer, which is embedded between the RS layers 14 and 15.

A.2 PASS2 level

- Crude Photon Veto Cut (PVCUT)

  Perform photon veto in the Barrel Veto (BV), End Cap (EC) and Range Stack (RS). Photon hits that are coincident with the charged track time are selected. Events are rejected if the energy sum of these in-time hits in each subsystem is above the threshold. The time windows and energy thresholds are summarized in Table 8.1.

- Target Reconstruction Cut (TGCUT)

  This cut consists of the following requirements:

  - The Kaon decay vertex is inside the target.

Subsystem	Time Window	Energy Threshold
Barrel Veto	± 2.0 ns	1.5 MeV
End Cap	± 1.5 ns	3.5 MeV
Range Stack	± 1.5 ns	3.0 MeV

Table 8.1: The time windows and energy thresholds for Barrel Veto, End Cap and Range Stack.

- The time difference between the average time of the kaon fiber hits in the target (target kaon time tk) and the B4 Hodoscope hit time is within 4 ns.
- The time difference between the average time of the pion fiber hits in the target (target pion time tpi) and the I-Counter hit time is within 5 ns.
- The energy deposit in the I-Counter should be consistent with that of pions.

- Accidentals at Muon Time (TDCUT)

  Search for accidental activity in the RS that is coincident with the second pulse time (muon time) in the stopping counter. Events are rejected if the energy sum of the coincident hits exceeds a threshold.

- Beam dE/dx & Double Beam Cut (PSCUT)

  Require that the energy deposit in the B4 Hodoscope is greater than a specific value and no extra beam particle coincident with the track time is recorded.

- Target Photon Veto Cut (TGPVCUT)

  Require no extra activity other than kaon and pion hits in the target.

This cut rejects events with photon activity in the target and events with an extra beam particle in the target.

- Delayed Coincidence Cut (DELCO2)

  Require that kaons should decay at least 2 ns after entering the target.

Using these cuts, 6 data "SKIMS" (3 for the 1/3 and 3 for the 2/3 sample) are prepared, in order to minimize processing time. Each SKIM is rich in a different background.

- SKIM1 (5 for the 1/3), for $K_{\pi 2}$: TGCUT, PSCUT, TDCUT, TGPVCUT.
- SKIM2 (6 for the 1/3), for $K_{\mu 2}$: TGCUT, PSCUT, PVCUT, TGPVCUT, DELCO2.
- SKIM3 (7 for the 1/3), for beam scatters: TGCUT, TDCUT, PVCUT.

A.3 Kinematic Cuts (KCUT)

Fiducial Cuts

- Stopping Layer Requirement (LAYV4)

  Require that the π^+ stopping layer is between 5 and 18, which ensures the π^+ stops in the Range Stack as requested in the trigger.

- Layer 14 Cut (LAYER14)

  No charged track is allowed to come to rest in the RSSC second layer embedded between RS layers 14 and 15. Events are rejected if the stopping layer is 14 and a prompt RSSC hit is found in the same sector or one sector clockwise of the stopping counter.

- Polar Angle Cut (COS3D)

  Require that the cosine of the polar angle of a charged track ($\cos\theta$) is within ± 0.5 ($|\cos\theta| \leq 0.5$).

- Stopping Z Position Cut (ZFRF)

  Require that the π^+ stopping z position in the Range Stack ($Z_{\pi stop}$) is within the fiducial volume. The cut position depends on the stopping layer of the event.

Stopping Layer	Cut Condition
11,12	$-35 \leq Z_{\pi stop} \leq 35cm$
13	$-40 \leq Z_{\pi stop} \leq 40cm$
14	$-30 \leq Z_{\pi stop} \leq 30cm$
15,16,17,18	$-50 \leq Z_{\pi stop} \leq 50cm$

Table 8.2: Cut conditions of π^+ stopping z position for various stopping layers.

- Fiducial Cut in UTC (ZUTOUT)

  The charged track should pass through the UTC fiducial volume. The z position at the UTC outer layer should be within the active region ($|\mathrm{z}| \leq 25cm$).

Track Reconstruction Cuts

- Track Reconstruction in the UTC (UTCQUAL)

  Reject events with poor UTC fits in either x-y or z. Events with overlapping tracks are also rejected.

- RS Track Reconstruction and Matching with the UTC Track (PRRF)

  This cut rejects events with the charged track scattering in the Range Stack. It consists of the following criteria:

  - χ^2 Probability Cut for RS Track Reconstruction (PRRF1)

    Reject events if the quality of the Range Stack track fitting in the x-y plane is poor. The RS track fitting is performed using sector crossing positions, RSSC hit positions, and energy deposit in the π^+ stopping counter.

  - Track Matching in RSSC Z Measurements (PRRFZ1)

    Reject events if the track reaches the RSSCs and the matching in the r-z plane between the UTC extrapolation and the RSSC hit positions is poor.

  - Track Matching in RS Z Measurements (PRRFZ2)

    Reject events if the matching in the r-z plane between the UTC extrapolation and the track hit positions derived from end-to-end timing in the RS counters is poor.

dE/dx Cuts in the Range Stack

- Maximum Energy Deviation in RS (CHIMAX)

  Deviations of energy deposits in the individual track counters are examined.

  $$\chi_i \equiv \frac{\log E^i_{exp} - \log E^i_{meas}}{\sigma^i} \tag{A.1}$$

  where E^i_{meas} is the measured energy deposit in the ith track counter and E^i_{exp} is the energy in the ith track counter expected from the measured range. Reject events with the absolute value of the largest χ_i greater than or equal to 4.

- Confidence Level in RS Energy Measurements (CLRSDEDX)

  The confidence level is calculated from the energy deviations in the individual track counters. The cut position is at 0.04.

- Likelihood Cut for RS Energy Measurements (RSLIKE)

  A likelihood is constructed from the energy deposits in the track counters. The likelihood value is required to be between 0 and 10.

π/μ **Separation in Range Stack**

- Range-Momentum Consistency (RNGMOM)

  The deviation of range in the Range Stack (χ_{R-P}) is required to be

$$\chi_{R-P} \equiv \frac{R_{meas} - R_{exp}}{\sigma_R} \leq 2.2$$

  where R_{exp} is the range expected from momentum with the assumption that the charged track is a pion.

Phase Space Cuts

- Small PNN2 Box

  Fixed cut on the momentum, energy and range, as inherited from E787:

$$\begin{aligned} 140MeV/c &\leq ptot \leq & 195MeV/c \\ 60MeV &\leq etot \leq & 95MeV \\ 12cm &\leq rtot \leq & 27cm \end{aligned}$$

- Expanded (nominal) PNN2 Box

  The upper p, E and R limits are expanded, using the deviations from the $K_{\pi 2}$ peak ($P_{peak} = 205.1MeV/c$, $E_{peak} = 108.6MeV$, $R_{peak} = 30.4cm$):

$$\begin{aligned} P_{dev} \equiv \frac{P_{peak} - ptot}{\sigma_P} \geq 2.5 &\implies ptot \leq 199MeV/c \\ E_{dev} \equiv \frac{E_{peak} - etot}{\sigma_E} \geq 2.5 &\implies etot \leq 100.5MeV \\ R_{dev} \equiv \frac{R_{peak} - rtot}{\sigma_R} \geq 2.75 &\implies rtot \leq 28cm \end{aligned}$$

  where σ_P, σ_E and σ_R are the sigmas of the $K_{\pi 2}$ peak momentum, energy and range respectively .

A.4 Beam Cuts (PSCUT06)

Single-Beam Cuts

- dE/dx in B4 Hodoscope (B4DEDX)

  Kaon identification is performed by examining the dE/dx in the B4 Hodoscope, which is required to be greater than or equal to 1.85 MeV.

- Kaon Stop Requirement: Delayed Coincidence Cut (DELC)

  The target pion time, t_π, is required to be at least 2 ns later than the target kaon time, t_K ($t_\pi - t_K \geq 2ns$). The cut position is tightened if either target kaon or pion times have a large uncertainty

  - $t_\pi - t_K \geq 5ns$ if the discrepancy between the target kaon time and B4 hit time is greater than 1 ns.
  - $t_\pi - t_K \geq 6ns$ if the discrepancy between the target pion time and track time is greater than 1.5 ns.
  - $t_\pi - t_K \geq 5ns$ if t_π is obtained from the time of the I-Counter hit, not from the target pion fiber hits.
  - $t_\pi - t_K \geq 4ns$ if the energy deposit of a kaon in the target is less than or equal to 50 MeV.
  - $t_\pi - t_K \geq 3ns$ if there are less than 4 target pion fibers found.
  - $t_\pi - t_K \geq 3ns$ if the beam likelihood value is less than 200 (to be explained in the Pathology Cuts section).
  - $t_\pi - t_K \geq 4ns$ if the discrepancy between any of the individual kaon fiber times and the average kaon time is greater than 2 ns.
  - $t_\pi - t_K \geq 4ns$ if the discrepancy between any of the individual pion fiber times and the average pion time is greater than 3.5 ns.

Double-Beam Cuts

- Double-Pulse Fitting in B4 Hodoscope (B4CCD)

  Pulses recorded in the B4 CCD are fitted with a double-pulse assumption. Reject events if hit modules have a signature of double pulses, and the average time of the fitted second pulses is within ±3.5 ns of the track time. The signature of double pulses is a ratio of the single-pulse fit χ^2 to the double-pulse fit χ^2 that is greater than a certain value, and the energy of the fitted second pulse exceeds a threshold.

- Timing in B4 Hodoscope (B4TRS)

  Events are rejected if the average TDC time of hit modules in the B4 Hodoscope is within ±2.5 ns of the track time, or the average CCD time of hit modules is within ±1.5 ns of the track time when the energy sum is above a threshold.

- Timing in BWPCs (BWTRS)

  Events are rejected if the time of a hit cluster in any Beam Wire Chamber is within ±4.5 ns of the track time.

- Timing in Kaon ČerenkovCounter (CKTRS)

  Events are rejected if the average TDC or CCD time of hits in the Kaon ČerenkovCounter is within ±2 ns of the track time.

- Extra Timing Cut in Kaon ČerenkovCounter (CKTAIL)

  The average time of hits in the Kaon ČerenkovCounter, obtained from the trailing edge of the pulses (minus the TDC width), should not be coincident with the track time. The time windows for this cut is dependent on the value of $t_\pi - t_K$.

- $t_\pi - t_K < 15ns$: events are rejected if there are any hits within ± 3 ns of the track time.
- $15 \leq t_\pi - t_K < 25ns$: events are rejected if there are any hits within ± 3.5 ns of the track time.
- $t_\pi - t_K \geq 25ns$: events are rejected if there are any hits within ± 2 ns of the track time.

- Timing in Pion ČerenkovCounter (CPITRS)

  Events are rejected if the average TDC or CCD time of hits in the Pion ČerenkovCounter is within ± 2 ns of the track time.

- Extra Timing Cut in Pion ČerenkovCounter (CPITAIL)

  The average time of hits in the Pion ČerenkovCounter, obtained from the trailing edge of the pulses (minus the TDC width), should not be coincident with the track time. The event is rejected if there are any hits within ± 2 ns of the track time.

Pathology Cuts

- Consistency Cut between B4 Hodoscope Analyses (B4ETCON)

  Requires a consistency between TDC, ADC and CCD values in B4 Hodoscope.

- Double-beam Cut in Target (TGGEO)

  Timing information in the I-Counter is used to reject Double Beam background with the following signature:

1. Both particles enter the target from a target edge or an I-Counter
2. the first particle or its decay product deposits a large energy pulse in the I-Counter
3. the first particle enters the target, decaying downstream or decaying very late (i.e., the decay product is not detected).

The second particle is scattered upstream of the beam line and misses some beam counters. Later, by multiple scattering, it enters the target and intersects the hit fibers of the first beam particle. These signatures fool the target reconstruction.

- Target Reconstruction (TGQUALT)

  The kaon vertex is reconstructed inside the target.

- Timing Consistency between Target and B4 Hodoscope (TIMCON)

  Require the consistency between the target kaon time (t_K) and the time of hit in the B4 Hodoscope (t_{B4}), and between the target pion time (t_π) and the track time (t_{RS}).

$$|t_K - t_{B4}| \leq 3.0 \text{ ns} \quad \text{and} \quad -4.5 < t_\pi - t_{RS} < 4.0 \text{ ns} \tag{A.2}$$

- Timing Consistency among Target Kaon Fibers (TGTCON)

  Require consistency between the average time of the kaon fiber hits and the times of the individual kaon fiber hits in the target.

- Photon Veto in Upstream Photon Veto and Ring Veto (UPV/RVTRS)

  Reject events with any activity at track time in the Upstream Photon

Veto or in the Ring Veto.

A.5 Target Quality Cuts (TGCUT06)

- Beam Likelihood Cut (B4EKZ)

  A likelihood is constructed from the energy deposit in the B4 Hodoscope, the energy sum of the kaon fibers and the K^+ stopping z position. The likelihood value is required to be greater than 10. The cut is tightened if the pion time is given by the I-Counter instead of the target. In this case, the likelihood value is required to be greater than 20.

- Target Fiducial Cut (TGZFOOL)

  Require the z position of the kaon decay vertex obtained from the UTC extrapolation to be within the target fiducial volume ($tgz \geq -5cm$). This cut ensures that the kaon decays in the target.

- Energy Cut on Target Pion Fiber (EPITG)

  Require that any target pion fiber should have an energy of less than or equal to 3 MeV.

- Energy Cut on Target Pion Fiber near Decay Vertex (EPIMAXK)

  Require that the target pion fiber closest to the decay vertex should have an energy of less than 3 MeV.

- Target Gap Cut between Kaon and Pion Fibers (TARGF)

  Reject events where the kaon cluster does not touch any pion fiber. The maximum distance allowed is 0.6 cm.

- Matching between Target and UTC (DTGTTP)

  Require that the target and UTC tracks are well matched to each other at the target radius. This cut eliminates events in which the UTC track does not intersect the target edge.

- Quality on Target Path Length Calculation (RTDIF)

  Require a small uncertainty in the calculation of the pion path length in the target. This is equivalent to the pion path hidden under the kaon fibers, and it is required to be less than 1.5 cm.

- Target Kink (DRP)

  The maximum and minimum distance from the center of the target pion fibers to the center of the circle that is fitted to the track path by the UTC are examined. Reject events if the distribution of the pion fibers is broad, namely

  $$\frac{d_{max} - d_{min}}{R_{tg}} > 0.35 \tag{A.3}$$

  where d_{max} and d_{min} are the maximum and minimum distances, respectively, and R_{tg} is the range of the track in the target.

- Time Consistency with the B4 (TGKTIM)

  The time in each target kaon fiber is required to be consistent with the kaon time in the B4 counter and the track time in the Range Stack.

- I-Counter Energy Cut (EIC)

  Require consistency between the measured (E_{meas}) and estimated (E_{est})

energy deposit in the I-Counter.

$$|E_{meas} - E_{est}| \leq 5 \text{ MeV and } (E_{meas} - E_{est}) \leq 1.75 \text{ MeV} \qquad \text{(A.4)}$$

- Timing Consistency between Range Stack and I-Counter (TIC)

  Require timing consistency between the track time (t_{RS}) and I-Counter hit time (t_{IC}).

  $$|t_{RS} - t_{IC}| \leq 5.0 \text{ ns}$$

- Energy in Target Edge Fibers (TGEDGE)

  Reject events with more than 4 MeV energy in any of target edge fibers within ± 5 ns of the track time.

- Target dE/dx Cut (TGDEDX)

  The dE/dx of pions in the PNN2BOX (140 MeV/c to 195 MeV/c) changes from 3.08 MeV/cm to 2.47 MeV/cm in plastic scintillator. A likelihood function was created by using the total measured momentum (ptot), target range (rtg) and the target energy (etg) of beam pion events. The target range was quantified in 5 momentum bins and 15 target energy bins. For each bin, the mean target range and sigma was stored and a likelihood function was created assuming a Gaussian distribution. This cut rejects events if this likelihood, $tgdedx\_like \leq 0.05$.

- Extreme Target Pion Energies (TGENR)

  This cut rejects events if the total pion energy in the target is either too large ($E_{tg} > 28MeV$) or too small ($E_{tg} < 1MeV$).

- Target Gap between Pion Fibers (PIGAP)

  Reject events with a gap between target fibers classified as pion fibers greater than 1.5 cm. This cut is tightened to 1.0 cm when the cosine of the polar angle is negative and the z position of the track in the I-Counter is less than -7 cm.

- Kaon Cluster and Decay Vertex Position Consistency with the B4 and the Pion Fibers (TGB4)

  - Consistency between the B4 Hodoscope and Target Hit Positions (DB4)

    Reject events with a distance from the xy hit position in the B4 Hodoscope to the nearest target kaon fiber of more than 1.8 cm.

  - Extra Consistency Cut between B4 Hodoscope and Target Hit Positions (DB4TIP)

    Reject events with a distance from the xy hit position in the B4 Hodoscope to the nearest extreme tip of a kaon cluster of more than 1.8 cm.

  - Target Gap Cut among Kaon Fibers (DVXTIP)

    Reject events with a distance between the kaon decay vertex and the nearest extreme tip of the kaon cluster of more than 0.7 cm.

  - Target Gap between Kaon and Pion Fibers (DVXPI)

    Reject events with a distance between the kaon decay vertex and the closest pion fiber of more than 1.5 cm.

- Back-to-back Track Cut in Target (PHIVTX)

  Reject events with back-to-back tracks in the target.

- Opposite-side Pion Fibers (OPSVETO)

  The energy sum of the target fibers which are on the opposite side of the pion fibers relative to the decay vertex and are coincident with the target pion time (within ± 4.0 ns), should be less than 1 MeV. The cut is tightened to 0.5 MeV when the beam likelihood value is less than 200.

- Target Likelihood Cut (TGLIKE)

  Events with extra energy hidden in the pion fibers, either from photons or pion scatters, should be removed.

  - A likelihood is constructed from times and energies of the target pion fibers and distances between the UTC extrapolation path and the target pion fiber hit positions (LIKE). The likelihood should be 3.2 or less.
  - Another likelihood is constructed only by the distances between the UTC extrapolated track and the target pion fiber hit positions (LIKE2). This likelihood should be 2.3 or less.

- Time, Energy and Position Cut for Kaon Fibers (TIMKF)

  This cut requires that the times of kaon fibers are consistent with the energy and position of the fiber.

- Pion Fiber Number Cut (NPITG)

  If the number of pion fibers in the target is less than 1, then the event is rejected.

- CCD Pulse Fits in the Kaon Fibers (ALLKFIT)

  This cut requires that all the kaon fibers which have energy more than 3 MeV should have a CCD pulse fit.

- Pion Fiber Time Distribution Width (TPICS)

  This cut rejects events for which the standard deviation of the pion time distribution in the target is greater than 4 ns.

- Pion Energy Under a Kaon Fiber Found by SWATHCCD (EPIONK)

  If the target reconstruction routine ("SWATHCCD") has found a pion fiber overlapping a kaon fiber, then the pion fiber is required to have energy less than 1.5 MeV. This cut removes an inconsistency caused by the use of SWATHCCD. SWATHCCD can find pion hits in kaon fibers for DELCO¿15ns. The cuts on pion fiber energy EPITG and EPIMAXK are at 3 MeV, whereas the cut on pion energy under a Kaon fiber (CCDPUL, explained later) is at 1.25 MeV. Therefore, if a fiber is classied as both kaon and pion and is not properly fit by the CCDPUL algorithm, then the pion energy cut on these fibers would be 3 MeV.

- Target Fitter Matching with Individual Pion Fibers (CHI567)

  A χ^2-like quantity is formed based on

  - the observed and expected energy in all the fibers which have a hit and are a part of the reconstructed pion track in the target (χ^2_5)
  - the minimum distance between the track and the corners of every fiber that has no energy but the track is projected to go through it (χ^2_6)

– the distance between the track and every fiber that has energy but the track is not projected to go through it (χ_7^2)

The cut CHI567 rejects events if the probability of the sum of these three quantities is less than 0.015, where the number of degrees of freedom is $nfree = nfib + 2$, where nfib is the number of fibers used in the fit. The details of these target track fitting quantities can be found in Appendix B of [31].

- Target Fitter Matching with Vertex Fiber (VERRNG)

  This cut rejects events if the fitted track in the target does not intersect the vertex fiber identied by SWATHCCD. If verrng is the projected range of the track in the vertex fiber, then this cut removes events for which $verrng < 0.05cm$.

- Maximum Contribution to the Target Fitter χ_5^2 (CHI5MAX)

  If the contribution from any individual fiber to χ_5^2 is more than 5, then the event is rejected.

- SWATHCCD and UTC Track Fitting Consistency (ANGLI)

  This cut rejects events if the range of the charged track in the target is less than 2cm and the angle between the SWATHCCD reconstructed track and the UTC extrapolated track in the target is greater than 0.01 radian.

- Kaon Time in I-Counter (KIC)

  Events are rejected if target kaon fibers are found near the I-Counter and a hit time in the I-Counter is coincident with the target kaon time.

- Kaon Fiber CCD Pulse Fitting Quality (CCDBADFIT)

  Cut event if both the single and double pulse probability of a fitted fiber with more than the minimum pion energy (1.5MeV) is zero.

- Pion Energy from the CCD Pulse Fitting (CCDPUL)

  Reject events with Kaon fibers whose second pulse found by the CCD fitter has more than 1.25 MeV energy within [-7.5,10.0]ns of pion time.

A.6 $\pi^+ \to \mu^+ \to e^+$ Decay Sequence Cuts

- Pion Time Consistency (TDTCON)

  Events in which an accidental hit plus a sequential hit of a muon track fake the $\pi^+ \to \mu^+$double pulses in the stopping counter should be removed. The first pulse time in the stopping counter, obtained from the TD Double-Pulse Fitting ($t_{\pi,TD}$), is required to be within ± 2.5 ns of the track time (t_{RS}).

$$|t_{\pi,TD} - t_{RS}| \leq 2.5 \text{ ns}$$

- $\mu^+ \to e^+$ Decay Requirement (EV5)

  A signature consistent with the $\mu^+ \to e^+$ decay is required in and around the stopping counter. A cluster of hits coincident with the third pulse time of the stopping counter is searched for around the stopping counter. Reject events if the cluster has hits in counters on both sides of the stopping counter.

- Cut on Muon Time Accidental (ELVETO)

  Events with accidental activities coincident with the second pulse time in the stopping counter should be removed. The accidental hits are searched for in the Range Stack, Barrel Veto, Barrel Veto Liner, and End Cap. Reject events if the energy sum of the coincident hits in any subsystem is above a threshold. The time window and energy threshold for each category are shown in Table 8.3.

Category	t Window (ns)	E Threshold (MeV)
Both-end hit category		
Range Stack (RS)	± 3.00	0.20
RS (TD)	± 0.25	5.20
Barrel Veto (BV)	± 1.25	0.20
Barrel Veto Liner (BVL)	± 2.75	0.20
Single-end hit category		
RS single energy, both time	± 7.00	0.20
RS both energy, single time	± 4.50	9.40
RS single energy, single time	± 8.75	6.60
RS no energy, both time	± 5.00	-
RS (TD) single energy, single time	± 3.00	3.20
BV single energy, both time	± 3.00	1.60
BV both energy, single time	± 0.25	0.40
BV single energy, single time	± 3.00	1.80
BV no energy, both time	± 5.75	-
BVL both energy, single time	± 0.75	0.10
BVL single energy, single time	± 5.00	1.00
BVL no energy, both time	± 5.50	-
Other category		
End Cap (EC)	± 0.25	22.00

Table 8.3: Time window and energy threshold for each category of the muon time accidental cut.

- Cut on Muon Time Accidental in the Track Counters (TDFOOL)

  Events with accidental activities overlaping the track counters and creating the second pulse in the stopping counter should be removed. TD pulses in the two layers prior to the stopping counter are fitted with a double-pulse assumption. Reject events if the fitted pulses are consistent with double pulses and the fitted time of the second pulse is coincident with the second-pulse time in the stopping counter.

- Neural Net $\pi^+ \to \mu^+$ Decay Cut (TDVARNN)

  Tail fluctuation background as well as muon time background should be removed. A Neural Net function with five variables is constructed from the single-pulse fit χ^2's, the ratios of a single-pulse fit χ^2 to that of a double-pulse fit, the energy and time of the fitted second pulse, and the difference of the second pulse times between both ends. The cut position on the NN function is set to 0.76.

A.7 Photon Veto Cuts

Any activity whose timing is coincident with the track time is searched for in all the subsystems, in order to remove events with photons. The time window and energy threshold for each category are shown in Table 8.4. Hits in the BV, BVL, and RS are further categorized into subcategories, depending on whether the counter has hits in both ends or only in single end. Time windows for the "single-end hit categories" are widened.

Category	t window (ns)	E threshold (MeV)
Both-end hit category		
Barrel Veto (BV)	±4.5	0.20
Barrel Veto Liner (BVL)	±2.0	0.00
Range Stack (RS)	±1.50	3.80
Single-end hit category		
BV single energy, single time	±9.50	4.80
BV single energy, both time	±1.00	2.80
BV both energy, single time	±11.00	8.80
BVL both energy, single time	±2.50	17.60
RS no energy, both time	±2.00	-
Other category		
End Cap (EC)	±2.25	3.80
EC inner ring (EC1)	±1.75	1.00
EC second pulse (EC2)		
Target (TG)	±1.30	4.79
I-Counter (IC)	±2.25	0.40
V-Counter (VC)	±2.00	1.60
Collar (CO)	±1.25	0.80
Microcollar (MC)	±1.50	2.80
BV early loose veto (BV1)	30.	30.
Active Degrader (AD)	±5.0	0.60

Table 8.4: Time window and energy threshold for each category of the Photon Veto Cuts.

B Choosing the Photon Veto cuts for $\pi\nu\overline{\nu}(2)$

The Photon Veto rejection in the $\pi\nu\overline{\nu}(2)$ region was extensively studied. The goal was to maximize the background rejection, while retaining a reasonable signal acceptance. To search for the best set of parameters for the 16 main PV subsystems, the same optimization process as in the $\pi\nu\overline{\nu}(1)$ analysis was used ([34]). Appropriate rejection ($K_{\pi2}$) and acceptance ($K_{\mu2}$) samples were prepared. Given an initial set of parameters (time offsets, time windows and energy thresholds for all the subsystems), the reference rejection and acceptance were measured. Then the parameters of one subsystem at a time were changed by given step sizes, and the rejection and acceptance were remeasured. A new set of parameters was chosen if it improved both the rejection and acceptance (best choice), or either of them without decreasing the other. The process was iterated, until no further improvement could be found. A schematic of the optimization process is shown in Fig. 8.1. Due to the large size of the parameter space (3×16 free parameters), care was taken to avoid falling in a local minimum. Repeating this process for 9 different "goal acceptances", the optimal set of parameters was found for each of these acceptances, that produced the best rejection-acceptance profile.

Two new PV cut categories were added in the $\pi\nu\overline{\nu}(2)$ analysis, which were not optimized with the previously mentioned procedure:

- Additional early BV (BV1): It was observed that for a wide time range (around 30 ns) before the prompt peak in the BV at RS time, there were very high energy hits in the $K_{\pi2}$sample, but not in the $K_{\mu2}$one. These were most likely due to early accidentals, that blinded the BV TDCs,

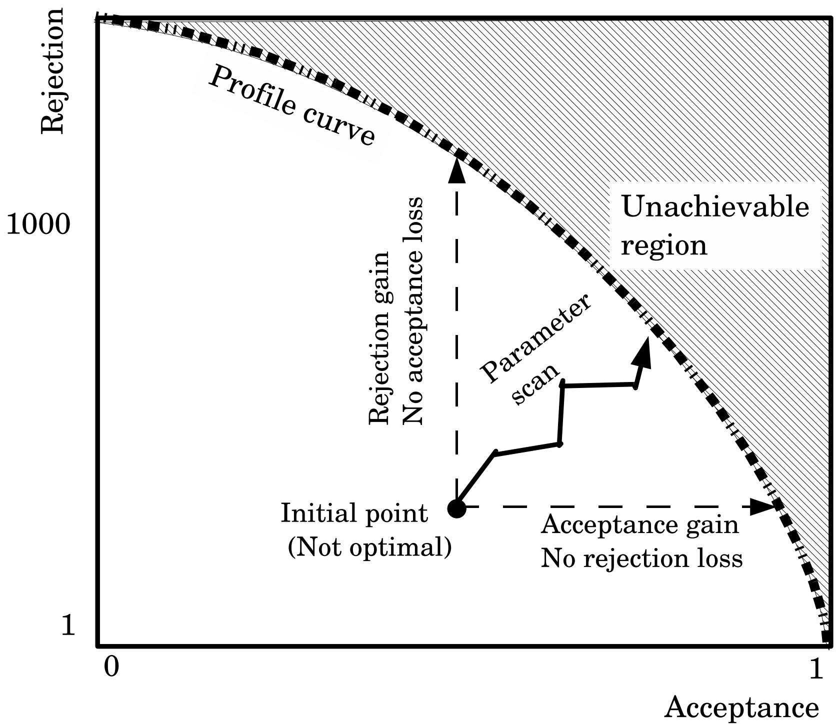

Figure 8.1: Schematic of the PV optimization process.

so that they could not register the photon hits in time with the decay. Since the ADC gates are pretty wide ($\sim$50 ns), the energy of both the accidental and the photon hit was measured, therefore these blinded BV modules had unusually high energy. Such events were vetoed with an additional BV cut at 30 MeV.

- Active Degrader (AD): To use the AD as a Photon Veto detector, care had to be taken not to veto on beam activity at Kaon time. The study and optimization of this detector is described in C.

Due to the lack of statistics in the 12 rejection classes of $K_{\pi 2}$TG-scattered events, the optimization was done in the $K_{\pi 2}$peak. The result in the $K_{\pi 2}$peak, broken down to each subsystem contribution, is shown in Fig. 8.2. Then the same PV was applied to the 12 TG-scatter classes, and the profiles of Fig. 8.3 were obtained. The values at 60% acceptance were chosen, a tighter choice than the cut used in $\pi\nu\overline{\nu}(1)$, based on the expected background for every set of parameters.

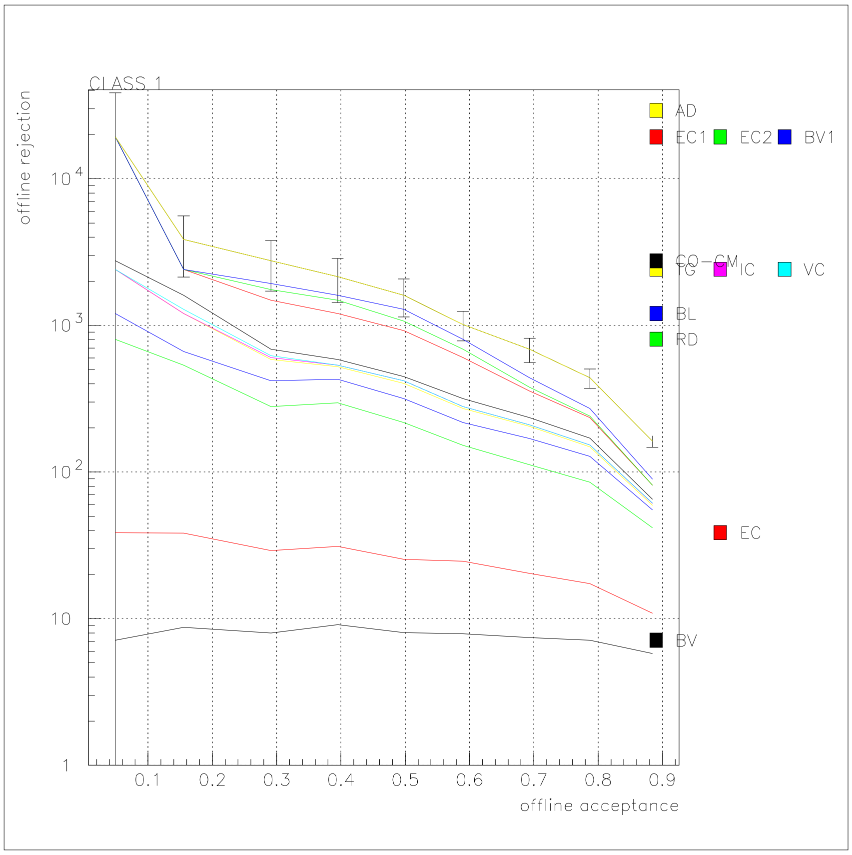

Figure 8.2: Offline rejection vs acceptance profile for the $K_{\pi 2}$peak, with each subsystem contribution.

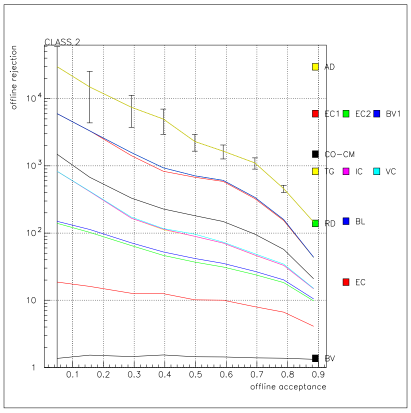

(a) CLASS2

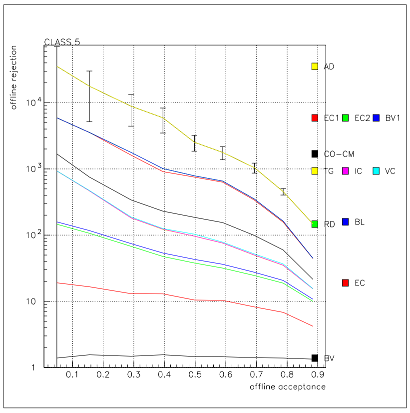

(b) CLASS5

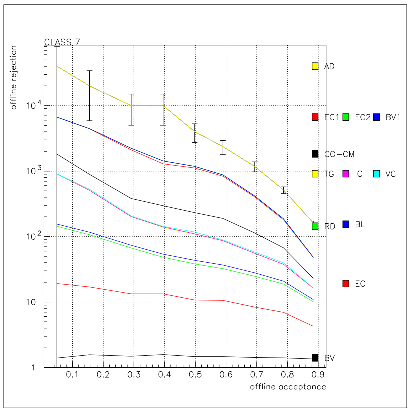

(c) CLASS7

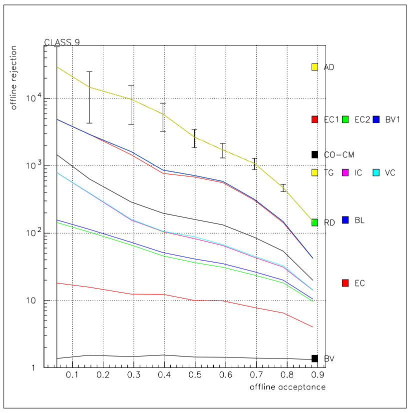

(d) CLASS9

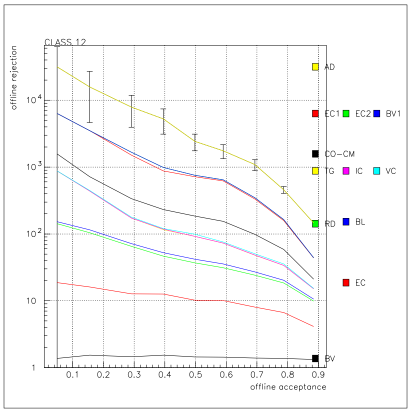

(e) CLASS12

Figure 8.3: Offline rejection vs acceptance profile for the classes with significant statistics, with each subsystem contribution.

C The Active Degrader

The Active Degrader (AD) has not been used in the PNN1 analysis, but is essential for PNN2, given the expected photon angular distribution from target-scattered $K_{\pi2}$events ([32]). Its performance was extensively studied, and its function as Photon Veto was optimized as described in this section.

In the following, "energies" are in arbitrary units. In order to find the energy in MeV, the Kaon and pion energy peaks from simulation ([35]) were used and compared with the ones from data. For the ADCs, the value of 6.49 hits/MeV was obtained from pions, and 6.22 hits/MeV from Kaons ([36]). For the CCDs, the value of 8.30 hits/MeV was found from Kaons. Therefore a calibration constant of 6.34 ADC hits/MeV (the average of the Kaon and pion results) can be used to translate the ADC energy plots to MeV, and 8.30 CCD hits/MeV for the CCD.

Beam particle track extrapolation was done to find which AD sectors are expected to be transversed by the incoming K, and thus have some energy deposit associated with the beam. The possibility of excluding these sectors for PV purposes was investigated. The incoming xy point was found by extrapolating the line defined by the hit points in BWC1 and BWC2 to the upstream face of the AD. The outgoing point was the one given by the B4 hit coordinates. Every sector between these 2 points was assigned to the K path. This algorithm has the flaw that it does not take into account the transverse uncertainty to the entering K point caused by multiple scattering in the Inactive Degrader, which is exacerbated by the geometry of the AD: since the beam is centered where all the sectors meet, a small perturbation in the path causes more/other sectors than expected to be hit.

The samples used in this study are:

- Acceptance sample: Clean $K_{\mu 2}$from $K_{\mu 2}$monitors, where no photon or beam activity is expected.

- Rejection sample 1: $K_{\pi 2}$peak events from SKIM5, with a loose PV cut.

- Rejection sample 2: $K_{\pi 2}$TG-scatter events identified by special target reconstruction software ([37]). These events ("kinks") have failed the normal target reconstruction ("SWATHCCD"), therefore they were not included in any background study and there is no danger in examining the ones in the PNN2 kinematic box. This sample is expected to be the richest one in TG scatters.

C.1 Timing peaks in the AD

In fig.8.4-8.7, the time distributions of hits in the AD are shown for the acceptance and the rejection samples. All the histograms are normalized to the number of events/incoming Kaons and have no energy threshold imposed. As can be seen in fig. 8.4, which is for sectors on the K path, the behavior of the three samples is effectively the same in terms of K activity: in the time distributions with respect to Kaon time (tk), an on-time peak is obvious, and the ones with respect to decay (pion) time (tpi), show a decay lifetime shape. Fig. 8.5 shows the same distributions for sectors off the K path. In the time distributions with respect to tpi, a strong photon peak is present for the rejection samples only. A decay lifetime shape for the same samples is present in the

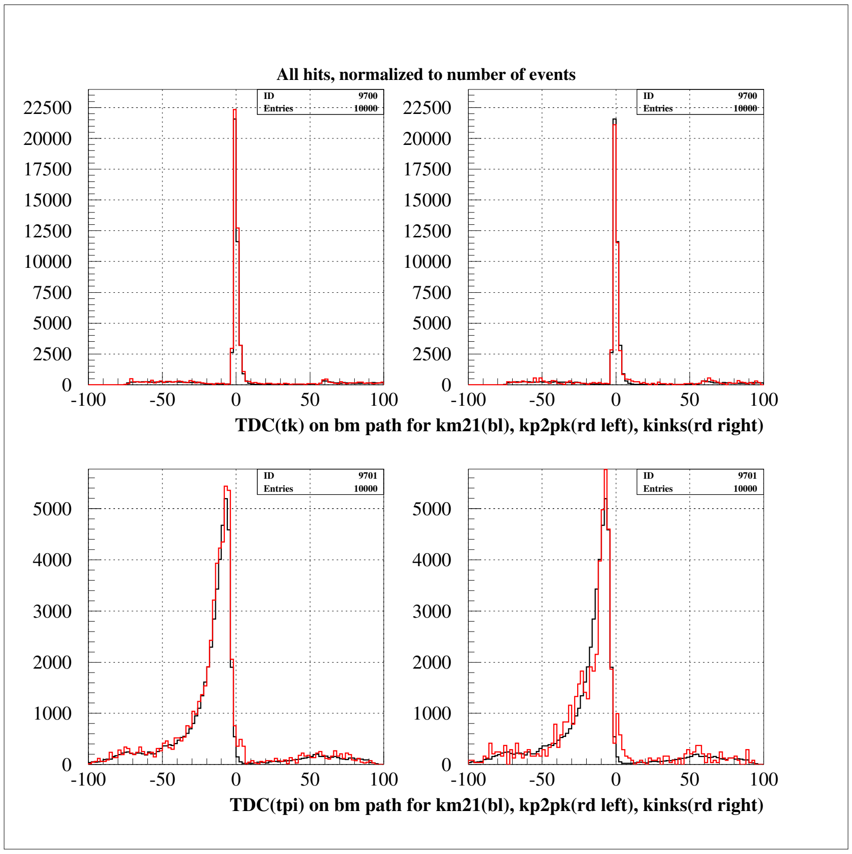

Figure 8.4: Time distributions of the AD TDC hits with respect to tk (top row) and tpi (bottom row) for sectors on the incoming Kaon path. Black histograms are for the acceptance sample and red for the two rejection samples ($K_{\pi 2}$peak on the left and kinks on the right). The units on the vertical axis are arbitrary.

time distributions with respect to tk. Fig. 8.6 and fig. 8.7 show the same for the CCDs. In addition to the photon peak in fig. 8.5 and 8.7, some K activity remnants in time with tk are present, that are the same for all samples. These are due to the inefficiencies in extrapolating the K path mentioned earlier.

The photon time distributions for $K_{\pi 2}$peak events and kinks are compared in fig. 8.8, where it can be seen that there is more photon activity in the AD for kinks. Comparing the number of events in the 3 bins of the photon peak

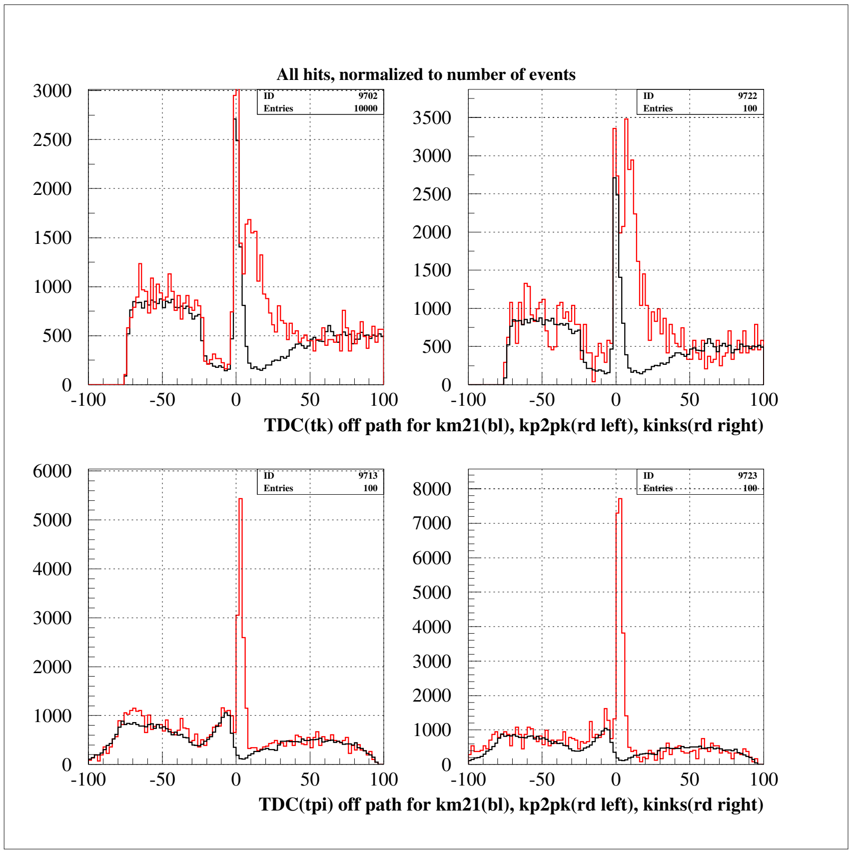

Figure 8.5: Time distributions of the AD TDC hits with respect to tk (top row) and tpi (bottom row) for sectors off the incoming Kaon path. Black histograms are for the acceptance sample and red for the two rejection samples ($K_{\pi2}$peak on the left and kinks on the right). The units on the vertical axis are arbitrary.

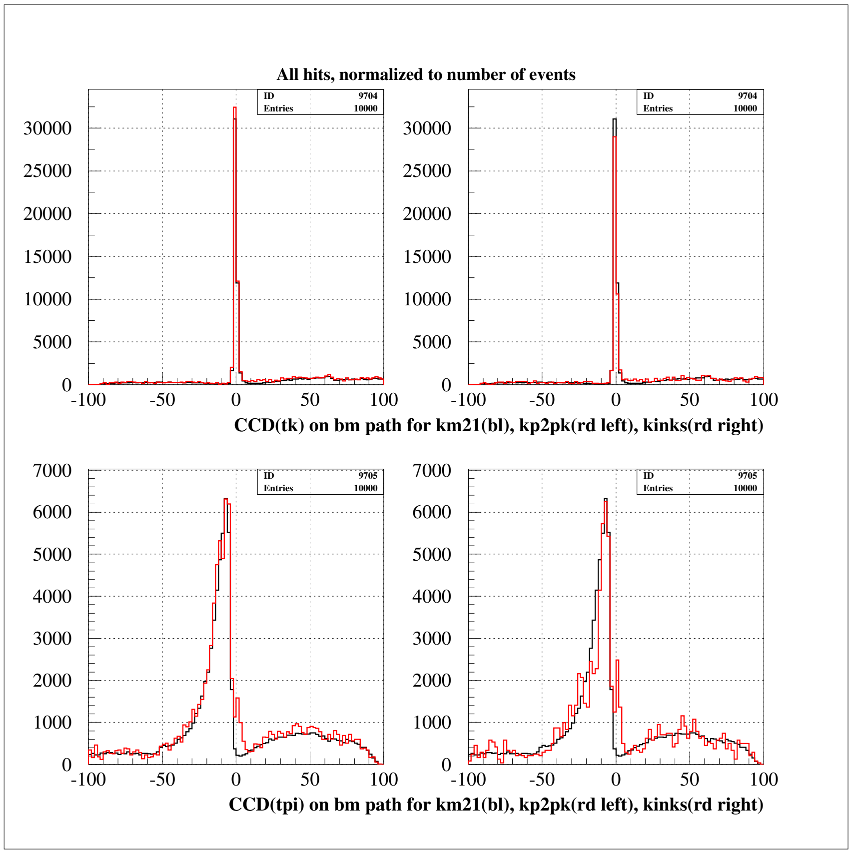

Figure 8.6: Time distributions of the AD CCD hits with respect to tk (top row) and tpi (bottom row) for sectors on the incoming Kaon path. Black histograms are for the acceptance sample and red for the two rejection samples ($K_{\pi 2}$peak on the left and kinks on the right). The units on the vertical axis are arbitrary.

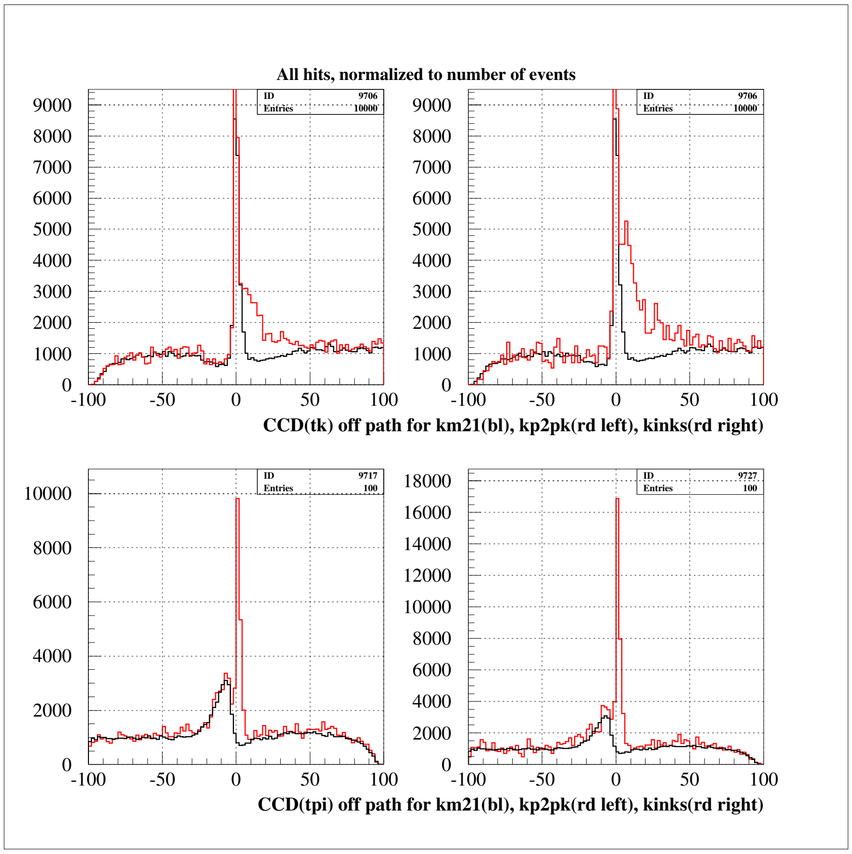

Figure 8.7: Time distributions of the AD CCD hits with respect to tk (top row) and tpi (bottom row) for sectors off the incoming Kaon path. Black histograms are for the acceptance sample and red for the two rejection samples ($K_{\pi 2}$peak on the left and kinks on the right). The units on the vertical axis are arbitrary.

for $K_{\pi 2}$peak and kinks, there is an approximate 72% more activity in the kink sample measured by the TDCs and 60% by the CCDs.

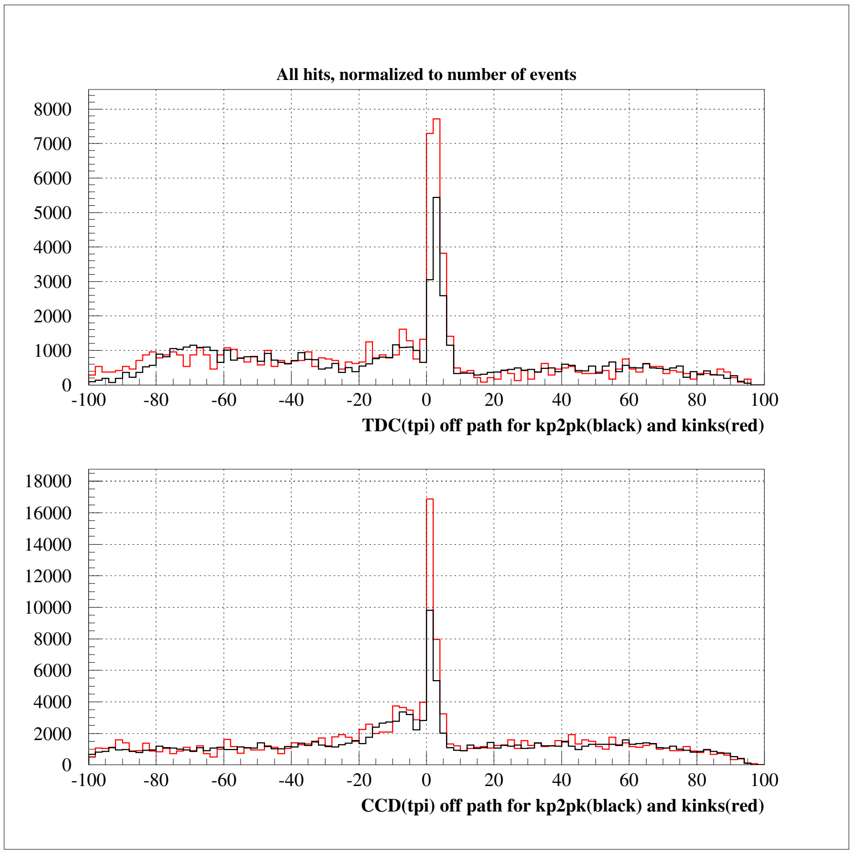

Figure 8.8: Time distributions with respect to tpi for sectors off the incoming Kaon path, from TDCs (top) and CCDs (bottom). Black histograms are for $K_{\pi 2}$peak and red for kinks. The units on the vertical axis are arbitrary.

Time closest to tk/tpi vs total energy distributions for the same samples are shown in fig. 8.9 (fig. 8.10 for CCDs) and energy distributions for the two timing peaks in fig. 8.11 (fig. 8.12 for CCDs). The K energy peak in time with tk is prominent for all samples, whereas most of the energy in time with tpi is at zero for the acceptance sample, and near zero with long high-energy tails for the rejection ones, as expected for showering photons.

C.2 Applying the cut

Based on the time and energy distributions in the AD, different ways to apply a PV cut were investigated. The main idea is to add the energy deposited either in whole sectors (for ADCs) or individual hits (for CCDs) and veto events based on this sum. For the ADCs, the different schemes are using sectors

- (a) with at least one TDC hit out of time with tk (>5ns) and in time with tpi (-2ns to 8ns)
- (b) same with (a) and no TDC hit at tk (±5ns)
- (c) same with (a) and the sector is also out of the K path
- (d) same with (b) and the sector is also out of the K path.

For the CCDs, hits are used that are either

- (a) in time with tpi and out of time with tk
- (b) same with (a) and in sectors out of the K path

The results, in the form of acceptance*rejection vs energy threshold, are shown in fig. 8.13 for the $K_{\pi 2}$peak and in fig. 8.14 for the kinks. For both the rejection samples, cutting on the sum of CCD "energy" at 5., irrespective of the sector the hit belongs to, seems to be the favorable case. Therefore no sector exclusion, or double-pulse fitting is necessary to mask out beam Kaon activity. The time window for this scheme was also optimized. The rejection, acceptance and rejection*acceptance for the lowest energy threshold for all cases are summarized in table 8.5.

	ADC (a),(b)	ADC (c),(d)	CCD (a)	CCD (b)
acc	0.96±0.001	0.98±0.001	0.94±0.002	0.97±0.001
$K_{\pi 2}$peak				
rej	1.64±0.03	1.54±0.03	1.79±0.04	1.59±0.03
acc*rej	1.58±0.03	1.51±0.02	1.68±0.04	1.54±0.03
Kinks				
rej	1.81±0.07	1.73±0.05	1.95±0.08	1.80±0.07
acc*rej	1.76±0.08	1.70±0.06	1.86±0.08	1.76±0.08

Table 8.5: Rejection, acceptance and rej*acc of different implementations of the AD photon veto for both rejection samples, for the lowest thereshold (5.).

C.3 Correlation with the EC

The rej*acc of the AD as a function of the energy threshold was also measured for tighter setup PV cuts and for only the upstream EC inner ring (EC1) PV tightened, in order to investigate the correlation of this subsystem with the rest of the PV. Photon activity in the AD is expected to be heavily correlated with activity in the EC1, as shown in [38]. The plots for the $K_{\pi 2}$peak for tight PV are shown in fig. 8.15, and for only the EC1 PV tightened in fig. 8.16. The results for the optimal case (CCD (a), at the lowest threshold) are summarized in table 8.6. The rej*acc is a bit higher for the tight PV sample, which means that the AD still has rejection power after the rest of the PV has been applied, and a bit smaller for the only-EC1-tightened one, as expected for these two correlated subsystems. In both cases, it follows the same trend as a function of energy threshold as the loose-PV case.

Further evidence of the AD-EC correlation is shown in fig. 8.17-8.18. The fraction of events with zero energy deposit in EC1 and the remaining upstream EC is shown as a function of the AD energy deposit for the three samples.

	loose PV (95%)	tight PV (53%)	tight EC1
acc	0.94±0.002	0.95±0.002	0.95±0.002
rej	1.79±0.04	1.95±0.14	1.69±0.07
acc*rej	1.68±0.04	1.86±0.13	1.60±0.06
EC1 parameters			
t half-window	2 ns	5.15 ns	5.15 ns
E threshold	2 MeV	0.2 MeV	0.2 MeV

Table 8.6: Rejection, acceptance and rej*acc of CCD(a) for the lowest energy thereshold for different setup PV cut, for $K_{\pi2}$peak. The EC1 veto parameters for every setting are also given.

The rest of the PV has not been applied on the rejection samples, to increase statistics. From the $K_{\mu2}$sample, it can be seen that the accidentals rate is at about 10% for both pieces of the upstream EC. The rejection samples show a clear correlation between both upstream EC parts and the AD. The rise of these plots in both the rejection samples for very high AD energies, is due to the online PV that has already cut events with high energy deposits in the EC. These events most likely also leave the highest energy in the AD.

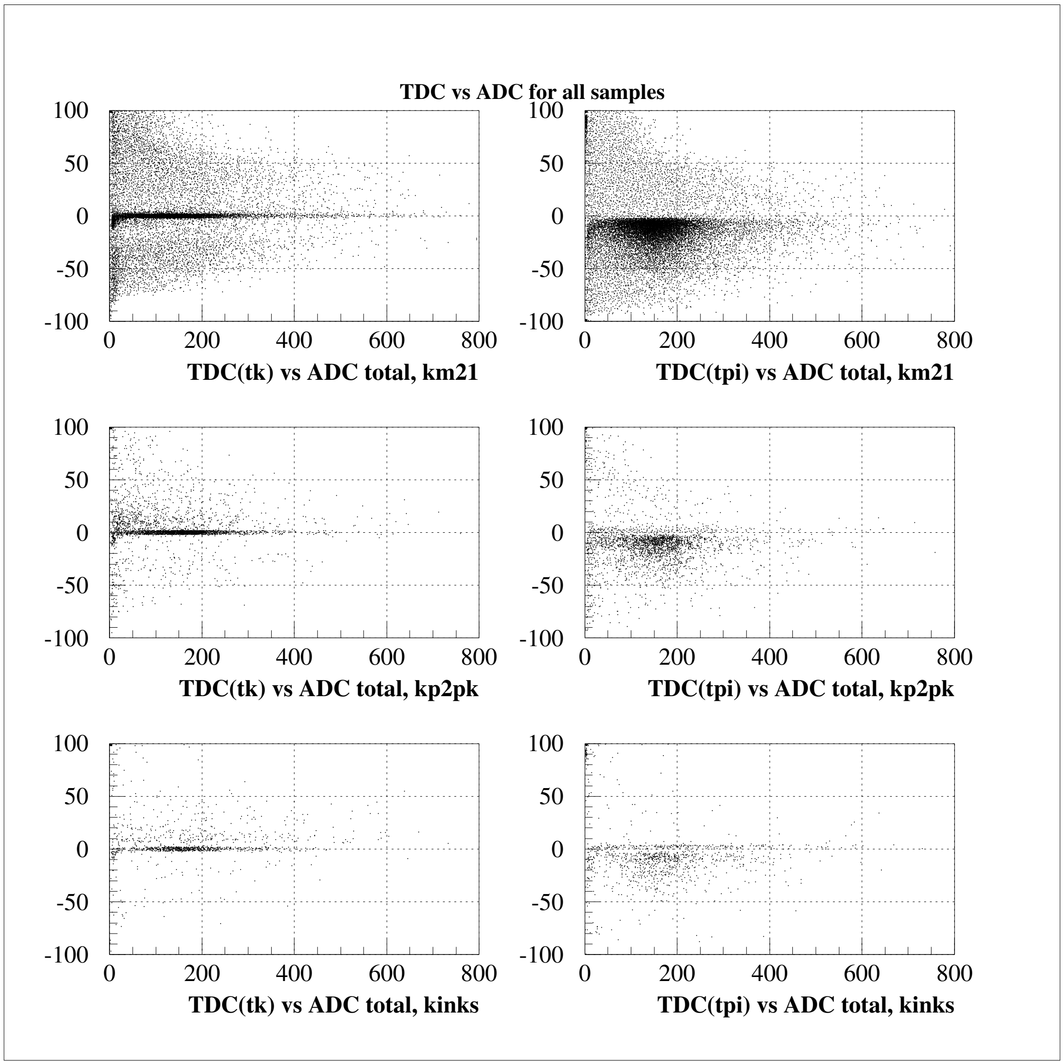

Figure 8.9: Time distributions with respect to tk (left) and tpi (right) of the TDC hit closest to tk or tpi, vs total ADC energy for $K_{\mu 2}$(top), $K_{\pi 2}$peak (middle) and kinks (bottom).

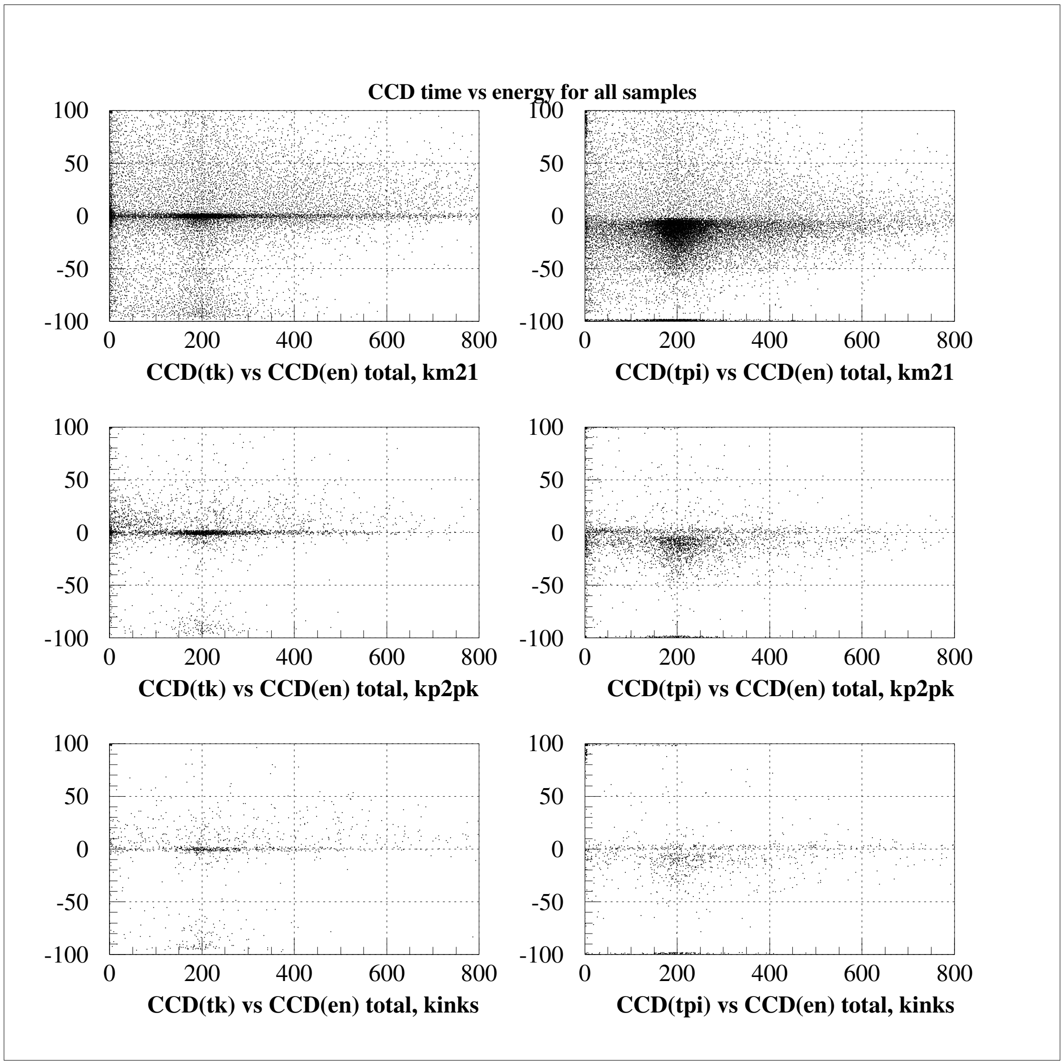

Figure 8.10: Time distributions with respect to tk (left) and tpi (right) of the CCD hit closest to tk or tpi, vs total CCD energy for $K_{\mu 2}$(top), $K_{\pi 2}$peak (middle) and kinks (bottom).

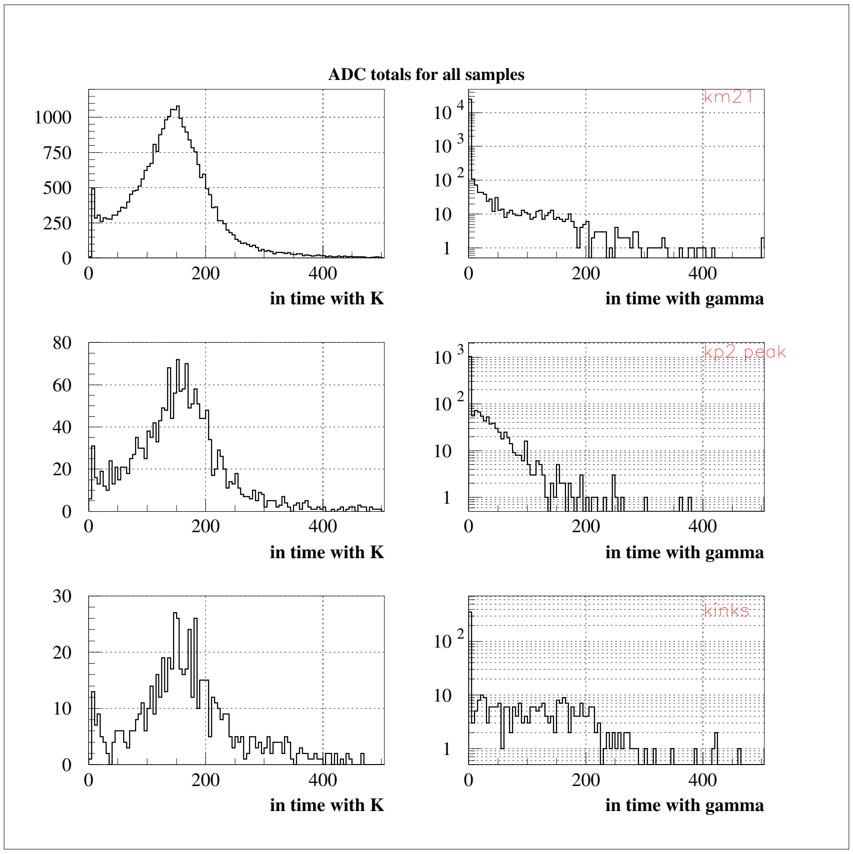

Figure 8.11: Total ADC energy in time with tk ($\pm 5ns$, left), and in time with the photon ($0 - 8ns$ from tpi, right) for $K_{\mu 2}$(top), $K_{\pi 2}$peak (middle) and kinks (bottom).

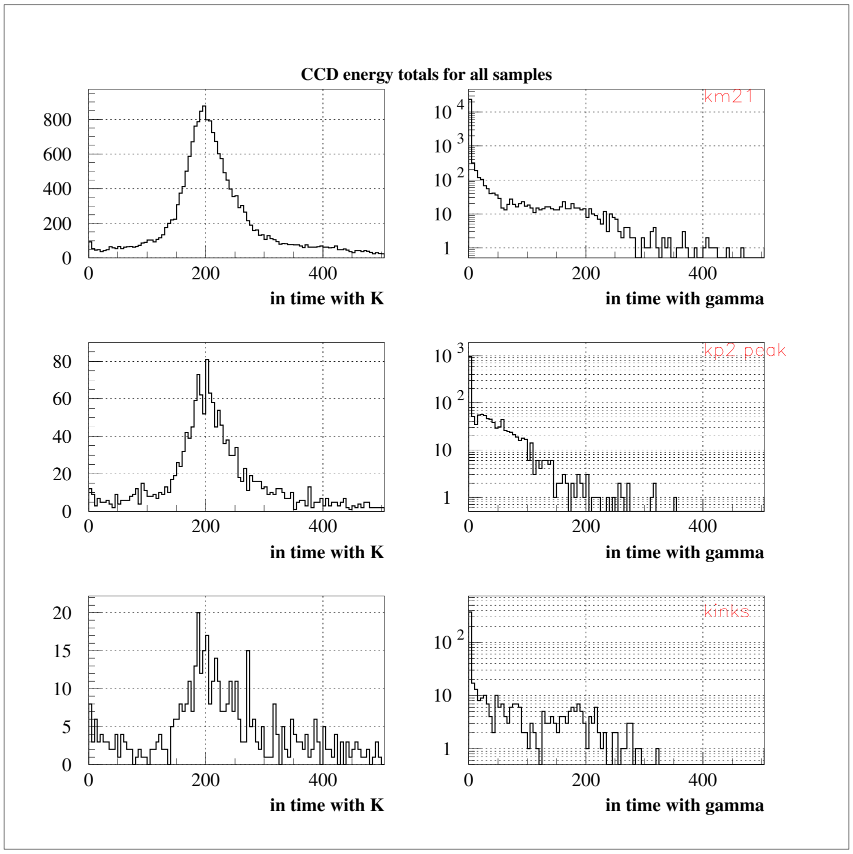

Figure 8.12: Total CCD energy in time with tk ($\pm 5ns$, left), and in time with the photon ($0-8ns$ from tpi, right) for $K_{\mu 2}$(top), $K_{\pi 2}$peak (middle) and kinks (bottom).

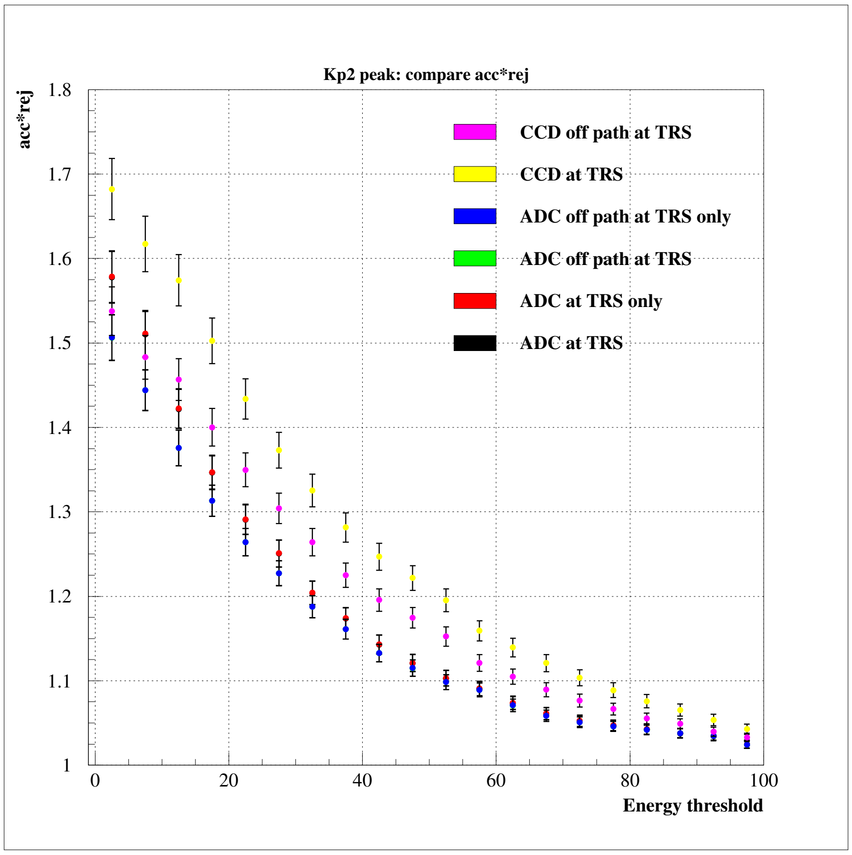

Figure 8.13: Acceptance*rejection vs total ADC or CCD energy threshold, for different sector selection, for $K_{\pi 2}$peak events. The different sets of points correspond to ADC cases a-d and CCD cases a-b explained in the text, from bottom to top. The points for ADC cases a and b (black and red), as well as c and d (green and blue), completely overlap.

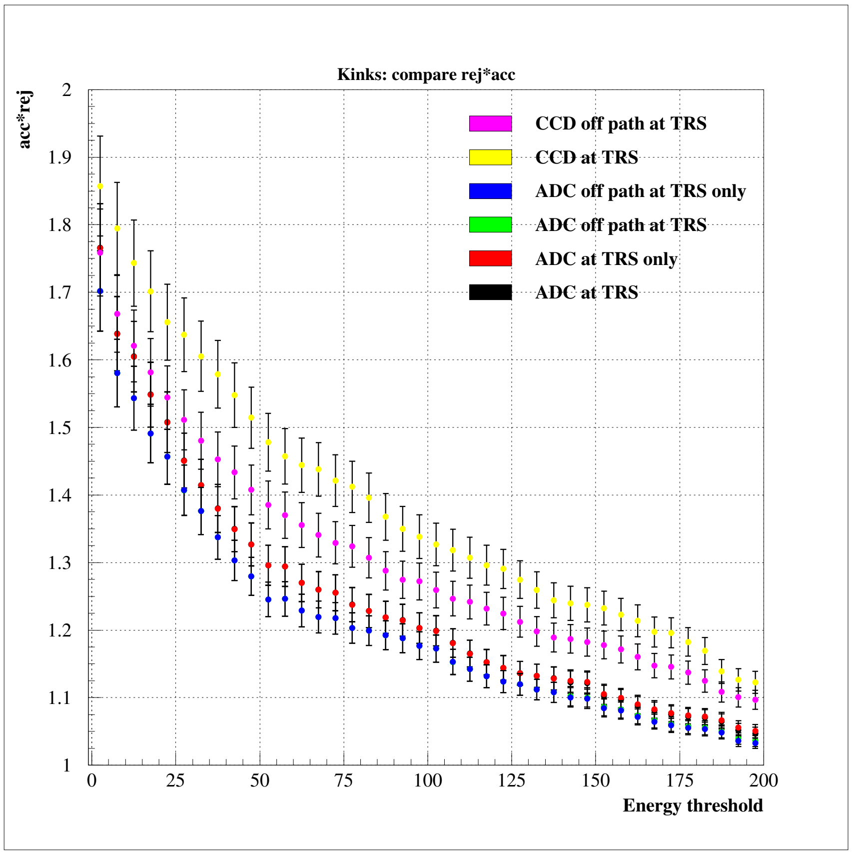

Figure 8.14: Acceptance*rejection vs total ADC or CCD energy threshold, for different sector selection, for kink events. The different sets of points correspond to ADC cases a-d and CCD cases a-b explained in the text, from bottom to top. The points for ADC cases a and b (black and red), as well as c and d (green and blue), completely overlap.

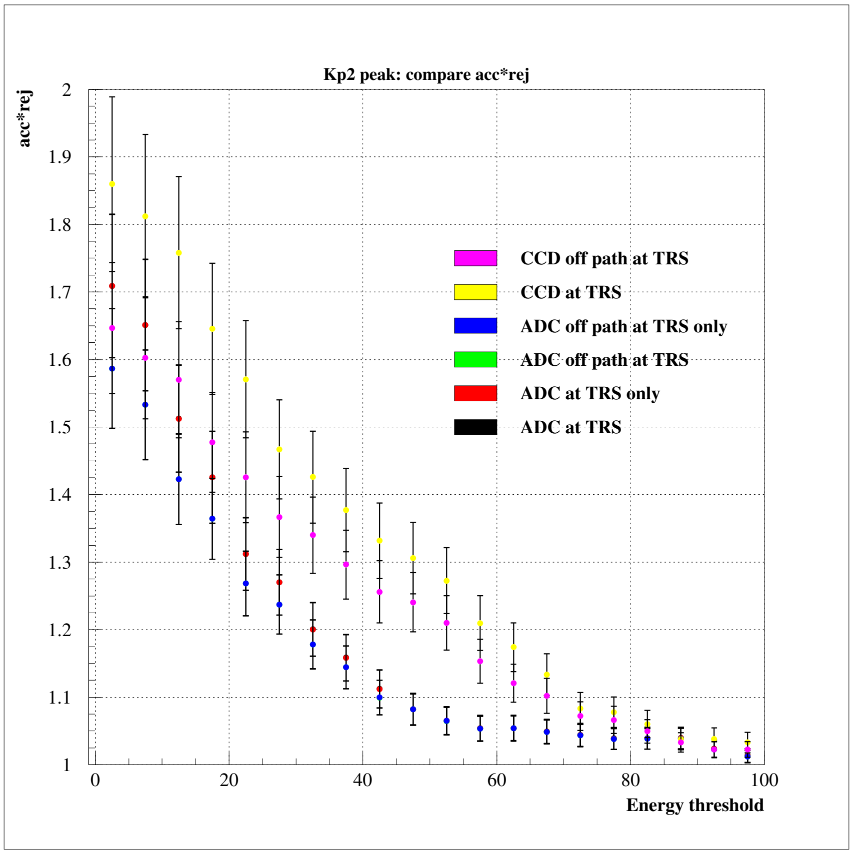

Figure 8.15: Acceptance*rejection vs total ADC or CCD energy threshold, for different sector selection, for $K_{\pi 2}$peak events with tight setup PV. The different sets of points correspond to ADC cases a-d and CCD cases a-b explained in the text, from bottom to top. The points for ADC cases a and b (black and red), as well as c and d (green and blue), completely overlap.

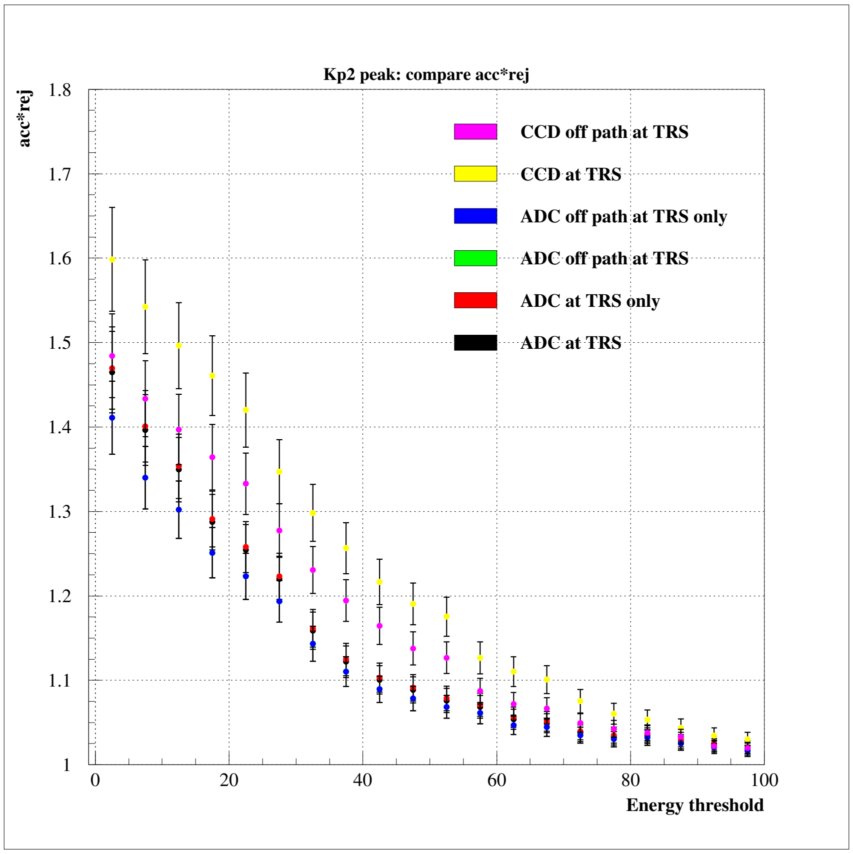

Figure 8.16: Acceptance*rejection vs total ADC or CCD energy threshold, for different sector selection, for $K_{\pi 2}$peak events with tight setup EC1 PV, with the rest of the systems at a loose setting. The different sets of points correspond to ADC cases a-d and CCD cases a-b explained in the text, from bottom to top. The points for ADC cases a and b (black and red), as well as c and d (green and blue), completely overlap.

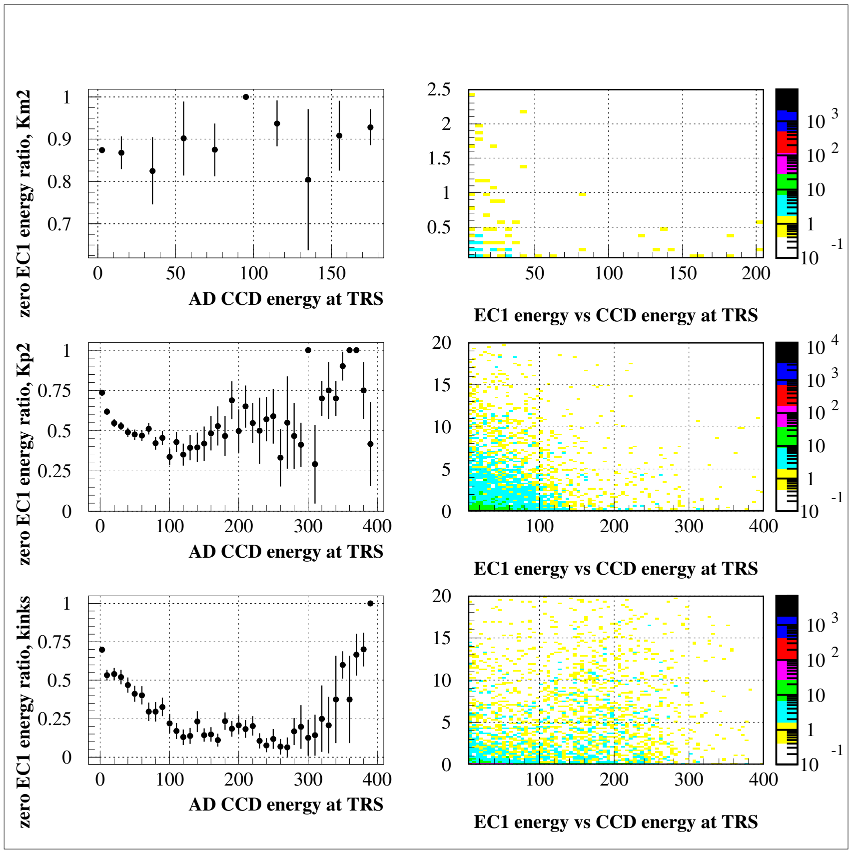

Figure 8.17: Percentage of events with zero energy deposit in the EC1 as a function of energy deposit in the AD (left) and the scatter plots of EC1 energy vs AD CCD energy that these graphs were created from (right), for $K_{\mu 2}$(top), $K_{\pi 2}$peak (middle) and kinks (bottom).

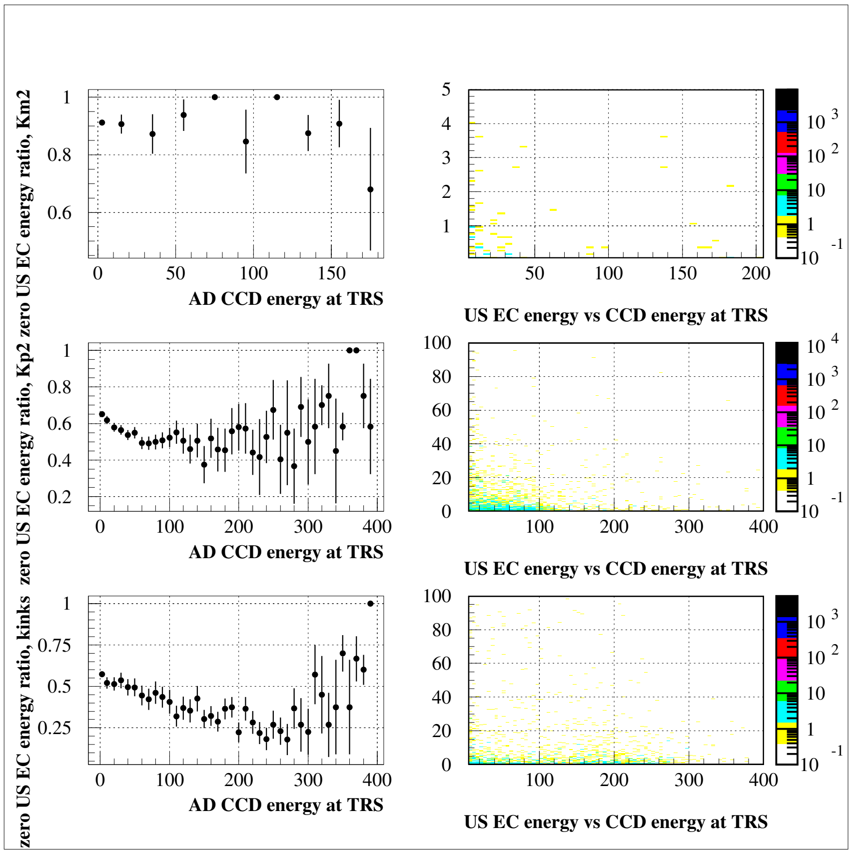

Figure 8.18: Percentage of events with zero energy deposit in the upstream EC (without the inner ring) as a function of energy deposit in the AD (left) and the scatter plots of EC1 energy vs AD CCD energy that these graphs were created from (right), for $K_{\mu 2}$(top), $K_{\pi 2}$peak (middle) and kinks (bottom).

Bibliography

[1] J.H. Christenson, J.W. Cronin, V.L. Fitch and R. Turlay, Phys. Rev. Lett. **13**, 138 (1964).

[2] M. Kobayashi and T. Maskawa, Prog. Theor. Phys. **49**, 652 (1973).

[3] S.L. Glashow, J. Iliopoulos, and L. Maiani, Phys. Rev. **D2**, 1285 (1970).

[4] N. Cabibbo, Phys. Rev. Lett. **10**, 531 (1963).

[5] L. Wolfenstein, Phys. Rev. Lett. **51**, 1945 (1983).

[6] Particle Data Group, W.-M. Yao *et al.*, Journal of Physics G **33**, 1 (2006)

[7] CKMfitter Group (J. Charles *et al.*), Eur. Phys. J. C41, 1-131 (2005) and http://ckmfitter.in2p3.fr

[8] A.J. Buras, F. Schwab, and S. Uhlig, arXiv:hep-ph/0405132 (2004).

[9] A.J. Buras, M. Gorbahn, U. Haisch and U. Nierste, arXiv:hep-ph/0603079 (2006).

[10] W.J. Marciano and Z. Parsa, Phys. Rev. **D53**, 1 (1996).

[11] Particle Data Group, S. Eidelman *et al*, Phys. Lett. **B592** (2004) 1, and 2005 partial update for edition 2006 available at http://pdg.lbl.gov.

[12] A.J. Buras, M.E. Lautenbacher, and G. Ostermaier, Phys. Rev. **D50**, 3433 (1994).

[13] D. Rein and L.M. Sehgal, Phys. Rev. **D39**, 3325 (1989); J.S. Hagelin and L.S. Littenberg, Prog. Part. Nucl. Phys. **23**, 1 (1989); M. Lu and M.B. Wise, Phys. Lett. **B324**, 461 (1994); S. Fajfer, arXiv:hep-ph/9602322 (1996); C.Q. Geng, I.J. Hsu, and Y.C. Lin, Phys. Rev. **D54**, 877 (1996).

[14] A. Belyaev *et al.*, Kaon Physics working Group Report "Kaon Physics with a High-intensity Proton Driver", arXiv:hep-ph/0107046 (2001); G. Isidori, arXiv:hep-ph/0110255 (2001); G. Buchalla, arXiv:hep-ph/0110313 (2001).

[15] A.J. Buras, arXiv:hep-ph/0402191 (2004); G. Isidori, arXiv:hep-ph/0301159 (2003).

[16] A.J. Buras *et al.*, arXiv:hep-ph/0402112 (2004); A.J. Buras *et al.*, arXiv:hep-ph/0408142 (2004).

[17] Y. Grossman and Y. Nir, Phys. Lett. **B398**, 163 (1997).

[18] B. Bassalleck *et al.*, E949 proposal, BNL-67247, TRI-PP-00-06 (1999), `http://www.phy.bnl.gov/e949/` .

[19] T. Yoshioka *et al.*, IEEE Trans. Nucl. Sci. **51**, 199 (2004).

[20] J. Doornbos *et al.*, Nucl. Instr. Meth. **A444**, 546 (2000).

[21] D.A. Bryman *et al.*, Nucl. Instr. Meth. **A396**, 394 (1997).

[22] M. Atiya *et al.*, Nucl. Instr. Meth. **A279**, 180 (1989).

[23] E.W. Blackmore *et al.*, Nucl. Instr. Meth. **A404**, 295 (1998).

[24] R.A. McPherson, "Chasing the Rare Decay $K^+ \to \pi^+\nu\overline{\nu}$", Princeton University, Ph.D. Thesis, November, 1995.

[25] I.H. Chiang *et al.*, IEEE Trans. Nucl. Sci. **42**, 394 (1995).

[26] T.K. Komatsubara *et al.*, Nucl. Instr. Meth. **A404**, 315 (1998).

[27] C. Caso *et al.*, European Physical Journal **C3**, 1 (1998).

[28] P. Meyers, "A modified Version of the UMC Multiple Scattering Routine MSCAT1", E787 Technical Note No.77 (1985). Unpublished.

[29] A.J. Stevens, "Nuclear Interactions in CH revisited", E787 Technical Note No.140 (1987). Unpublished.

[30] W.R. Nelson *et al.*, "The EGS4 Code Syatem", SLAC 265, SLAC (1985).

[31] B. Bhuyan, 'Search for the Rare Kaon Decay $K^+ \to \pi^+\nu\overline{\nu}$', PhD thesis, 2003.

[32] V. Jain, 'Simulation of elastic scatters of π^+ in the target from Kp2 decays', E787 technical note 375, 1999.

[33] C. Witzig, "π^- absorption in the RS", E787 technical note 278, 1994.

[34] K. Mizouchi, 'Experimental Search for the Decay $\pi^o \to \nu\overline{\nu}$', PhD thesis, 2006.

[35] Coombes *et al*, "Tests of prototype E949 beam instrumentation", E949 technical note K-020, 2001.

[36] D.E. Jaffe, "Estimate of number of photoelectrons in the AD", E949 technical note K-057, 2006.

[37] B. Lewis, "A new Target Reconstruction and Target Scatter Algorithm", E949 technical note K-063, 2006.

[38] T. Numao, "Monte Carlo study of the Active Degrader", E949 technical note K-008, 1999